

Hedda Christine Soland

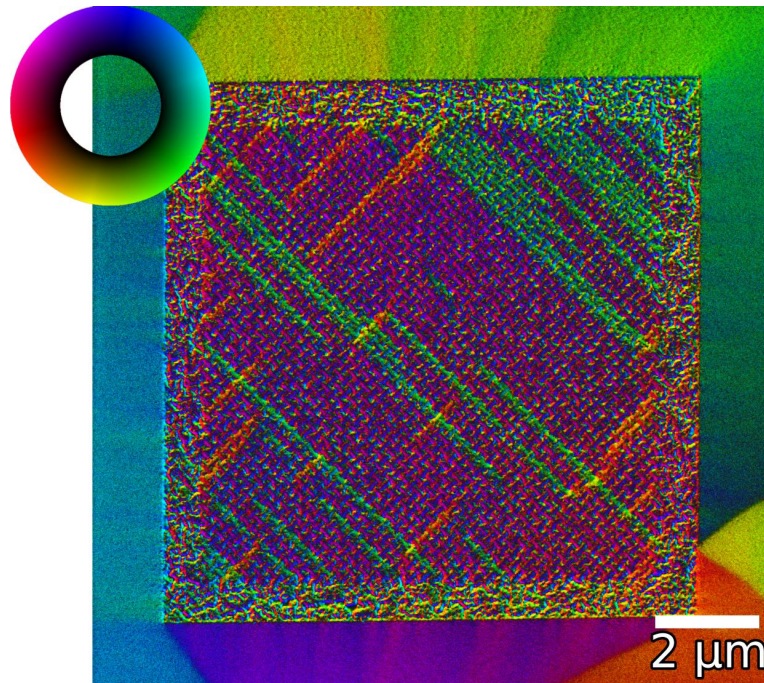
# Using STEM-DPC with a Conventional ADF Detector to Explore FIB Patterned Artificial Spin Ice Structures in Permalloy

Master's thesis in MTNANO

Supervisor: Magnus Nord

Co-supervisor: Erik Folven, Gregory Nordahl

June 2023







Hedda Christine Soland

# **Using STEM-DPC with a Conventional ADF Detector to Explore FIB Patterned Artificial Spin Ice Structures in Permalloy**

Master's thesis in MTNANO

Supervisor: Magnus Nord

Co-supervisor: Erik Folven, Gregory Nordahl

June 2023

Norwegian University of Science and Technology



Norwegian University of  
Science and Technology



---

# Abstract

We find ourselves in the midst of a remarkable technological revolution, with rapid advancements in fields such as artificial intelligence, robotics and information technology. Consequently, there is a pressing need for low-power technologies that are not reliant on continuous power supply. The field of spintronics aims to resolve this by coupling electric and magnetic properties. To pave the way for this new technology, it is imperative to deepen our understanding of how magnetism acts at the nanoscale by exploring the behaviour of magnetic nanostructures. Fortunately, with the advancements made in nanofabrication and characterization equipment over the past decades, our ability to study magnetism all the way down to the nanoscale is ever-increasing.

Among the myriad of fascinating nanosized magnetic systems, is artificial spin ice (ASI). ASIs are geometrically frustrated systems composed of coupled nanomagnets arranged in a two-dimensional lattice and have since their discovery in 2006 been extensively studied as model systems to explore magnetic frustration. In the last decade, ASIs have also shown great promise for use in novel and efficient ways to store data and for alternative computing methods like reservoir computing. To accelerate our understanding of ASI systems, efficient and accessible characterization methods are needed. Scanning transmission electron microscopy (STEM) is a well-established technique predominantly used to study nanoscale structures with Ångström resolution, map chemical composition and map crystallographic orientations within materials. However, by turning off the objective lens (OL) of the microscope, internal magnetic fields in materials can be imaged by utilizing the Lorentz force, which leads to a deflection of the electron beam that is detectable on any standard STEM detector. This technique is called STEM - differential phase contrast (DPC). By combining STEM-DPC with a weakly excited OL and tilting the sample, it is even possible to image the switching of ferromagnetic domains in materials down to the nanoscale.

In this work, we have successfully fabricated a wide range of ASI systems composed of islands as small as  $225\text{nm}\times 75\text{nm}$ <sup>1</sup>, using a focused ion beam (FIB). The structures were characterized with two distinct STEM-DPC techniques using a conventional annular dark field (ADF) detector. The fabrication and characterization techniques showed exceptionally good results, indicating that the methodology is indeed well-suited for fast prototyping and characterization of ASIs, and can even be combined with structural and chemical analysis in the TEM. Due to continuous advancements in aberration correction and STEM detectors, it is believed that this can become a valuable tool in the development of novel, low-power spintronic devices.

---

<sup>1</sup>This is comparable to the dimensions typically used in the ASI community.

# Sammendrag

Vi befinner oss midt i en bemerkelsesverdig teknologisk revolusjon, der utviklingen innenfor områder som kunstig intelligens, robotikk og informasjonsteknologi er enorm. Som følge av dette er det et stort behov for mer energieffektiv teknologi enn det som er mulig med tradisjonell silisiumbasert halvlederteknologi. Forskningsfeltet spintronikk kobler magnetiske og elektriske egenskaper. For å legge grunnlaget for denne nye teknologien er det viktig å forstå hvordan magnetisme opptrer på nanoskala ved å utforske adferden til magnetiske nanostrukturer. Heldigvis, med fremskrittene som er gjort innen nanofabrikasjons og karakteriseringsverktøy de siste tiårene, blir det mer og mer mulig å studere magnetisme helt ned på nanoskalaen.

Blant utallige fascinerende magnetiske nanosystemer, har vi *kunstig spinn is*. Dette er geometrisk frustrerte systemer bestående av komplette nanomagneter satt sammen i en todimensjonal gitterstruktur, og har siden oppdagelsen i 2006 blitt mye studert for å utforske magnetisk frustrasjon. De siste tiårene har kunstig spinn is også vist seg å være en god kandidat som materiale til energi-effektiv datalagring og reservoar-computing. For å akselerere forståelsen av avanserte ASI systemer er effektive og lett tilgjengelige karakteriseringsmetoder nødvendig. Skanning transmisjonselektronmikroskopi (STEM) er en veletablert teknikk som primært brukes til å studere nanoskala strukturer og materialesammensetning med Ångstrøm-oppløsning, kartlegge kjemisk sammensetning og kartlegge krystallografiske orienteringer i materialer. Ved å slå av objektivlinsen (OL) i mikroskopet kan man imidlertid avbilde de interne magnetfeltene i materialer ved hjelp av Lorentzkraften, som fører til en avbøyning av elektronstrålen og kan oppdages av en hvilken som helst standard STEM-detektor. Dette gir opphav til STEM - differensiell fasekontrast (DPC). Ved å kombinere STEM-DPC med en svakt eksitert OL, og samtidig tilte prøveholderen, er det mulig å avbilde flipping av ferromagnetiske domener i materialer helt ned på nanoskala.

I dette arbeidet har vi med stor suksess fabrikert ulike ASI-systemer bestående av magneter så små som  $225\text{nm} \times 75\text{nm}^2$ , ved hjelp av en fokusert ionestråle (FIB). Strukturene ble karakterisert med to forskjellige STEM-DPC-teknikker ved bruk av en konvensjonell mørkefelt-detektor (ADF). Fabrikasjons- og karakteriseringsmetodene viste svært gode resultater, noe som indikerer at metoden er godt egnet for rask prototyping og karakterisering av ASI-systemer, og kan til og med kombineres med strukturell og kjemisk analyse i TEM. Gitt at utviklingen av aberrasjonskorrigering og STEM-detektorer fortsetter, antas det at dette kan bli et verdifullt verktøy for utvikling innenfor spintronikk.

---

<sup>2</sup>Dette er sammenlignbart med dimensjoner som vanligvis brukes i ASI-miljøet.

# Preface

This project is meant to showcase the knowledge and skills acquired throughout a five years integrated Master of Science in Nanotechnology, with a specialisation in Nanomaterials for Energy and the Environment, at the Faculty of Natural Sciences at the Norwegian University of Science and Technology (NTNU). The work was found to be enlightening and a worthy end to this academic journey. All of the results presented were obtained during the spring semester of 2023 and built upon the specialisation project carried out in the subsequent semester. The project was organized by the Department of Physics at the Norwegian Micro and Nano-Fabrication Facility, NorFab, supervised by Associate Professor Magnus Nord. and co-supervisors Professor Erik Folven and PhD Candidate Gregory Nordahl. Sample fabrication was performed at NTNU Nanolab by Gregory Nordahl and the author herself, and magnetic characterization at the TEM Gemini Centre, Norwegian Centre for Transmission Electron Microscopy, NORTEM. We acknowledge the support from the Research Council of Norway for the Norwegian Center for Transmission Electron Microscopy, NORTEM (197405), NorFab (295864), and In-situ Correlated Nanoscale Imaging of Magnetic Fields in Functional Materials, InCoMa (315475). This work focused on the optimization of two STEM-DPC imaging techniques for artificial spin ice structures, utilizing a conventional ADF detector. Additionally, the fabrication process of these structures using FIB was also optimized. STEM-DPC was performed in low-magnification mode, where the objective lens is switched off, to minimize the magnetic field felt by the specimen. Sample fabrication in FIB, magnetic characterization in STEM, and subsequent data processing were all performed by the experimentalist herself, with the guidance of Magnus Nord, Gregory Nordahl, Bjørn Gunnar Solheim, Emil Christiansen and Yu Liu. The author would like to thank you all for teaching her the fabrication and characterization techniques necessary to obtain the final results. It has been incredible to observe the beauty of physics in action this past year, using electrons to observe the magnetic reversal of structures sized 100,000 times smaller than a strand of hair. No wonder why people refer to Nanotechnology as magic.



---

Hedda Christine Soland  
29th June 2023

# Acknowledgements

What is even more magical than Nanotechnology itself, is the magicians behind it, or more precisely my classmates in MTNANO kull 18. Thank you for welcoming me with open arms in 2019. You are truly a unique collection of people, which keep impressing me with each day that goes by. I wish you all the best, and for our career and life paths to cross again. Of all the beautiful people in our class, I want to raise a special toast to Susanne. She has been my partner in crime, at the lab, amongst friends and at home. I truly cherish the many memories we have shared over the years. Never change, and always remember to go out to the sea from time to time. I would also like to thank the other residents of Villa Nidarøy for so many wonderful years where new and old friendships have bloomed, and my besties Vilde, Ingvild and Kaja for all the joy and laughter you have brought into my life. I am quite certain our strong friendship continues throughout the chapters of life, even though this one closes. Thank you also to my family - my mom, dad and my sisters. You have always and will forever continue to inspire me. I hope you are proud and I know you will continue to support me no matter what I put my peculiar mind up to.

I would like to thank Gunvor for all the fruitful discussions throughout this year. You have guided me through the realm of magnetism, which is a surprisingly challenging realm to navigate through sometimes. It has been a pleasure finishing my studies with you by my side, whether that be in Lausanne, in the mountains or at the lesesal. Additionally, I would like to express my appreciation to co-supervisor, Professor Erik Folven, for his valuable insights on magnetism and for his many good ideas, and to him and Johannes Høydahl Jensen for the interesting discussions regarding practical applications of ASIs. I will also send a big thank you to my other co-supervisor, PhD Candidate Gregory Nordahl, which has been an immense support in the lab, whether that be teaching me how to use the FIB, the TEMs or how to master my skills in paint. If you ever find yourself in need of some tips and tricks in PowerPoint, you know who to ask. I wish you all the best for the continuation of your PhD and your future career. Last, but not least, I would like to pay a special gratitude to my talented, understanding and attentive supervisor, Magnus Nord. Your visionary mind has pushed my thesis in directions I am most grateful for. Thanks to you, this work has inspired and challenged me to become a better researcher as I embark upon my journey as a PhD student at Lund University. With that being said, I have one final word describing how I feel about finishing this thesis and that is *DIGG*<sup>3</sup>.

---

<sup>3</sup>A Norwegian word most often used to describe good food, but famously used by Magnus Nord to celebrate academic victories, for example when experiments actually work in our favour.



# List of Acronyms

Note that LTEM and LM(S)TEM is here used to describe Lorentz TEM and low magnification (S)TEM, respectively.

**ADF** annular dark field

**ASI** artificial spin ice

**BF** bright-field

**DED** direct electron detector

**DPC** differential phase contrast

**EBL** electron beam lithography

**FIB** focused ion beam

**HDD** hard disk drive

**MOKE** magnetic optical Kerr-effect

**LMSTEM** low magnification STEM

**LTEM** Lorentz TEM

**MFM** magnetic force microscopy

**MRI** magnetic resonance imaging

**OL** objective lens

**PEEM** photoemission electron microscopy

**pwASI** pinwheel ASI

**STEM** scanning transmission electron microscopy

**sqASI** square ASI

**TEM** transmission electron microscope

**XMCD** x-ray magnetic circular dichroism

## Dimensions of ASI Islands

**XL** 1800nm×600nm

**L** 900nm×300nm

**M** 600nm×200nm

**S** 450nm×150nm

**XS** 225nm×75nm

# Contents

|   |            |
|---|------------|
| <b>Abstract</b>   | <b>i</b>   |
| <b>Sammendrag</b>   | <b>ii</b>  |
| <b>Preface</b>  | <b>iii</b> |
| <b>Acknowledgements</b>   | <b>iv</b>  |
| <b>List of Acronyms</b>   | <b>v</b>   |
| <b>Dimensions of ASI Islands</b>                                      | <b>vi</b>  |
| <b>1 Introduction</b>   | <b>1</b>   |
| 1.1 Motivation . . . . .  | 1          |
| 1.2 Background . . . . .  | 1          |
| 1.3 Objectives . . . . .  | 3          |
| <b>2 Theoretical Framework</b>  | <b>4</b>   |
| 2.1 Magnetism and Magnetic Materials . . . . .                        | 4          |
| 2.1.1 An Introduction to the Magnetic Field Inside a Magnet . . . . . | 4          |
| 2.1.2 Types of Magnetism . . . . .                                    | 5          |
| 2.1.3 Micromagnetic Energy Contributions . . . . .                    | 5          |
| 2.1.4 Magnetic Domains . . . . .                                      | 8          |
| 2.1.5 Hysteresis . . . . .  | 9          |
| 2.1.6 Magnetic Frustration . . . . .                                  | 10         |
| 2.1.7 Artificial Spin Ice . . . . .                                   | 10         |
| 2.2 Magnetic Imaging in TEM . . . . .                                 | 12         |
| 2.2.1 STEM-DPC . . . . .  | 12         |
| <b>3 Materials and Methods</b>  | <b>15</b>  |
| 3.1 Sample Fabrication . . . . .                                      | 16         |
| 3.1.1 Bitmap Design . . . . .   | 16         |
| 3.1.2 Material . . . . .  | 19         |
| 3.1.3 FIB Milling . . . . .   | 19         |
| 3.2 LSTEM imaging with an ADF Detector . . . . .                      | 20         |
| 3.2.1 STEM-DPC with an ADF detector . . . . .                         | 21         |

|          |  |           |
|----------|--|-----------|
| 3.2.2    | Processing of ADF-STEM-DPC Data . . . . .                        | 23        |
| 3.2.3    | Continuous Tilt STEM-DPC . . . . .                               | 25        |
| <b>4</b> | <b>Results &amp; Discussion I</b>                                |           |
|          | <b>Sample Fabrication</b>  | <b>27</b> |
| 4.1      | The Path Towards XS-Sized ASI Islands . . . . .                  | 27        |
| 4.1.1    | Optimizing Milling Parameters . . . . .                          | 28        |
| 4.1.2    | Mask Design: Bitmap Resolution and Beam Overlap . . . . .        | 28        |
| 4.1.3    | Probe Size: Milling Efficiency and Precision . . . . .           | 32        |
| 4.1.4    | Milling Strategy: Channelling Reduces Sputtering Yield . . . . . | 33        |
| 4.2      | Summary and Future Directions: Fabrication . . . . .             | 34        |
| <b>5</b> | <b>Results &amp; Discussion II</b>                               |           |
|          | <b>Characterization</b>  | <b>35</b> |
| 5.1      | LMSTEM Alignment Procedure . . . . .                             | 35        |
| 5.1.1    | Using a Milled Circle as a Compass and Alignment Tool . . . . .  | 36        |
| 5.1.2    | An Attempt to Reach the Ground State of sqASI . . . . .          | 37        |
| 5.1.3    | Correction of Coma . . . . .                                     | 38        |
| 5.1.4    | Magnetic Contrast . . . . .                                      | 39        |
| 5.2      | Diffraction Effects . . . . .                                    | 41        |
| 5.3      | Analysis of ADF STEM-DPC Data . . . . .                          | 44        |
| 5.3.1    | The Square Lattice . . . . .                                     | 44        |
| 5.3.2    | The Pinwheel Lattice . . . . .                                   | 49        |
| 5.3.3    | Combining ADF-STEM-DPC and Sample Tilt . . . . .                 | 52        |
| 5.4      | Analysis of Continuous Tilt STEM-DPC Data . . . . .              | 54        |
| 5.5      | Summary of the Findings: Characterization . . . . .              | 57        |
| <b>6</b> | <b>Conclusion and Further Work</b>                               | <b>60</b> |
|          | <b>References</b>  | <b>61</b> |
| <b>A</b> | <b>Problems Tackled Along the Way</b>                            | <b>65</b> |
| <b>B</b> | <b>Extra STEM-DPC Data</b>                                       | <b>67</b> |
| <b>C</b> | <b>The Kagome Lattice</b>  | <b>68</b> |
| <b>D</b> | <b>Magnetic Field Measurements of the OL</b>                     | <b>69</b> |

# List of Figures

|      |  |    |
|------|--|----|
| 2.1  | Types of magnetism . . . . .   | 5  |
| 2.2  | Magnetostatic energy and the demagnetization field . . . . .                           | 7  |
| 2.3  | Easy and hard axis . . . . .   | 8  |
| 2.4  | Magnetic domains . . . . .   | 9  |
| 2.5  | Hysteresis curve . . . . .   | 10 |
| 2.6  | Groundstate for sqASI and pwASI . . . . .  | 11 |
| 2.7  | STEM-DPC with a pixelated detector . . . . .   | 13 |
| 3.1  | Method flowchart . . . . .   | 15 |
| 3.2  | Geometries of a pinwheel vertex . . . . .  | 16 |
| 3.3  | FIB milling procedure . . . . .  | 19 |
| 3.4  | STEM-DPC setup with an ADF detector . . . . .  | 21 |
| 3.5  | Data processing of ADF-STEM-DPC data . . . . .   | 24 |
| 3.6  | Continuous Tilt STEM-DPC . . . . .   | 25 |
| 3.7  | Probe position on the ADF detector . . . . .   | 26 |
| 4.1  | Bitmap resolution . . . . .  | 29 |
| 4.2  | Resolution and size of bitmap dictate ion beam overlap . . . . .                       | 30 |
| 4.3  | Varying size of milled area . . . . .  | 31 |
| 5.1  | Calibration circle . . . . .   | 36 |
| 5.2  | Tilting to groundstate . . . . .   | 38 |
| 5.3  | Magnetic contrast and OL strength . . . . .  | 40 |
| 5.4  | Channeling effects when varying milling angle . . . . .                                | 42 |
| 5.5  | Diffraction contrast is reduced by tilting the specimen off the milling axis . . . . . | 43 |
| 5.6  | DPCy is independent of diffraction contrast . . . . .                                  | 43 |
| 5.7  | ADF-STEM-DPC data of an S-sized sqASI . . . . .  | 45 |
| 5.8  | Observed vertex states in sqASI . . . . .  | 45 |
| 5.9  | ADF-STEM-DPC image of XS sqASI . . . . .   | 46 |
| 5.10 | Observed vertex states in pwASI . . . . .  | 49 |
| 5.11 | Size of ASI islands changes the emergent behaviour of the system . . . . .             | 50 |
| 5.12 | Stray fields from neighbouring islands . . . . .                                       | 51 |
| 5.13 | ADF-STEM-DPC showing domains in XL-sized islands . . . . .                             | 52 |
| 5.14 | Tilt series of a square array with L-sized islands . . . . .                           | 54 |
| 5.15 | Dynamic tilted STEM-DPC series of an XS-sized pinwheel . . . . .                       | 55 |

|      |   |    |
|------|---|----|
| 5.16 | Switching data of pw M versus pw M spaced . . . . .                     | 56 |
| 5.17 | Switching data of pw S versus sq S . . . . .                            | 57 |
| A.1  | Challenges met during FIB milling . . . . .                             | 65 |
| B.1  | Dynamic tilted STEM-DPC series of an XS-sized pinwheel . . . . .        | 67 |
| D.1  | Measured flux density when OL is off as a function of specimen tilt . . | 69 |
| D.2  | Measured flux density as a function of OL strength . . . . .            | 70 |



# Chapter 1

## Introduction

### 1.1 Motivation

Every day, we are surrounded by magnetic devices, from the speakers in our phones and the internal hard disk drives (HDDs) in our computers to the powerful magnets utilized in magnetic resonance imaging (MRI) machines at the hospital. Magnetic materials have existed since long before us and were first studied by ancient civilisations dating back to 600 BCE. In modern-day life, magnetic materials play an important role, and it seems like their importance will only continue to grow in the future. With the rapid technological advances in our society, power consumption is already skyrocketing, showcasing that there is a pressing demand for low-power devices for information storage and computing that goes beyond traditional silicon-based semiconductor technology. As devices shrink to extremely small sizes, heat dissipation becomes a major obstacle and Moore's Law<sup>1</sup> is becoming increasingly more challenging to sustain. The field of spintronics, however, aims to create novel, more energy-efficient devices by coupling electric and magnetic properties, eliminating many of the problems traditional semiconductor technology face. Therefore, understanding emergent magnetic properties at the nanoscale is crucial to realize the technological advancements that are needed to push our society forward.

### 1.2 Background

A metamaterial<sup>2</sup> that has shown great promise in spintronic applications, and is believed to play an important role in tomorrow's technology, is artificial spin ice (ASI) [1]. ASIs are composed of single-domain nanomagnets, put in a geometrical lattice, which are coupled through their stray fields [1–4]. Since their discovery in 2006 by Wang et. al. [2], ASIs have been extensively studied as model systems to explore magnetic frustration, but have recently shown great promises in applications such as low-power data storage and as reservoir computing [5–11]. The research field predominantly relies

---

<sup>1</sup>The number of transistors on a chip doubles approximately every two years

<sup>2</sup>A material that shows properties beyond its constituents.

on computer simulations [6, 9, 10, 12], with only small-scale logical operations realized thus far, leaving the practical utilization of these structures unknown [1]. However, experiments and simulations show that ASIs have a unique response to external stimuli such as temperature [13] and magnetic fields [3, 14–17]. This response can be modified through a vast parameter space, including size, shape and ratio [18], thickness [15], and lattice configuration [15, 16], resulting in countless possibilities when it comes to engineering novel devices with ASIs. To achieve effective coupling of ASI structures, it is essential to fabricate single-domain magnets with large stray fields in close proximity to each other. Single domain magnets are typically obtained below a specific size threshold, as size dictates the energy contributions that control whether magnetic domains are formed or if the excess energy is stored in the surrounding stray field [19, 20]. This requires high-quality fabrication of small enough structures, with relatively small spacing so the islands feel neighbouring stray fields. Additionally, to properly study the magnetic properties of these systems, there is a need for efficient, high-quality techniques that can study the magnetic properties at nanometer-length scales while applying external stimuli such as magnetic fields. Current magnetic characterization techniques face challenges in terms of accessibility, cost, time-consuming fabrication procedures, long acquisition times, spatial resolution and difficulties in applying external stimuli. State-of-the-art magnetic characterization methods like x-ray magnetic circular dichroism photoemission electron microscopy (XMCD-PEEM) require a synchrotron, which is not always found around the corner. A more available instrument like magnetic force microscopy (MFM) is exceptional for imaging magnetic structures in the vicinity of external magnetic fields, but has long acquisition times and is not well-suited for magnetic reversal experiments. Magnetic optical Kerr-effect (MOKE) has a spatial resolution limited by the diffraction limit of light and electron holography requires an electrostatic biprism installed on the transmission electron microscope (TEM). TEM however, is a versatile and well-established instrument which in scanning (STEM) mode can image materials down to single atomic columns. It is typically used for structural and chemical characterization, but can also be used to image internal magnetic fields in materials by utilizing the Lorentz force. This force leads to a deflection of the electron beam, which can be detected on any standard STEM detector [20–22], resulting in a visual representation of the local magnetization direction for all in-plane directions of the magnetic field created by the specimen [23, 24]. By turning off the objective lens (OL) of the microscope, the magnetic states of the specimen can be captured in a near-field-free environment. This weak residual field from the OL can be utilized by tilting the specimen, enabling the possibility to image magnetic reversal and switching of ferromagnetic domains in materials down to the nanoscale. That STEM-DPC shows such detailed information about in-plane magnetization distinguishes it from other magnetic characterization techniques. Other much-used techniques are e.g. limited by only showing two magnetic directions (XMCD) [3, 25], only dipole-dipole interactions (MFM) [2, 15] or only domain walls (Fresnel) [14]. Additionally, because it is a STEM technique, it is not difficult to apply and adjust external stimuli such as temperature and magnetic field with good precision by using dedicated holders, or by tuning the current through the OL. However, a disadvantage

to STEM-DPC is that it can be difficult to extract information about the quantitative magnetic field, ergo the absolute value of the magnetic fields within the materials. This can however be resolved using Foucault imaging or STEM-DPC with a pixelated detector [26–28].

### 1.3 Objectives

This thesis aims to address two key objectives. The first objective is to efficiently fabricate and then characterize emergent magnetic properties of complex magnetic systems like ASIs, using the instruments at disposal. This includes a focused ion beam (FIB) for the fabrication procedure, and a non-aberration corrected Jeol JEM-2100F STEM for magnetic characterization. The second objective is to study these structures and establish whether the observations made are indicators of true ASI behaviour, or just arrays of independent magnets responding to external stimuli. Demonstrating such behaviour would validate that by *only* using FIB and STEM, it is indeed possible to manufacture and characterize ASI structures in a fast and efficient way, facilitating rapid prototyping and high-quality magnetic imaging of novel magnetic systems. While electron beam lithography (EBL) is commonly used for ASI fabrication, we adopted a different approach utilizing FIB patterning, which is often used to prepare samples for TEM experiments. The optimization of the FIB procedure involved an extensive exploration of various parameters to obtain the best possible results. For characterization, STEM-DPC was used in low-magnification STEM (LMSTEM), also called OL-off mode. However, STEM-DPC set-ups often-most require a segmented or pixelated detector, which is less common than conventional STEM detectors. This project aims to extend the magnetic characterization method by using a conventional annular dark field (ADF) detector. Using the ADF detector for STEM-DPC can be a huge benefit when it comes to imaging larger structures, data storage and post-processing of data. Most STEM-DPC data sets acquired in this work span around  $15\mu\text{m}^2$  per image with a pixelation of  $3072\times 3072$ , resulting in less than 200MB per data set. Using the ADF detector even introduces new possibilities for in-situ magnetic reversal studies. With only a few months of practice, the kind of work presented here can even be performed by a master’s student and should therefore also be feasible for the more experienced scientist.

## Chapter 2

# Theoretical Framework

This chapter is meant to work as an introduction to the physical phenomena relevant to this project. Considering the wide scope of the project, we will only cover essential terminology necessary to understand the physical concepts of magnetic materials and how we can utilize the Lorentz force to characterize such materials in TEM. Basic TEM theory is considered known by the reader. Theory about magnetism is mostly based on Magnetism and Magnetic Materials by J. M. D. Coey [20] and Fundamentals of Magnetism by M. Getzlaff [21].

### 2.1 Magnetism and Magnetic Materials

In order to understand the Lorentz force and how to practically utilize this phenomenon for the characterization of magnetic materials, it is helpful to first introduce some key concepts in magnetism.

#### 2.1.1 An Introduction to the Magnetic Field Inside a Magnet

All magnetic materials exhibit a magnetic field  $\mathbf{B}$ , which is dependent on the dipole moment per volume (magnetization)  $\mathbf{M}$  of the material and any external magnetic field  $\mathbf{H}$ , times the vacuum permeability  $\mu_0$ , as shown in Equation 2.1.

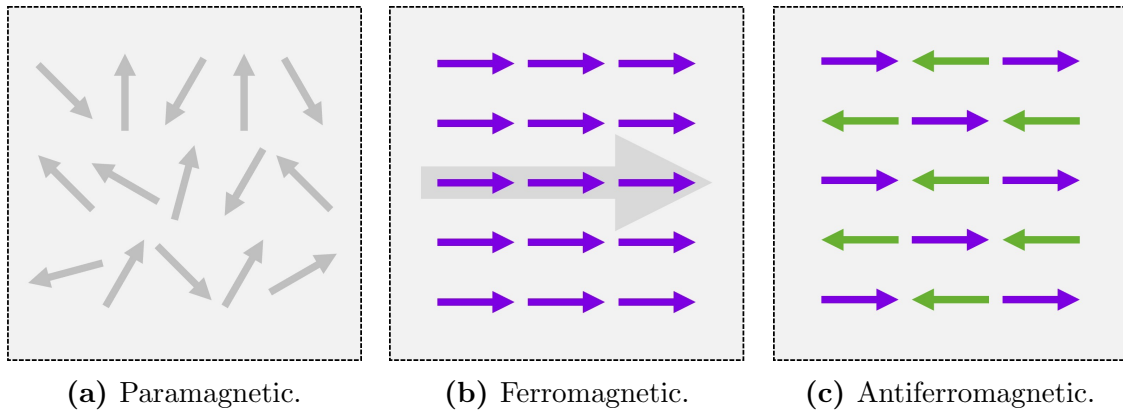
$$\nabla \cdot \mathbf{B}, \quad \mathbf{B} = \mu_0(\mathbf{H} + \mathbf{M}) \quad (2.1)$$

The external magnetic field can be parted into  $\mathbf{H} = \mathbf{H}_0 + \mathbf{H}_d$  where  $\mathbf{H}_0$  is here used to define the externally applied field and  $\mathbf{H}_d$  is the demagnetization field, or stray field, that is created by the material as a means to minimize  $\mathbf{M}$ . Logically,  $\mathbf{H}_d$  must therefore be directed in the opposite direction to  $\mathbf{M}$  and  $\mathbf{B}$  (within the material), creating a conservative field ( $\nabla \times \mathbf{H} = 0$ ) with closed flux lines. Another way to differentiate between  $\mathbf{H}_0$  and  $\mathbf{H}_d$  is in terms of free and bound currents.  $\mathbf{H}_0$  arises due to free currents such as electrons in a wire. In TEM, we could talk about  $\mathbf{H}_0$  when referring to the magnetic field from the electromagnetic lenses in the system. Whereas  $\mathbf{H}_d$  is due to bound currents in the magnetized matter, such as in a magnetic specimen.

Magnetization  $\mathbf{M}$ , which indicates the magnetic moment per unit volume of the material, can be expressed as  $\mathbf{M} = \chi\mathbf{H}$ , where the material-specific parameter  $\chi$ , known as magnetic susceptibility, represents the material's capacity to align with  $\mathbf{H}$ . Depending on the nature of the material, the magnetic susceptibility can either be positive (paramagnetic or ferromagnetic materials) or negative (diamagnetic materials).

### 2.1.2 Types of Magnetism

In the case of positive magnetic susceptibility  $\chi$ , there are three magnetic configurations to consider: paramagnetism, ferromagnetism, and antiferromagnetism as illustrated in Figure 2.1. Paramagnetic materials (Figure 2.1a) have a small, but positive  $\chi$ , resulting in a weak alignment to an external magnetic field. Ferromagnetic materials (Figure 2.1b), on the other hand, possess a large  $\chi$  and spontaneous magnetization even in the absence of an external field, with neighbouring spins aligning in parallel to produce a strong overall magnetization. Although, above a certain temperature  $T_C$ , the ferromagnetic material becomes paramagnetic. Antiferromagnetic materials (Figure 2.1c) also have neighbouring atomic magnetic moments aligned, but they align in a mutually opposing manner, resulting in a net magnetic moment of zero.



(a) Paramagnetic.

(b) Ferromagnetic.

(c) Antiferromagnetic.

**Figure 2.1: Types of magnetism** | Magnetic moments align differently in paramagnetic, ferromagnetic and antiferromagnetic materials. Magnetization for the different types is illustrated without applying any external field.

### 2.1.3 Micromagnetic Energy Contributions

The alignment of magnetic moments in a material plays a crucial role in determining its emergent magnetic properties. In bulk<sup>1</sup> ferromagnetic materials, the magnetic moments align themselves into magnetic domains to minimize the system's magnetostatic energy  $E_{MS}$ , which is one of several energy contributions that influence the overall behaviour of a magnetic system. The total energy  $E_{Tot}$ , of the system, is governed by

<sup>1</sup>Magnetic structures within the nano range may behave differently.

four major energy contributions: the Zeeman energy  $E_{Zeeman}$ , the exchange energy ( $E_{Ex}$ ), the magnetocrystalline anisotropy  $E_{anis}$ , as well as the magnetostatic energy. This is shown in Equation 2.2.

$$E_{Tot} = E_{Ex} + E_{anis} + E_{MS} + E_{Zeeman} \quad (2.2)$$

The process of a material system reaching its most energetically favourable state often involves a compromise between energy contributions that favour conflicting outcomes. In the following, we will explore three key energy contributions that are relevant for understanding the behaviour of our systems, namely  $E_{MS}$ ,  $E_{Ex}$  and  $E_{Zeeman}$ . In the case of the material under consideration, Ni<sub>80</sub>Fe<sub>20</sub> (Permalloy),  $E_{anis}$  can be neglected and will not be further discussed. This is due to the fact that Permalloy exhibits a vanishingly small magnetocrystalline anisotropy and magnetostriction, despite its high magnetic permeability [29].

### Exchange Energy

The exchange energy is a quantum mechanical effect that arises from the interactions between neighbouring electrons in a ferromagnetic material. It is governed by the Pauli Exclusion Principle and electrostatic interactions. When considering two neighboring electrons with spin angular momenta  $\mathbf{S}_1$  and  $\mathbf{S}_2$ , the exchange energy can be expressed as,

$$E_{Ex} = -2JS_1 \cdot \mathbf{S}_2 = -2JS^2 \cos \theta_{12} \quad (2.3)$$

where  $J$  is the exchange integral and  $\theta_{12}$  is the angle between the spins. The exchange interaction is a short-range interaction which prefers to align neighbouring spins parallel in order to minimize Coulombic repulsion. However, spin alignment in magnetic materials is not solely determined by the exchange energy but is an interplay between the exchange energy and the magnetostatic energy. If an external field is applied, Zeeman energy must also be taken into consideration. For now, we will assume that it is not.

### Magnetostatic Energy and Demagnetization Field

Previously, it was mentioned that the demagnetization field  $\mathbf{H}_d$  is generated by the material to diminish the magnetization  $\mathbf{M}$  and that it is a conservative field, and must therefore always have closed flux lines. This is most easily done by arranging into magnetic domains, as depicted in Figure 2.2c. This configuration is famously called the Landau pattern and is effectively minimizing the energy  $E_{MS}$  stored in the demagnetization field because  $\mathbf{H}_d = 0$ . The mathematical expression for  $E_{MS}$  is,

$$E_{MS} = -\frac{1}{2}\mu_0 \int \mathbf{H}_d \cdot \mathbf{M} dV. \quad (2.4)$$

For bulk systems, magnetic domain formation is near-completely determined by  $E_{MS}$ . However, as we move from bulk to material dimensions where the order of



exchange energy  $E_{Ex}$  intersects  $E_{MS}$ , we observe that the physics changes drastically. When the dimensions are small enough, spins will align parallel to each other in order to reduce  $E_{Ex}$ , eventually resulting in single-domain magnets. This is shown in Figure 2.2a and b. Additionally, because we in Equation 2.4 integrate over volume  $dV$ , and magnetization is not constant throughout the material, the magnetostatic energy also depends on the shape of our structure. Different shapes are attributed with a demagnetization factor  $N_d$ . For example, elongated rod-like structures ( $N_d < 0.1$ ) show lower values than spherical structures ( $N_d = \frac{1}{3}$ ). Shape anisotropy is an important factor to consider when tailoring magnetic materials. By modifying the shape, we can force the structure to align in certain ways.

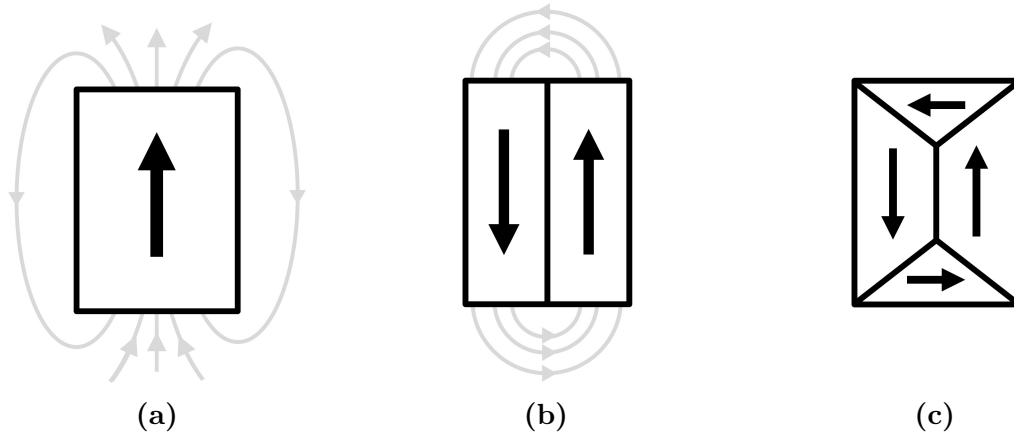


**Figure 2.2: Magnetostatic energy and the demagnetization field** | Magnetic domains result in lower  $E_{MS}$ . If, for some reason, it is not favourable to create magnetic domains, magnetostatic energy will be stored in the demagnetization field depicted in grey. (a) High  $E_{MS}$  (b) Low  $E_{MS}$  (c) No  $E_{MS}$  energy in a perfect Landau-pattern.

The magnetic moments want to align along the longest axis of the structure, known as the easy axis, as this is the configuration which minimizes demagnetization energy. The opposite is true for the hard axis. For dimensions small enough, we can assume single-domain behaviour, and thus the magnetization will align left/right for horizontal magnets and up/down for vertical magnets [6]. An example of this is shown for a single-domain magnet with length  $l$ , and width  $w$ , in Figure 2.3a. Because the energy in the demagnetization field will be minimized when magnetization is along  $l$ , this is also the easy axis. If an external magnetic field is applied along the hard axis, the magnet will not necessarily align with that field. This is due to the strongly preferred magnetization along the easy axis. The magnetization direction depends on the strength of  $\mathbf{H}_0$ ,  $N_d$  and  $\chi$ .

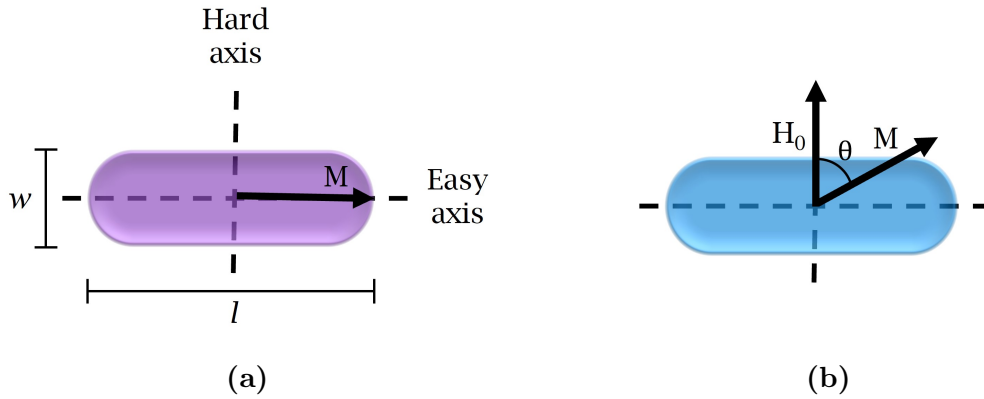


**Figure 2.3: Easy and hard axis** | (a) A single-domain magnet with  $l/w$ -ratio 3:1, with a net  $\mathbf{M}$  along the easy axis. It is energetically unfavourable for the magnetic spins to align along the hard axis. (b) Magnetization is not necessarily parallel to an applied field  $\mathbf{H}_0$  unless applied along the easy axis <sup>2</sup>.

### Zeeman Energy

When an external magnetic field  $\mathbf{H}_0$  is applied, such as in Figure 2.3b, the magnetic moments in the material will align themselves with the field to minimize the energy in the system. This is referred to as Zeeman interaction. The Zeeman energy  $E_Z$  is directly proportional to the scalar product of each magnetic moment  $\mu_{spin}$  and  $\mathbf{H}_0$ . Therefore, the Zeeman energy is minimized when the magnetic moments are aligned in the direction of the applied field. However, to align all the magnetic moments with  $\mathbf{H}_0$ , the applied field must overcome the demagnetization energy,  $E_{MS}$ . The alignment of magnetic moments with  $\mathbf{H}_0$  is thus a compromise between lowering  $E_Z$  and  $E_{MS}$ .

#### 2.1.4 Magnetic Domains

Magnetic domains are regions within a magnetic material where the dipole moments align in a coordinated manner. These domains form because the material wants to minimize  $E_{MS}$ , as discussed previously. Each magnetic domain acts like a tiny magnet with its own north and south poles. The boundaries between domains are called domain walls and come with an energy cost due to the rotation of dipole moments, and thus higher  $E_{Ex}$ . In an unmagnetized ferromagnetic material (Figure 2.4a), the domains are randomly oriented, resulting in a net magnetization of zero. However, when an external magnetic field is applied, the domains can align with the field (Figure 2.4b). This alignment process, known as magnetic domain reorientation, is responsible for the magnetic response and behaviour of the material. Materials with higher magnetic permeability  $\mu_r$ , align more easily with  $H_0$ .

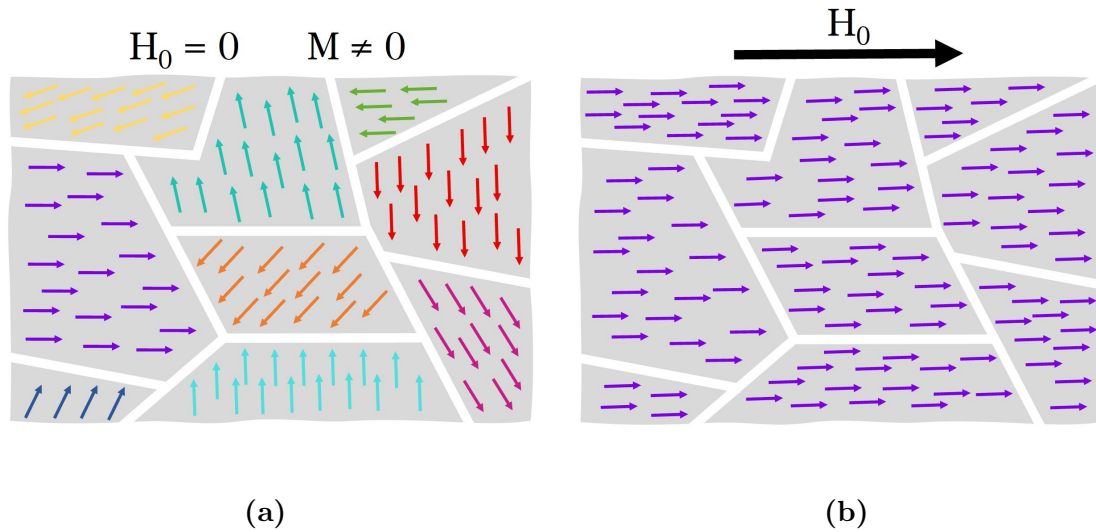


**Figure 2.4: Magnetic domains** | (a) In a bulk ferromagnetic material, magnetic domains are formed, aligned in a way so the net magnetization becomes zero. (b) If an external magnetic field  $\mathbf{H}_0$  is applied, the magnetic moments will align with this field, resulting in a non-zero net magnetization.

### 2.1.5 Hysteresis

The behaviour of hysteresis in ferromagnetic materials can be effectively illustrated through a hysteresis curve, as depicted in Figure 2.5. This provides a visual representation of the relationship between an applied magnetic field and resulting magnetization, highlighting important parameters such as magnetic saturation, remanence and coercivity.

When an external magnetic field is applied to a ferromagnetic material, its magnetization aligns with the field, reaching a point of saturation where a further increase in the field does not significantly affect the magnetization. This maximum magnetization is known as magnetic saturation,  $M_s$ . Upon decreasing the applied field, the magnetization does not instantly return to zero but retains a residual magnetization called remanence,  $|M_r|$ . To completely demagnetize the material, a field in the opposite direction must be applied. At the point where the strength of the opposing magnetic field drives the magnetization to zero, we have reached the point of coercivity,  $|H_c|$ . Before completely aligning the dipole moments in the opposite direction (at  $-M_s$ ), again reaching magnetic saturation,  $|M_s|$ .

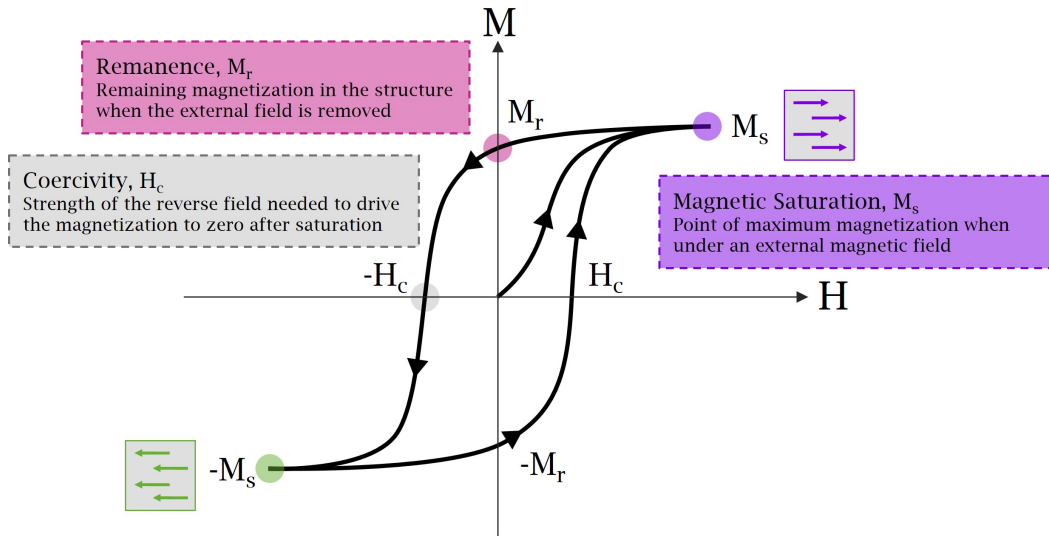


**Figure 2.5: Hysteresis curve** | Hysteresis curve describing the relationship between an applied magnetic field and alignment of magnetic moments. Magnetic saturation, remanence and coercivity are highlighted on the graph along with the respective definition.

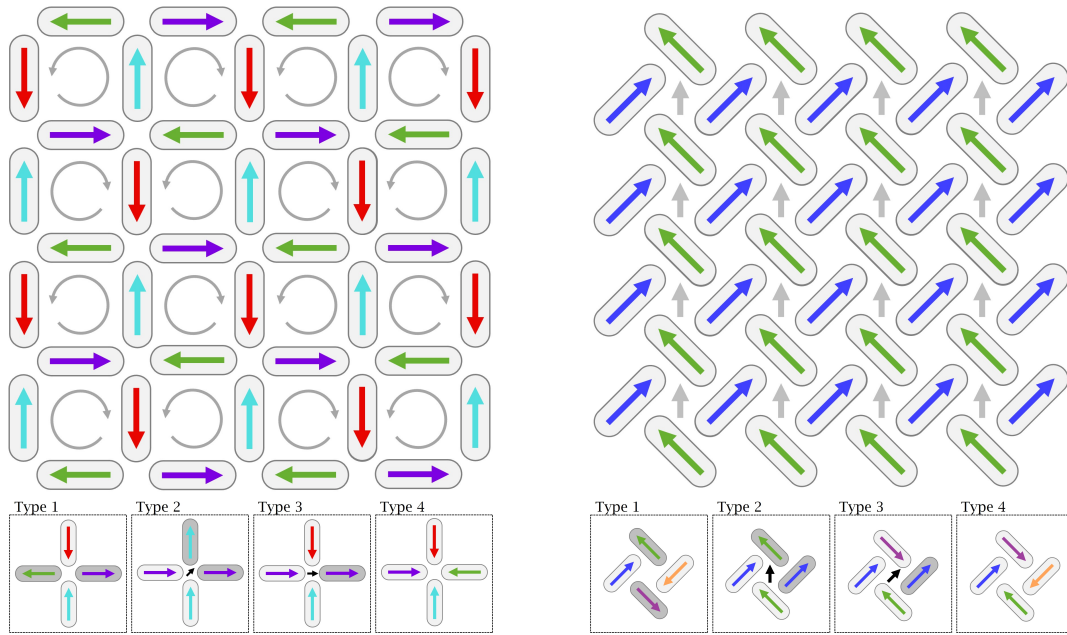
### 2.1.6 Magnetic Frustration

Magnetic frustration is a phenomenon that arises in certain magnetic materials, particularly those with a lattice structure that does not allow all the magnetic interactions to be simultaneously satisfied. This leads to a state of competing magnetic interactions, resulting in a frustrated magnetic system. In such systems, it becomes challenging for the magnetic moments to arrange themselves in a unique, low-energy configuration. Instead, they can adopt various configurations or exhibit collective behaviour, such as spin ice. Magnetic frustration is of great interest in the study of condensed matter physics and has implications for understanding magnetic materials with complex behaviour and emergent properties.

### 2.1.7 Artificial Spin Ice

ASIs are magnetically frustrated systems built up of nano-sized, and thus single-domain, magnetic islands and can be arranged in a variety of different patterns, such as square (sq) and pinwheel (pw) (see Figure 2.6) [1]. Because each island is single-domain, its magnetization is forced by shape anisotropy to align in one of two directions. Each island can therefore be treated as a single magnetic moment. The islands are coupled together through dipolar interaction, where the strength of interaction is inversely proportional to the distance between the dipoles, or magnetic islands, in this case, [21]. This interaction is what gives ASI its emergent properties, and the reason

it is classified as a metamaterial. Depending on the given configuration, the system displays various emergent magnetic properties. An example is that the groundstate of sqASI is antiferromagnetic (Figure 2.6a), whereas pwASI displays ferromagnetic properties (Figure 2.6b). However, it is important to note that ASI systems can often have degenerate ground states, meaning it exists multiple configurations with the same energy. This degeneracy allows for a rich variety of behaviours and dynamics in ASI system, making them intriguing for studying emergent phenomena and manipulating magnetic properties.



(a) sqASI prefers type 1 icing rule and is antiferromagnetic. (b) pwASI prefers type 2 icing rule and is ferromagnetic.

**Figure 2.6: Groundstate for sqASI and pwASI** | The most energetically favorable vertex configurations for sqASI and pwASI is the two-in-two-out vertex. The four vertex types are shown, together with examples of degenerate ground states for the two lattices.

Observing such a low-energy state can however be quite tricky. Because the structures are frustrated by nature, they are extremely sensitive to external stimuli, fabrication defects, temperature, thickness variations etc. Groundstate-like behaviour are however a key indicator that we do indeed have a coupled ASI system and not just an independent array of magnets. For this to occur, each island should be single-domain to maximize stray field and thus enhance the coupling between magnets. This requires small islands so that  $E_{Ex} > E_{MS}$ . Furthermore, the pitch (distance to neighbouring islands), should be small enough to ensure maximum interaction, as the stray fields from neighbouring islands decay proportional to distance. Additionally, lattice configuration will of course play a huge role. This has already been demonstrated with antiferromagnetic and ferromagnetic behaviour in sqASI and pwASI, respectively. Be-

cause of the orientation and ferromagnetic ordering of the pwASI islands, it is expected that these are more strongly coupled than sqASI islands. For any ASI system, the edge islands will be less magnetically coupled due to not having as many neighbouring islands. These islands are more easily flipped and often happen to be nucleation points for avalanches (flipping of magnetization in neighbouring islands) propagating through the structure. Based on how strongly coupled the islands are the nature of these avalanche effects may differ. These dynamic effects can be used to study our system, with and without a magnetic field applied, and is a characteristic of ASI behaviour.

## 2.2 Magnetic Imaging in TEM

Lorentz TEM (LTEM) is a collective term for TEM techniques used to investigate magnetic and electric fields at the nanoscale. When electrons (with charge  $-e$ ) travel down the TEM column at a velocity  $\mathbf{v}$ , they interact with electric ( $\mathbf{E}$ ) and magnetic ( $\mathbf{B}$ ) fields present in the specimen. This interaction results in a force that deflects the electron beam, known as the Lorentz force  $\mathbf{F}$ . Mathematically, the Lorentz force is given by:

$$\mathbf{F} = -e \cdot (\mathbf{E} + \mathbf{v} \times \mathbf{B}). \quad (2.5)$$

The magnetic field component  $B_{\parallel}$  in the sample that is parallel to the electron beam, does not cause any deflection of the beam because  $\mathbf{v} \times \mathbf{B}_{\parallel} = 0$ . As a result, LTEM techniques are sensitive only to the in-plane magnetization of a sample [22]. Albeit, this in-plane deflection of the beam can be utilized and visualized by e.g. defocusing the beam in Fresnel imaging to visualize the domain walls, or by monitoring the deflection of the beam at each scanning position using scanning TEM (STEM) - differential phase contrast (DPC).

### 2.2.1 STEM-DPC

STEM-DPC is a widely used LTEM technique that involves scanning a finely focused electron beam across the specimen to map the deflection of the beam at each scan position. Because of the relationship in Equation 2.5 and Equation 2.1, the magnetization can be mapped with spatial resolution mainly decided by the probe size [22]. Traditionally, STEM-DPC experiments have been performed using segmented detectors. These detectors divide the signal from the deflected electron beam into different segments. By subtracting the intensity signals from the opposing four segments of the detector, the orthogonal components of the in-plane magnetic induction, DPC<sub>x</sub> and DPC<sub>y</sub>, can be determined and combined into a vector plot. In recent years, pixelated detectors such as the MerlinEM detector, have become more common. These detectors can save large amounts of information in complex 4D datasets, not only containing information about the image plane but also the back focal plane for each scan position. This can be advantageous when analysing STEM-DPC data, as we have direct access



to how the beam is changing when rastering across the specimen. To obtain a magnetic induction map, a centre of mass<sup>3</sup> calculation is usually performed, linking the displacement of the electron beam with the real image of the specimen. An example of STEM-DPC with a pixelated detector is illustrated in Figure 2.7.

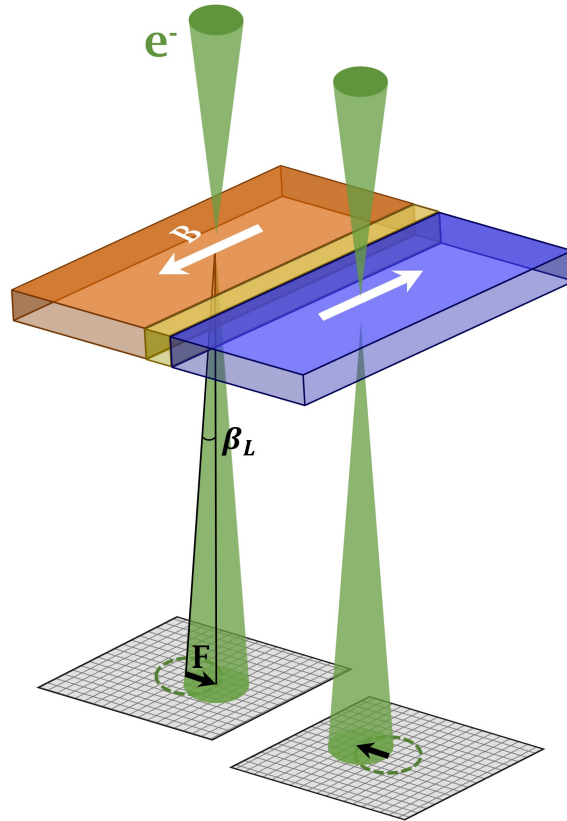


**Figure 2.7: STEM-DPC with a pixelated detector** | The incident beam is deflected by the magnetic field  $\mathbf{B}$ , present in the specimen. The angle of deflection of the electron beam caused by the Lorentz force  $\mathbf{F}$ , is annotated as  $\beta_L$ .

The magnetic induction,  $\mathbf{B}$  in each domain, is affected by magnetic fields originating from the electromagnetic lenses of the TEM system. This applies in particular for the objective lens, because of its central placement around the specimen. Therefore, during STEM-DPC experiments, the objective lens is often turned off to create a near-field-free region around the specimen. This mode is referred to as low magnification STEM (LMSTEM). However, a small residual field  $\mathbf{H}_0$  is usually present or can be introduced by slightly exciting the objective lens.  $\mathbf{H}_0$  can be utilized in experiments to investigate magnetic reversal. Tilting the specimen enables direct manipulation of the  $\mathbf{H}$ -field across the sample, indirectly affecting the deflection of the beam. Furthermore,

<sup>3</sup>The centre position of each bright field disk is calculated by a weighted average of intensity in the disk, assigning a value of beam deflection to each pixel in the scan.

the deflection is also influenced by the thickness of the sample through  $B_s \cdot t$ , where  $B_s$  is the saturation induction in the sample and  $t$  is the sample thickness [30]. This is shown in Equation 2.6, which shows that if assumed a uniform  $\mathbf{B}$ , this expression can be simplified, illustrating how thickness variations also can contribute to beam deflection.

$$\beta_L = \frac{e\lambda}{h} \int \mathbf{B} \times d\mathbf{l} = \frac{e\lambda}{h} B_s \cdot t \quad (2.6)$$

Thicker films and materials with higher magnetic permeability, and thus larger saturation magnetization, will therefore exhibit stronger magnetic contrast in STEM-DPC. This makes the technique sensitive to thickness variations across the sample, which is important to consider when fabricating samples used for imaging with the STEM-DPC technique [31].

## Chapter 3

# Materials and Methods

This chapter provides a comprehensive overview of the materials and methods employed in this study, encompassing the key steps in the fabrication, characterization, and data processing procedures. A schematic representation of the process is presented in Figure 3.1. This includes mask design and FIB milling of these structures, two distinct LTEM techniques, and the following data processing.

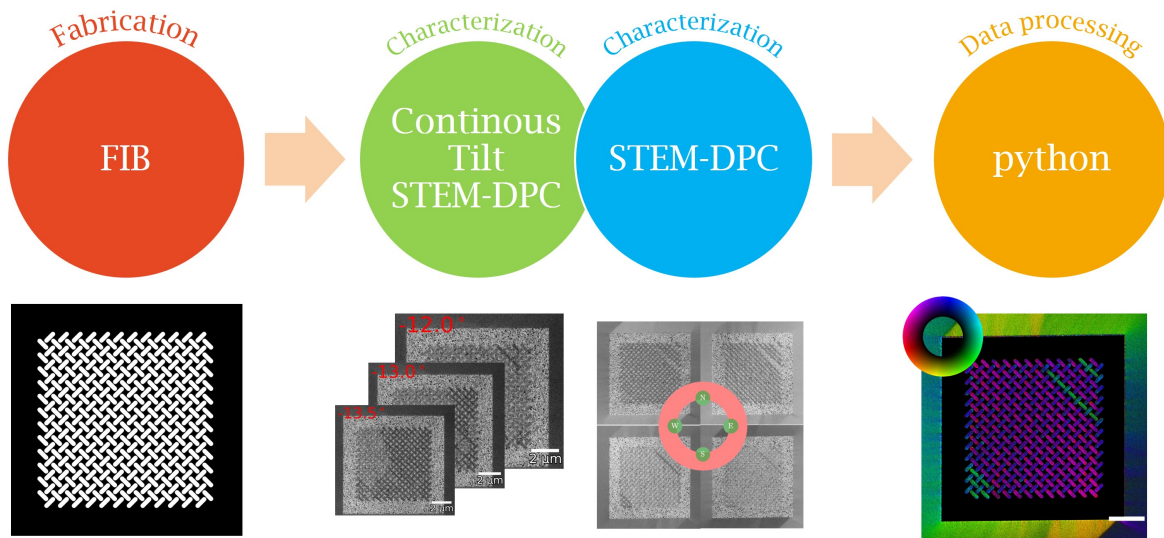


**Figure 3.1: Method flowchart** | Overview of the methodology presented in this work. All scale bars are 2  $\mu\text{m}$ .

The primary objective of this study was to investigate the behaviour of ASI structures utilizing available fabrication and characterization tools. Traditionally, ASIs are fabricated with electron beam lithography (EBL), which is known for its ability to create precise and intricate patterns in materials by selectively removing most material in between the features [2]. Although EBL is an excellent nanofabrication method, EBL fabricated samples are often incompatible with TEM, and especially STEM-DPC, due to charge build-up and height differences distorting the electron beam in unwanted ways [31]. Focused ion beam (FIB) milling was therefore the chosen fab-

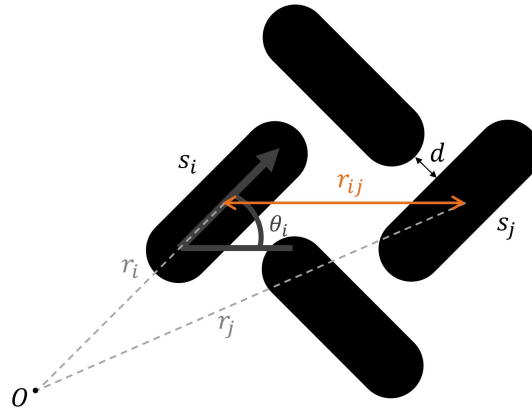
rication procedure for the purpose of this work. FIB is a fast, and highly flexible, fabrication procedure which, with an optimized milling procedure, is well-suited for efficient prototyping of nanosized magnetic patterns such as ASIs. All parts of the experimental procedures were conducted by the experimentalist herself, with the exception of the Permalloy deposition onto TEM grids, which was performed by PhD. Candidate Gregory Nordahl.

## 3.1 Sample Fabrication

In this section, we will outline the essential steps when fabricating arrays of magnetic islands in Permalloy. The fabrication process encompasses bitmap design, selection of material, and the FIB milling procedure. With precise control over the sample fabrication process, we are able to fabricate the magnetic samples necessary for the successful characterization and analysis of ASI behaviour.

### 3.1.1 Bitmap Design

The first step in sample fabrication is the design of pattern masks that are used in the FIB milling procedure. A wide range of geometries was explored, as summarized in Table 3.1. The masks were created as bitmaps using the simulation software Mumax<sup>3</sup>. By programming the bitmaps in Mumax<sup>3</sup>, we can precisely control the resolution, shape, and arrangement of the features, tailoring the bitmaps to our needs. Additionally, it facilitates future magnetic simulations which can be compared to the obtained experimental results. Such magnetic simulations have however not been included in this work.

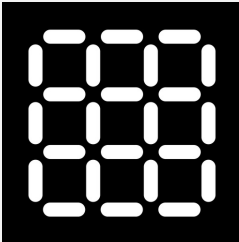
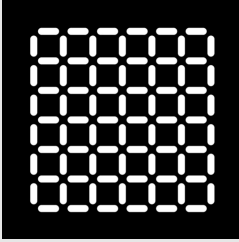
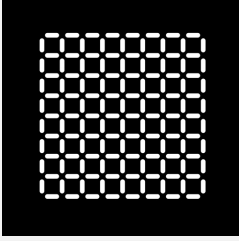
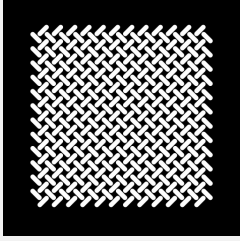
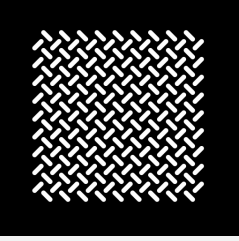
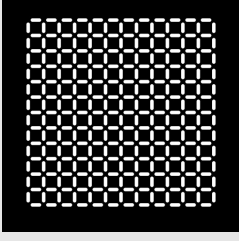
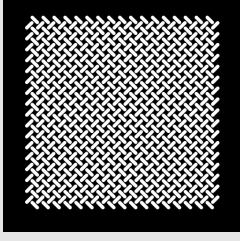
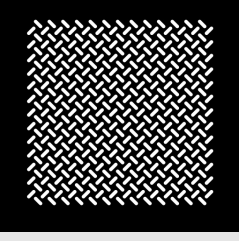
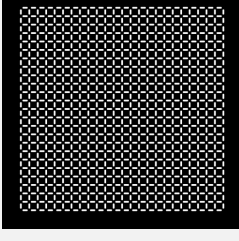
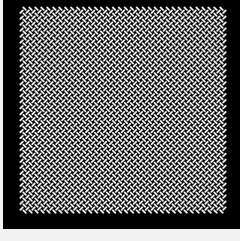
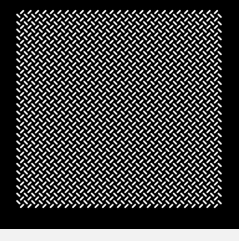


**Figure 3.2: Geometries of a pinwheel vertex** | The distance between two neighbouring islands  $s_i$  and  $s_j$  in an ASI vertex is  $r_{ij}$ . The smallest distance between each island is  $d = 30nm$  for the not-spaced pwASI. Each magnet is rotated at an angle  $\theta = \pm 45^\circ$ . Figure inspired by [12].

Figure 3.2 shows a detailed overview of the arrangement of magnetic islands in a pinwheel vertex, i.e. the building blocks of a pwASIs. The distance between two islands,  $s_i$ , and  $s_j$ , is  $r_{ij} = r_j - r_i$ . The shortest distance between neighbouring islands, often called pitch, is annotated as  $d$ . For the pwASIs,  $d = 30nm$  and  $r_{ij} = l + d$  where  $l$  is the length of each island. For the spaced pwASIs soon introduced,  $d_{spaced} = d + 75nm = 105nm$ . The spins are rotated an angle  $\theta = \pm 45^\circ$ .

The first magnetic arrays studied in this project consisted of magnets measuring  $1800nm \times 600nm$  (size XL). This was mostly because of limitations in sample fabrication, and the investigation of smaller elements was therefore initially constrained to larger sizes. Over time, improvements were made, enabling the study of smaller island sizes down to  $225nm \times 75nm$  (size XS). Therefore, in Table 3.1 we present the five island sizes: XL ( $1800nm \times 600nm$ ), L ( $900nm \times 300nm$ ), M ( $600nm \times 200nm$ ), S ( $450nm \times 150nm$ ), and XS ( $225nm \times 75nm$ ). The length-width ratio was kept constant at 3:1, as this was found to be an optimal ratio for single-domain magnets, confirmed by micromagnetic simulations and experimental studies in the preceding work of this thesis. In addition to the five sizes, three lattice configurations were studied: square (sq), pinwheel (pw), and kagome. To limit the scope of this project, the data of the kagome lattice can be found in Appendix B. More information about different ASI lattice configurations can be found in [1]. Additionally, a variant of the pinwheel lattice, *spaced pinwheel*, was studied. This version has 75nm more  $d$ -spacing between neighbouring islands. Initially, the square lattice was the primary focus of this study. However, it was later found that the pinwheel lattice exhibited more pronounced ASI behavior, thus becoming the primary focus. Because of improvements in the fabrication method, only M-, S-, and XS-sized pwASIs were studied.

**Table 3.1: Mask geometries** | An overview of the bitmaps used as milling patterns in FIB, divided by the size of each island put into different lattice configurations. The black areas were selectively removed, resulting in separated magnetic islands shown in white <sup>1</sup>. It is important to keep a large enough padding around the ASI to avoid any unwanted magnetic connection to the surrounding thin film.

| Size \ Lattice           | Square  | Pinwheel   | Spaced Pinwheel   |
|--------------------------|---|--|---|
| <b>XL</b> (1800nm×600nm) |    |  |   |
| <b>L</b> (900nm×300nm)   |   |  |   |
| <b>M</b> (600nm×200nm)   |  |  |  |
| <b>S</b> (450nm×150nm)   |  |  |  |
| <b>XS</b> (225nm×75nm)   |  |  |  |

### 3.1.2 Material

The material of choice in this study is nanocrystalline Permalloy, which is a magnetic alloy of Nickel (Ni) and Iron (Fe), typically in the composition  $\text{Ni}_{80}\text{Fe}_{20}$  as used here. Permalloy exhibits an exceptionally high magnetic permeability measured as high as  $\mu_r \approx 90000$  [32]. This makes it highly responsive to magnetic fields and easily aligns itself with them, making Permalloy suitable for use in e.g. magnetic sensor devices, data storage, and magnetic reversal experiments. Because Ni and Fe are earth-abundant elements, and it is relatively easy and cost-effective to deposit Permalloy thin films, makes it an excellent choice for rapid and exploratory research like what was conducted in this work.

### 3.1.3 FIB Milling

FIB is a well-suited tool to create high-resolution nano-patterned structures. It offers a fast and relatively simple process, making it useful for prototyping and efficient exploration of various structures. In contrast to electron beam lithography (EBL), which is commonly used for ASI fabrication, FIB is a maskless one-step process utilizing an ion beam to mill away material and transfer predefined patterns onto the surface.

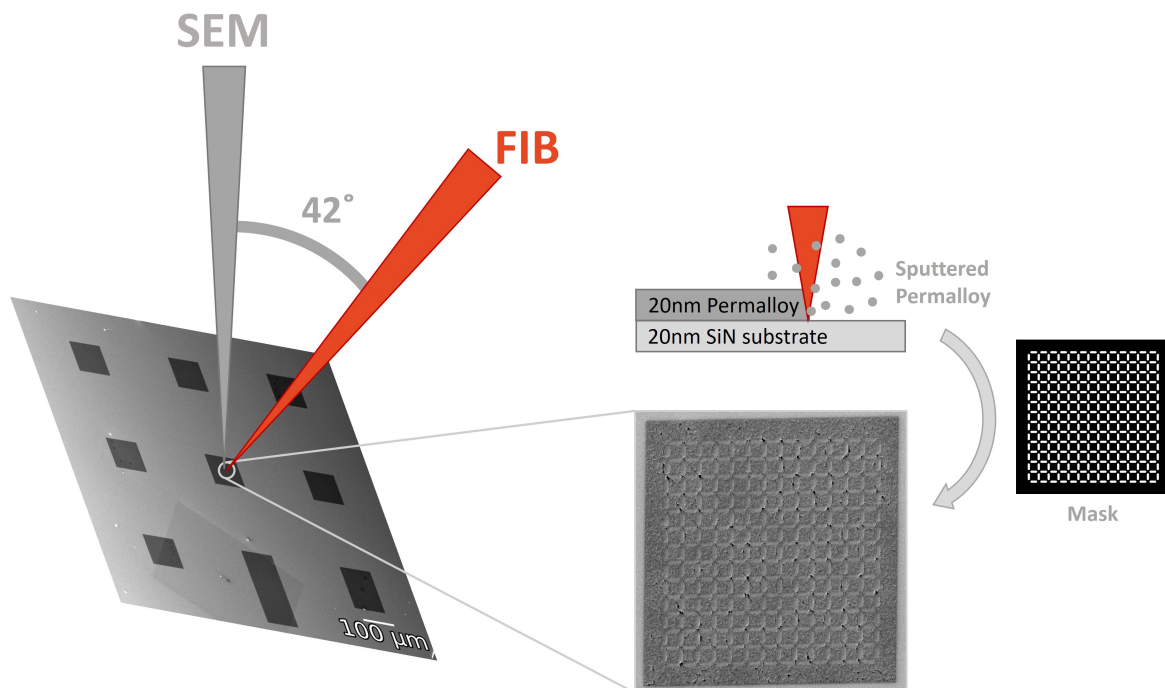


**Figure 3.3: FIB milling procedure** | Overview of the FIB milling procedure in one of the nine windows of a SiN TEM grid. A square array of  $600\text{nm} \times 200\text{nm}$  islands were milled into 20nm Permalloy thin film at a milling angle  $10^\circ$  ( $42^\circ$ ) off the normal incidence angle ( $52^\circ$ ). The corresponding bitmap is shown to the right.

The TEM grids used to host the magnetic structures in this work have a frame thickness of  $100\mu\text{m}$  and a window thickness of  $20\text{nm}$ . The grid contains nine windows, each measuring  $100\mu\text{m}\times 100\mu\text{m}$ , except for one larger window with dimensions of  $350\mu\text{m}\times 100\mu\text{m}$ . An example of such TEM grid can be seen to the left in Figure 3.3. Before FIB milling,  $20\text{nm}$  Permalloy was deposited onto the silicon nitride (SiN) TEM grids with a Pfeiffer Vacuum Classic 500 e-beam evaporator at NTNU NanoLab. To prepare the specimen for FIB patterning, the TEM grid was mounted on a stub using copper tape to prevent drift due to charge build-up. The FEI Helios G2 DualBeam FIB was utilized, accelerating high-energy  $\text{Ga}^+$  ions onto the specimen to precisely remove atoms in specified patterns (see Table 3.1). The scanning electron microscope (SEM) column was used to monitor the milling process. The ion beam was tilted  $42^\circ$  relative to the SEM column, resulting in a  $10^\circ$  tilt off the sample normal. The beam was then scanned across the sample using the serpentine scanning path, possibly leading to a higher material removal rate than the raster scanning path [33]. The milling process causes the Permalloy in the milled areas to lose its magnetic properties due to removal of material,  $\text{Ga}^+$  implantation, or a combination of the two. The FIB was set to an ion beam energy of  $30\text{kV}$  to obtain high lateral resolution and sputter yield [34, 35], with an ion beam current of  $27\text{pA}$  for high efficiency when milling structures measuring  $10.24\mu\text{m}\times 10.24\mu\text{m}$ . Dwell time was set to  $500\text{ns}$  and amount of passes to  $20,000$ . The parameter choices were done based on an experimental approach, inspired by Urbànek et. al. [34].

## 3.2 LSTEM imaging with an ADF Detector

As described in section 2.2, the Lorentz force causes the electron beam to deflect as it scans across magnetic domains. This deflection can be detected as a magnetic signal and analyzed in various ways depending on the type of detector used. However, segmented or pixelated detectors, which are not always available in all TEMs, are required for such analysis. In this study, magnetic imaging was performed using a conventional ADF detector on a non-aberration corrected Jeol JEM-2100F operating in LMSTEM mode at an acceleration voltage of  $200\text{kV}$ . To achieve maximum magnetic sensitivity, meaning enabling the detection of smaller deflections of the beam, the smallest condenser aperture ( $10\mu\text{m}$ ) was used. Additionally, the projector lens value was set to maximum to ensure a large camera length to enhance magnetic sensitivity.

Two LTEM methods utilizing the ADF detector were employed in this study. The first method aimed at creating a STEM-DPC vector map of magnetic induction by acquiring four images from orthogonal positions on the ADF detector. These four images were then combined in post-acquisition processing to create a composite DPC image. The second method involved in-situ exploration by continuously tilting the sample, acquiring one image at each tilt, therefore only registering deflection in one direction. Each data set required an acquisition time of approximately five minutes, which could vary based on the number of pixels in the image and dwell time settings. However, it is worth noting that automating the process can significantly improve the efficiency of data acquisition for these two methods, making them more suitable for



large-scale experiments. These two techniques will now be described in detail.

### 3.2.1 STEM-DPC with an ADF detector

In this work, STEM-DPC was performed using a conventional ADF detector instead of the segmented or pixelated detectors commonly used for STEM-DPC, as previously described in subsection 2.2.1. The ADF detector indirectly measures the magnetic induction in the sample by mapping the beam deflection, and thus intensity variations, captured by the doughnut-shaped detection area at each scan position. Figure 3.4 illustrates the STEM-DPC setup with an ADF detector. To mimic the signal obtained in regular STEM-DPC, four images were acquired by placing the probe at four positions (N, S, E, W) along the edge of the ADF detector, acquiring one image at a time to obtain a complete dataset. The four images were then combined during data processing into a vector map illustrating magnetization in the structure. Most ADF-STEM-DPC image acquired in this work holds a resolution of  $3072 \times 3072$  and a dwell time of  $8 \mu\text{m}$ , resulting in an approximate acquisition time of about half a minute per probe position.

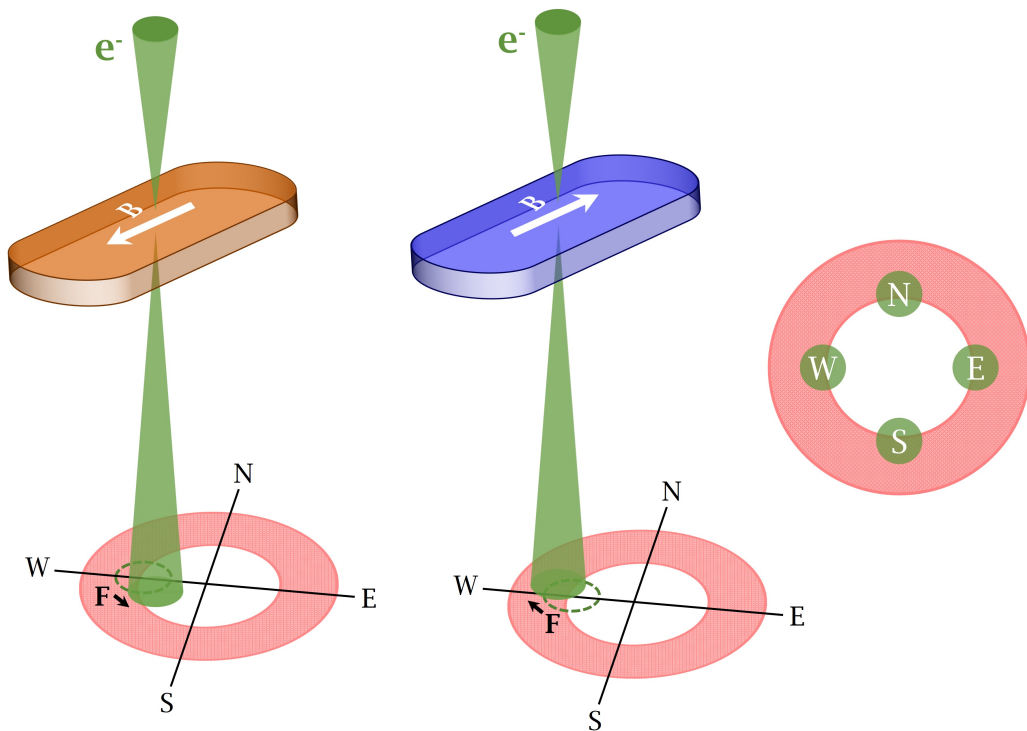


**Figure 3.4: STEM-DPC setup with an ADF detector** | STEM-DPC images were captured by placing the probe placed halfway onto the ADF detector. This arrangement allows for the registration of intensity variations due to deflections in either direction at each scan position. The process is repeated by placing the probe at four opposing positions on the detector to acquire a complete dataset.

STEM-DPC with an ADF detector offers several advantages compared to segmented or pixelated detectors. ADF detectors, which are commonly installed on all conventional TEMs, provide significantly smaller datasets, with each dataset composed of four images requiring less than 200MB of storage space. In contrast, pixelated detectors yield large 4D datasets, usually at least 4GB in size, even at low pixelation. The practicality and accessibility of the ADF-STEM-DPC method make it an advantageous technique for efficient data processing and analysis. In the subsequent section, we will provide a detailed description of the data processing steps, outlining how the acquired images are combined to generate vector plots of the differential phase contrast (DPC) signal.

### 3.2.2 Processing of ADF-STEM-DPC Data

The data processing procedure involved in the extraction of DPC signal from ADF-STEM-DPC signal is broken down in the following steps.

1. **Combining four ADF-STEM-DPC images into a DPC signal:**

- (a) **Pre-processing:** The first step is to remove the de-scan, an unavoidable scanning distortion where the diffraction pattern is shifted based on the probe position's distance from the centre of the scan. This is corrected by first masking out everything but the padding area around the ASI, ensuring that shifts due to the Lorentz force are not affected. Next, a linear intensity plane is created from the unmasked regions and subtracted from the image to level out the intensities. The four images are then aligned to correct for sample drift, using the `stack align` function in `hyperspy`.
- (b) **DPCx and DPCy:** Data from opposing positions on the ADF detector are subtracted to create DPCx and DPCy signals. These signals represent the horizontal and vertical components of electron beam deflection, respectively, and can often be convenient to analyze individually.
- (c) **DPC:** DPCx and DPCy are combined to form a DPC vector plot, which can be colourized to visualize magnetization directions. The magnetization direction is shown in the colour wheel. This and the former step is included in the `calculate_DPC_image` function in `asistem`.

2. **Masking the DPC signal:** Due to factors that might distort the beam in the milled areas, thus affecting the magnetic contrast, it is often convenient to mask the DPC signal for visual clarity.

- (a) **Reconstructed bright field (BF) image:** After accounting for de-scan and sample drift, the four raw images are added together to form a reconstructed BF image, which provides an image of the sample without any magnetic contrast.
- (b) **Edge detection:** Canny edge detection is used to map out the features in the BF image.
- (c) **Corner detection:** Using the `compute_corners` function in `asistem`, the corners are detected from the canny edge map in the previous step.
- (d) **Mask alignment:** The mask is then fitted by matching the corner coordinates and applying the `maximise_pattern_fit` function to find the best fit onto the DPC signal.

The overall flowchart of the data processing steps can be seen in Figure 3.5. The python package `asistem`, developed by Bekkevold [31], is used, and strongly appreciated, with some minor adjustments for processing the datasets. The result of the processing is a detailed and visually informative representation of the DPC signal, showing magnetic domains and the direction of magnetic moments within the sample.

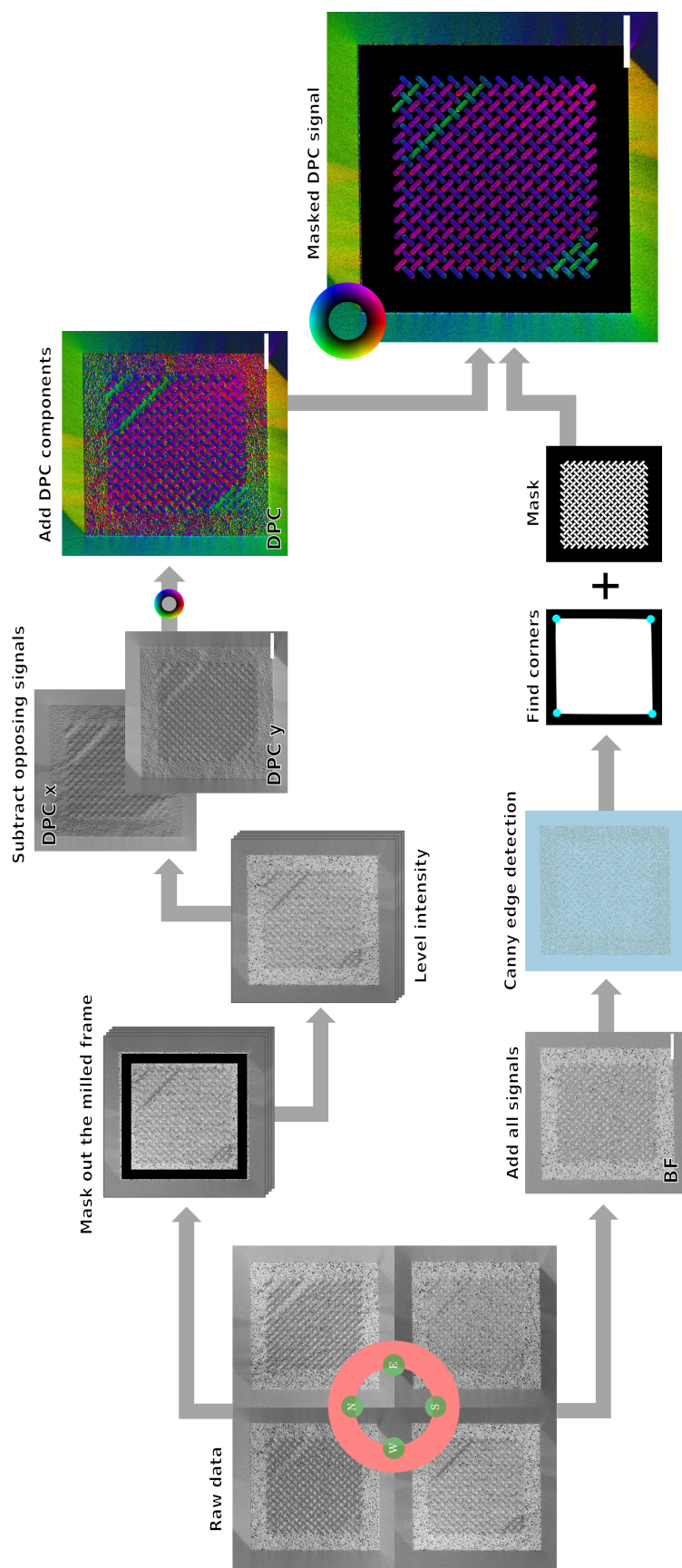


**Figure 3.5: Data processing of ADF-STEM-DPC data** | Flowchart explaining the data processing performed in python, starting from the four raw images to the final, colored and masked vector map.

### 3.2.3 Continuous Tilt STEM-DPC

Continuous tilt STEM-DPC is a technique that expands the capabilities of traditional STEM-DPC by introducing sample tilting. The technique is illustrated in Figure 3.6. This method allows for time-resolved imaging and provides useful insight into magnetic reversal processes. The method works in a similar manner to the ADF-STEM-DPC described in the previous section. However, in continuous tilt STEM-DPC, the probe is placed at one position on the ADF detector, whilst continuously tilting the sample, capturing images of the magnetic states as a function of tilt angle. This technique offers in-situ exploration due to fast acquisition times and provides a new way to explore magnetic reversal and flipping in e.g. ASI structures.

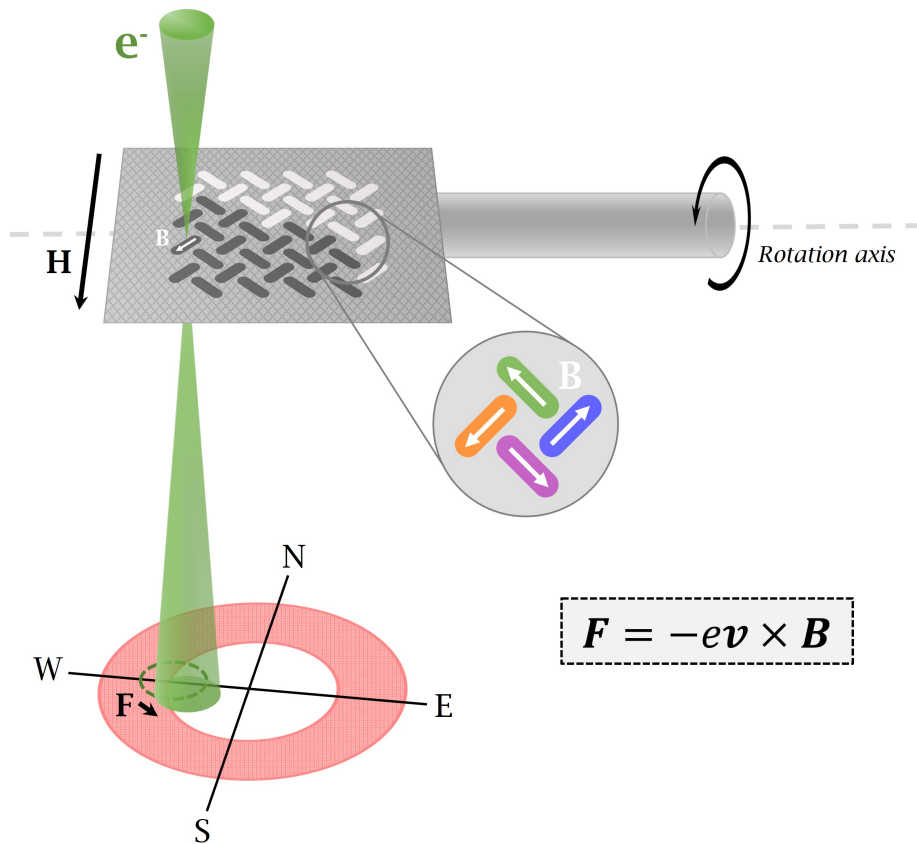


**Figure 3.6: Continuous Tilt STEM-DPC** | Illustration showing how the continuous tilt STEM-DPC method works.  $\mathbf{H}$  is the external magnetic field originating from the objective lens, whilst  $\mathbf{B}$  is the field in and around each magnet due to the inherent magnetization  $\mathbf{M}$ , and the influence of  $\mathbf{H}$ .  $\mathbf{B}$  then causes the electron beam to shift in the direction governed by the Lorentz force,  $\mathbf{F}$ .

It is important to note that the term "time resolution" refers to the ability to capture and observe dynamic processes occurring on short timescales. In the context of STEM-DPC, dynamic imaging refers to capturing images over time to analyze

changes and dynamics in the sample. The term "fast" can also refer to the speed of the instrument or the ability to capture images quickly, allowing for real-time or near-real-time observations of dynamic processes. In the context of this work, the acquisition time was around 3 seconds per  $768 \times 768$  image, which is good for fast data acquisition, but does not provide us with insight into time-resolved dynamics within each magnet or what happens in the time between stable and metastable states.

### Considerations Regarding Probe Placement and Detector Geometry

The placement of the electron probe on the ADF detector is important to consider when applying the continuous tilt STEM-DPC method. Because of the geometry of the doughnut-shaped ADF detector and our very geometrical material system, the probe placement will directly affect magnetic contrast in the acquired images. To obtain as much information as possible in one image, the probe should therefore be placed on an edge where deflection results in as many intensity variations as possible. An illustrative example showing the significance of probe placement when comparing the square and pinwheel lattice is presented in Figure 3.7. When capturing data of the pinwheel lattice (see Table 3.1), it was found that the south-west (SW) probe position (Figure 3.7d) yielded the best results, exhibiting three intensity variations. The opposite applied for the square lattice, showing that the west (W) probe position (Figure 3.7a) maximized magnetic contrast, also resulting in three intensity variations. It is worth noting that the probe position can of course be rotated by multiples of  $90^\circ$  because of the symmetry of the ASI arrays. For the STEM-DPC method described in subsection 3.2.1, four images are combined so the position does not matter unless you are only analysing the DPCx and DPCy components.

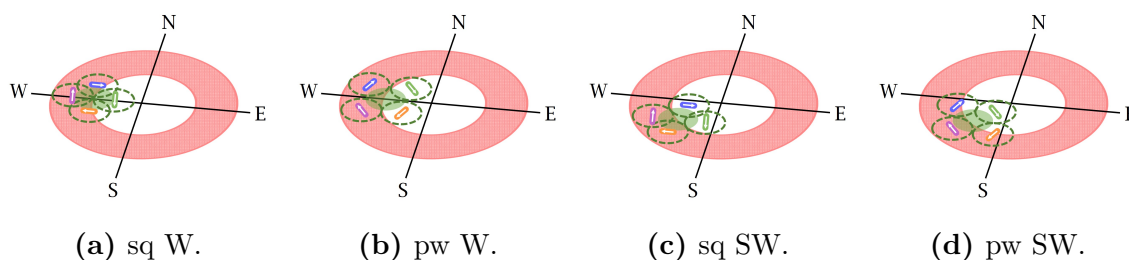


**Figure 3.7: Probe position on the ADF detector** | Probe position matters when capturing magnetic contrast. Imaging a square ASI with the probe placed at (a) W position or (c) SW position should theoretically result in three versus two shades of grey, respectively. The opposite applies for the pinwheel ASI if rotation is kept constant, where (b) W is less favorable than (d)SW with two versus three intensity variations captured by the ADF detector. Note that the stapled circles here represent the deflected beam.

---

## Chapter 4

# Results & Discussion I

## Sample Fabrication

“The biggest room in the world is the room for improvement.”

---

Helmut Schmidt

This chapter serves as the first of two chapters comprising the Results & Discussion section. In this chapter, we delve into our journey from initially being limited to milling ASIs with larger M-sized ( $600\text{nm}\times 200\text{nm}$ ) islands to the successful FIB milling of ASIs with smaller XS-sized ( $225\text{nm}\times 75\text{nm}$ ) islands. Additionally, we explore the milling parameters and strategies used to minimize surface roughness and hole formation, as well as channelling effects.

### 4.1 The Path Towards XS-Sized ASI Islands

Throughout the course of this work, it has become increasingly apparent that achieving high-quality FIB milling is arguably the most critical, albeit tedious, step in the procedure outlined in Figure 3.1. That is simply because you cannot observe ASI behaviour if you have not actually been able to make a structure that behaves in such ways. In the ASI community, studies often focus on arrays of stadium-shaped<sup>1</sup> magnetic islands with dimensions around  $220\text{nm}\times 80\text{nm}\times 10\text{-}30\text{nm}$  [1, 4]. When each island in the structure is that small, they can be assumed to be single domains and thus behave like single magnetic moments, or macro spins. Consequently, the structure falls under the category of ASI and all that entails. However, manufacturing this typical size of ASI islands requires exceptionally high pattern fidelity, i.e. the quality of the milled pattern relative to the input mask. In the early stages of this research, achieving such precise control over the patterning process proved challenging due to a number of reasons.

---

<sup>1</sup>A rectangle with rounded corners, similar to that of a football stadium

The main advantage, but also a disadvantage, of utilizing FIB for sample fabrication is the wide range of parameters which significantly influences the final result. These parameters can be tuned, which allows for enhanced control of the quality of the fabricated structures. However, this flexibility also means that finding the optimal parameter settings can be time-consuming. Trial and error are often necessary to achieve the desired results, especially when working with new materials or complex structures. In the following, it will be demonstrated that tuning of parameters can be done either directly in the software, or indirectly via choice of mask design, milling strategy and quality of ion beam alignment.

### 4.1.1 Optimizing Milling Parameters

To explore the various parameters set directly in the FIB software,  $5\mu\text{m}\times 5\mu\text{m}$  squares were milled, varying one parameter at a time. The parameters examined were scan direction (bottom to top, top to bottom, left to right, right to left), dwell time (100ns, 250ns, 500ns, 1000ns), amount of passes (100, 500, 1000, 10000, 20000) and beam current (9.7pA, 27pA). However, no particular differences in surface roughness were observed, nor any other indications of improved milling quality. For the rest of the discussion, the software parameters used were scan direction left to right, 500ns dwell time and 20000 passes. When milling intricate patterns, the number of passes did seem to show some improvement, reducing surface roughness and hole formation. This is in line with theory, which states that multiple pattern repeats will result in a slower, more uniform and controlled milling procedure than a single repeated pattern because re-deposited material is removed for each scan. However, as a high number of passes reduces sputter yield, the beam current was set to 27pA to ensure maximum milling efficiency. Although, it could be useful to conduct an organized experiment by varying these parameters for bitmaps and not just for simple squares. The ion beam energy was set to 30kV after some experimenting with 16kV, in order to obtain the highest possible lateral resolution together with a high sputter yield [34, 35]. The ion dose used was  $20000\text{ nA/nm}^3$ , which is considered suitable for magnetic thin films of 20-30nm [34]. Even though tuning most of these parameters did not prove significant changes, a sudden improvement in milling quality happened at a point. This was most likely due to a combination of several factors, one being the choice of mask design and beam overlap.

### 4.1.2 Mask Design: Bitmap Resolution and Beam Overlap

The work of Urbànek et. al. [34] has been a valuable reference, inspiring changes in the milling procedure and providing answers to why certain changes showed better results than others. Even though SiN was used in this project, and not pure Si substrate, the similarities between the two experiments are evident. Some of the factors enlightened in their work are probe size and beam overlap, incidence milling angle, ion dose and dwell time. These factors, to varying degrees, have been found to strongly influence surface roughness, hole formation, channelling effects and re-deposition rate.



The subsequent discussion follows a thorough analysis of how these factors can have improved the milling quality and resolved the issues outlined in Appendix A.

Appendix A shows that the FIB software is sensitive to large pattern files, such as highly pixelated bitmaps, at least above  $2048 \times 2048$  pixels. The original bitmaps showed in Table 3.1 are composed of  $4096 \times 4096$  pixels with a pixel resolution of 2.5nm if the area milled is  $10.24 \mu\text{m} \times 10.24 \mu\text{m}$ . Therefore, to ensure that the software does not crash, the bitmaps were resized to  $512 \times 512$ , leading to a resolution of 20nm/pixel. This is illustrated in Figure 4.1. The blurring that can be observed in the right-most image, can be due to the `EdgeSmooth` parameter that is set to 8 in Mumax<sup>3</sup>, an effect of the resizing, or a combination of the two. It remains unknown if the FIB takes blurred edges into account when milling or not. We will assume that it does not.

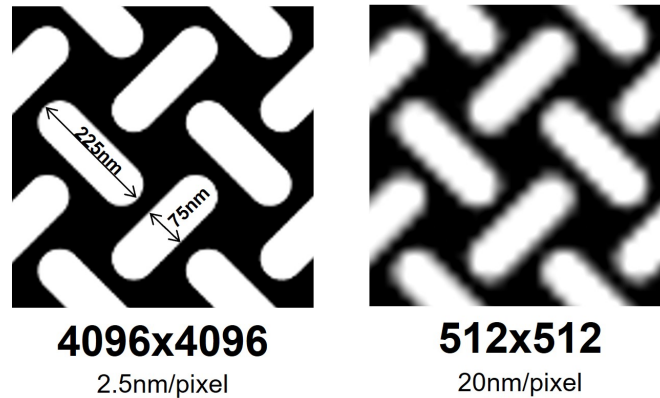


**Figure 4.1: Bitmap resolution** | The left-most image shows the original  $4096 \times 4096$  pixelated bitmap of an XS pwASI created in Mumax<sup>3</sup>. The right-most image is the  $512 \times 512$  resized version.

Not surprisingly, the resolution and pattern fidelity of a milled structure is directly influenced by bitmap resolution (area milled/amount of pixels). A less obvious factor is that bitmap resolution, together with probe size, dictates probe overlap. Probe overlap refers to the amount of ion probe overlapping from one scan position (pixel) to the next, and can normally be tuned directly in the FIB software. In bitmap mode, this can most easily be controlled by tuning bitmap resolution through pixelation or by adjusting the size of the bitmap milled. Figure 4.2 illustrates an example of a scaled-up bitmap whilst keeping a constant probe size of 30nm. This results in four different bitmap resolutions of 10, 20, 30 and 40nm/pixel, from left to right respectively. It is not entirely thought out to expect that e.g. the 10nm/pixel scenario could lead to hole formation and the 40nm/pixel scenario in an unevenly milled surface, as the two scenarios show severe overlap and no overlap, respectively.

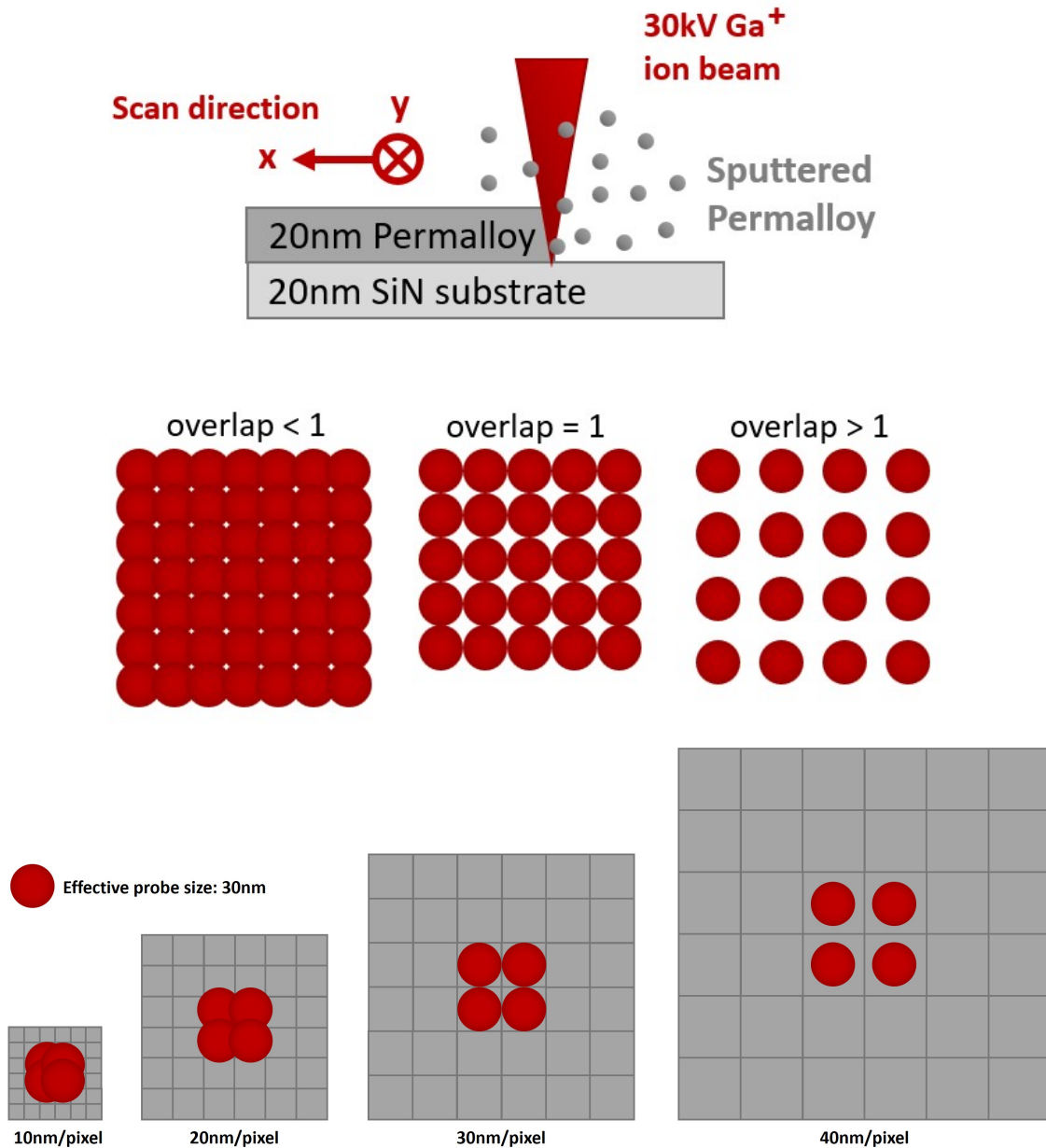


**Figure 4.2: Resolution and size of bitmap dictate ion beam overlap** | The size of the probe, overlap and angle of incidence milling angle can all be adjusted when milling in FIB. Here, the ion beam is shown milling normal to the specimen with an ion beam voltage of 30kV. Illustrated below are four scenarios with a thought probe size of 30nm, showing that when the size or resolution of a bitmap changes, this strongly influences probe overlap. It is therefore crucial to control bitmap size and resolution to avoid surface roughness and hole formation when using the patterning function in FIB. Figure inspired by [34].

Urbanèk et. al. reports that beam overlap holds a significant influence over factors such as hole formation and surface roughness. Their work shows that an ideal overlap is around 30%, corresponding to an overlap value of 0.7. This value ensures maximum smoothing of the Gaussian-shaped intensity distributions of each probe spot, which is essential to obtain uniform milling [34]. If compared to Figure 4.2, we see that this value corresponds to approximately that observed in the second scenario from the left (20nm/pixel), with an overlap of 0.66. In our work, we have, unless stated otherwise, used a bitmap resolution of 20nm per pixel (512×512 pixels distributed across an area of 10.24µm×10.24 µm). However, because the effective probe size remains unknown, an exact value of the probe overlap can not be estimated. As an attempt to estimate beam overlap, and thus probe size, we will now evaluate some geometries milled when varying bitmap resolution.

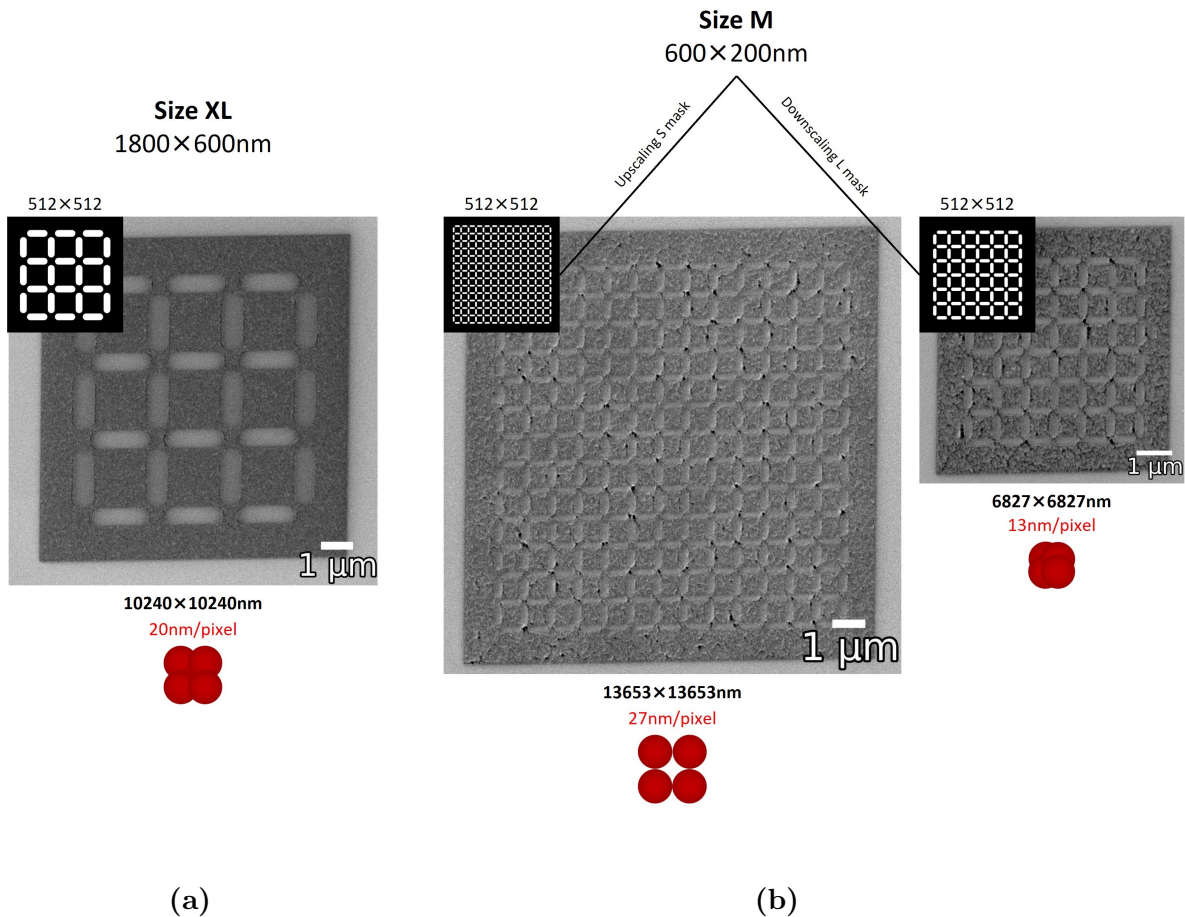


**Figure 4.3: Varying size of milled area** | Three FIB images of consecutively milled square arrays of (a) XL-sized islands and (b) M-sized islands using two different bitmaps, one downscaled from L, and one upscaled from S. The probe size was kept constant, resulting in differing beam overlap.

In Figure 4.3, three distinct structures are presented, all milled consecutively using the same parameters, ensuring a consistent, yet unknown, probe size. Each structure was milled with a  $512 \times 512$  bitmap, but bitmap geometry (XL, S and L) and area milled was varied. In Figure 4.3a, the XL-mask is milled on an area measuring  $10.24 \mu\text{m} \times 10.24 \mu\text{m}$ , which is the standard area milled in this project. As mentioned, this yields a bitmap resolution of  $20\text{nm}/\text{pixel}$ . In Figure 4.3b, an S-mask was upscaled by a factor of  $\frac{1}{3}$ , resulting in each element measuring  $600\text{nm} \times 200\text{nm}$  instead of  $450\text{nm} \times 150\text{nm}$ , and a bitmap resolution of  $27\text{nm}/\text{pixel}$ . Conversely, the L-mask was downscaled by a factor of  $\frac{1}{3}$  from  $900\text{nm} \times 300\text{nm}$  to  $600\text{nm} \times 200\text{nm}$ , resulting in a bitmap resolution of  $13\text{nm}/\text{pixel}$ . This resizing of masks was necessary as a separate M-sized mask had not yet been made at this point.

Upon examining the M-sized elements in Figure 4.3b, we observe an increase in surface roughness and hole formation compared to the XL-sized structure in Figure 4.3a. Sources state that the milling rate is faster along edges, potentially explaining the presence of holes between the M-sized islands [34, 36]. However, this does not explain the enhanced surface roughness. Assuming that the XL-sized structures were milled with the ideal overlap of 0.7, this would correspond to an effective probe size of about  $30\text{nm}$ . Anyhow, referring to the argument presented in Figure 4.2, it is possible that this slight variation in pattern size leads to different beam overlap, and consequently sub-optimal surface roughness. Another factor to consider is pattern density. Higher pattern density often yields more efficient material removal and reduces the likelihood of holes and incomplete milling. The pattern density, defined as the non-milled area divided by the total area, is approximately 30% for the square geometries and 50-60% for pinwheel geometries. The pattern density in Figure 4.3 from left to right is approximately 30%, 23% and 25%. Whether a higher pattern density can have such a high impact on surface roughness remains uncertain, and it is highly likely that the observed effects are a combination of multiple factors.

### 4.1.3 Probe Size: Milling Efficiency and Precision

Achieving uniform and precise material removal is crucial when fabricating intricate ASI bitmaps. This can be ensured through careful tuning of the probe size, achieved by selecting the appropriate aperture and ensuring proper beam alignment. In this work, the expected probe size was assumed to be around  $15\text{nm}$  based on previous experience and the findings of Urbànek et. al. [34]. However, the effective probe size in this experiment was estimated to be around  $30\text{nm}$ , as mentioned in the previous section. This larger effective probe size can be attributed to factors such as drift, charging, and the interaction volume of  $\text{Ga}^+$  ions in the material. It is therefore important to take these effects into consideration when experimenting with parameters and mask design. Additionally, it is important to ensure proper beam alignment to maintain precision in FIB systems. This involves precise alignment of the stage and beam, focusing the structures accurately on the ion beam, and minimizing beam astigmatism. A good beam alignment facilitates a circular and small ion probe, resulting in precise milling paths. The beam must often be re-aligned from time to time to ensure that it is

still in focus, especially when moving across the sample due to height differences. Additionally, instrument instabilities or external factors like rush hours in the lab or nearby train vibrations may introduce instabilities to the ion beam. There is even a possibility of slight movement from the operator's chair affecting the alignment. To mitigate these effects, the FIB instrument is typically placed on a separate floor block to minimize unwanted vibrations.

In addition to probe size, the ion beam current also plays a significant role, especially in terms of material removal rate. Too low a current results in a slower material removal rate and the risk of incomplete milling. Conversely, if the current is too high, it can result in too fast material removal, potential structural damage, and the formation of holes before the milling process is complete. During the milling procedure at 30kV, both a smaller (9.7pA) and larger (27pA) apertures were tested. Consistent with the findings of Urbánek et al., it was determined that both apertures could be utilized. However, the larger aperture achieved a milling time of approximately one minute, while the smaller aperture required around five times longer to achieve similar results. Additionally, we observed that the milling rate became too slow for the smaller aperture, often resulting in insufficient material removal, requiring the milling process to be stopped. Given that there was no significant increase in surface roughness observed with 27pA aperture compared to the 9.7pA aperture, 27pA was selected for more efficient milling. Furthermore, in the DualFIB system at NanoLab, two 27pA apertures were available, and it was observed that one of them produced slightly better results than the other. This difference could be attributed to factors such as mechanical wear over time or inherent variations between the apertures.

#### 4.1.4 Milling Strategy: Channelling Reduces Sputtering Yield

As mentioned earlier and in Appendix A, issues were encountered when milling small features such as S and XS islands. The milling was found to be extremely uneven as shown in Figure A.1b, leading to holes after only a few seconds of milling, even at low currents. However, after some trial and error, ASIs with both S- and XS-sized islands were fabricated with good precision. Coincidental or not, this occurred at the same time as the ion beam was tilted  $10^\circ$  off the normal incidence angle and is therefore believed to be the main cause of this improvement. Efficient milling in FIB is associated with cascade events, i.e. a series of collisions that take place when an ion interacts with the target material. This is also one of the main reasons for the lateral spread of ions, resulting in a larger effective beam and milling volume. During this cascade, each incident ion transfers its kinetic energy to target atoms through elastic collisions, causing atomic displacements. These displaced atoms can then further collide with neighbouring atoms, leading to a cascade of atomic collisions and displacements within the material. However, when an ion does not transfer its kinetic energy to the material in this way, they are left with a lot of energy when eventually colliding with Py thin film or even the SiN substrate, maybe causing unwanted hole formation. This has not been proven but could be a possible explanation as to why holes are so easily created when milling at the normal incidence ion beam angle [36]. Whenever a charged particle,

whether that be an electron or an ion, interacts with a crystalline material, there is a probability of channelling. Channelling is a well-known effect when working with crystalline materials, which occurs when charged particles are aligned with the crystal lattice planes in the material. Channelling is most prominent for low-index directions and close-packed crystal structures with high atomic densities [36]. This can become a problem when milling nanocrystalline Permalloy. Channelling is most often not desired in FIB milling, because ions will traverse through the material with minimal interaction, reducing the milling efficiency dramatically [37, 38]. Non-channelled ions, on the other hand, will yield a higher sputtering yield of the material, strongly influencing the final results [34, 39]. Considering the nanocrystalline structure of Permalloy, channelling is expected to occur independently of the incidence milling angle. Because SiN is amorphous, and has a lower packing density than Permalloy, the substrate is therefore expected to yield less channelling than in the Permalloy itself, working as a barrier for high-energy channeled ions, which may result in hole formation.

Another contributor to hole formation could be the choice of milling strategy. Several advantages have been reported when using serpentine as opposed to raster during FIB milling [33]. Serpentine can help mitigate channelling effects and reduce the formation of holes compared to raster scanning. Serpentine also allows for tight spacing between milling paths and reduces re-deposition, which can result in higher pattern fidelity and finer feature resolution. It has been proven that more advanced scanning paths can result in less surface roughness and could be a consideration for future work if provided a FIB that has the possibility to do so [33].

## 4.2 Summary and Future Directions: Fabrication

In summary, the use of  $10.24\mu\text{m}\times 10.24\mu\text{m}$  sized bitmaps with  $512\times 512$  pixels was shown to be optimal with the milling parameters presented in subsection 4.1.1. It is important to consider that even though smaller ion beam currents can result in finer patterns, prolonged milling times can also introduce irregularities such as increased re-deposition rates, resulting in more grain growth. It is therefore recommended to continue using a  $512\times 512$  bitmap with a 27pA aperture for efficient milling, minimized re-deposition and maximized sputter yield. High milling efficiency is also crucial for studying larger ASI systems. With small adjustments to the presented protocol, it is possible to extend the fabrication of ASI structures to more than 10000 islands, which is more than a four-time doubling of the number of islands in the XS-sized pwASIs milled in this work. All in all, FIB milling is shown to provide advantages when tailoring the process for each material and geometry, despite its complexities. Other fabrication methods like EBL, have drawbacks in terms of time consumption and multi-step procedures as well as challenges in STEM-DPC due to charging and beam distortions. Overcoming these challenges, especially charging and beam distortion would be necessary for it to work effectively for STEM-DPC. Because of this, FIB remains the preferred tool for fast prototyping of ASI designs for characterisation with STEM-DPC, whereas EBL should be employed for large-scale production of high-quality ASIs.

## Chapter 5

# Results & Discussion II

## Characterization

This chapter presents the primary findings of this study, focusing on the two Lorentz TEM characterization methods applied, namely STEM-DPC with an ADF detector and continuous tilt STEM-DPC. First, we address some important considerations that should be taken into account during the general LMSTEM alignment procedure. Then we dive into the significance of channeling effects from FIB, resulting in enhanced diffraction contrast in TEM. Lastly, we present and discuss the findings when studying the square and pinwheel lattice, linking them to the magnetism and STEM-DPC theory previously presented. Throughout the following section, it should be noted that the two STEM-DPC techniques are intended to complement each other. Therefore, it is advisable to utilize both methods together to conduct a thorough and efficient analysis, especially when studying magnetic reversal in ASI.

### 5.1 LMSTEM Alignment Procedure

Specimen quality and pattern fidelity are critical factors that impact spatial resolution, as emphasized in the previous chapter. Once these factors are ensured, the stage is set for exploration of structures using STEM-DPC. The STEM data presented in this study were acquired in low magnification mode, also known as OL-off or wide-field mode. In this mode, the objective lens is intentionally turned off to reduce the magnification, but can also be used in magnetic imaging to create a near-field free region around the specimen. Throughout this study, several improvements have been made to the LMSTEM alignment procedure. Initially, the smallest magnetic islands we were able to observe were around  $600\text{nm} \times 200\text{nm}$  (size M). The limiting factors could be sample fabrication, various effects contributing to distortion of the electron beam during STEM-DPC acquisition, the specific TEM instrument used and the operator's experience.



### 5.1.1 Using a Milled Circle as a Compass and Alignment Tool

Regardless of the detector used, precise calibration of directions is crucial in STEM-DPC to ensure an accurate representation of the vector plots. This is particularly important in our study, where we tilt structures, such as sqASI and pwASI, along the diagonal and vertical axis, respectively. This may result in some confusion during data processing if caution has not been taken during data acquisition. When acquiring data, it is important to take note of sample rotation, scan rotation and the position of the probe on the ADF detector. To validate the directions, milling a circle, as depicted in Figure 5.1, has proven to come in handy due to multiple reasons. The DPC signal indicates that the induction vectors inside the vortex follow a curved path, always pointing parallel to the edge circumference of the milled circle. This is the expected magnetic behaviour of a magnetic vortex [40], and can therefore be used to calibrate the magnetic directions in our structures. The chirality of the vortex could also be inverted, meaning the spins are aligned counterclockwise, opposite of that in Figure 5.1. The colour wheel represents the magnitude and direction of magnetic induction vectors and is representative of all ADF-STEM-DPC data shown in this work if not specified otherwise.

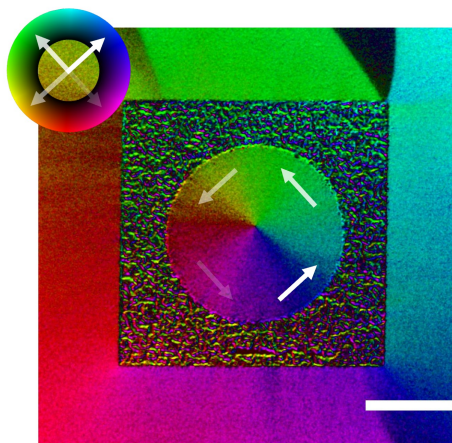


**Figure 5.1: Calibration circle** | Milled circle used for alignment and color wheel calibration during data processing. Scale bar is 2  $\mu\text{m}$

Apart from its usefulness in calibration, the circle also serves as a valuable tool for aberration correction. When the OL is turned off in LMSTEM, it leads to an increase in aberrations such as astigmatism and coma. This is because the condenser mini lens takes over as the probe-forming lens in LMSTEM when the OL upper pole piece is turned off. The condenser mini lens is weaker compared to the OL, resulting in more pronounced aberrations in LMSTEM. In conventional STEM alignment, astigmatism can be corrected using the Ronchigram, but in low mag mode, this becomes significantly more difficult. Instead, the calibration circle can be utilized for this task by simply fitting the circle to one of the larger condenser apertures, elegantly eliminating most signs of astigmatism. This approach assumes a fully circular condenser aperture and a calibration circle milled normal to the incidence angle. It is also worth



mentioning that even though the Ronchigram in LMSTEM is not great for aberration correction, it is useful as a shortcut to obtaining perfect focus, as the Ronchigram is located at the in-focus point. The calibration circle can also be utilized to correct for any mis-tilt of the specimen, which refers to small deviations from perfect, normal alignment to the magnetic field generated by the OL. By tilting, one can navigate the vortex to the middle of the circle, almost like a game of labyrinth where the rolling ball is the vortex, compensating for the mis-tilt and ensuring accurate alignment of the specimen. This was done in an attempt to reach the ground state of sqASI by obtaining a close-to-uniform field across the specimen.

### 5.1.2 An Attempt to Reach the Ground State of sqASI

Unlike any pattern of randomly assembled magnets, ASIs behave in a collective manner due to interactions through local dipole-dipole coupling. These interactions are the very reason for the phenomena that give any natural or artificial spin ice its unique properties, namely magnetic frustration (see subsection 2.1.6). Because spin ices show rich dynamics, the systems often have degenerate ground states, meaning there are multiple low-energy states that can be formed, as explained in subsection 2.1.7. The ground states of ASIs are governed by the ice rule, which states that in a lattice site of the spin ice, two spins point in and two spins point out (see Figure 2.6). In a sqASI or pwASI, the lowest energy state is type 1 and type 2 configurations, respectively.

One possible explanation for the challenges in observing low-energy states is that even a slight tilt of the specimen can cause the system to favour a different configuration due to the presence of the external magnetic field from the OL. To correct for any mis-tilt, we can utilize the calibration circle. This can be done by tilting the sample holder to balance the vortex at the centre of the calibration circle. This provides a rough estimate of zero tilt, although hysteresis must be taken into account. Another approach involves moving to an empty window in TEM mode, defocusing to observe domain walls (Fresnel imaging), and gently tilting the sample holder to "lock" a domain wall across the window. These two techniques for finding the zero tilt point were employed in an early-stage experiment, with the results shown in Figure 5.2b, while the starting point is depicted in Figure 5.2a. Even though the ground state was out of reach for this experiment, we did successfully manage to align our specimen so that the field from the OL seems more normal to the specimen. However, due to hysteresis and limitations of our rotation holder with a single tilt angle, achieving precise alignment proved challenging. The results after tilt show a more similar state as the low-energy state shown in Figure 2.6 than what was observed before tilting. Additionally, another approach was explored by briefly activating the current in the objective lens to enhance the magnetic field in the z-direction and then switching it off. The goal was to reset the structure from any previous configuration and relax it into its most energetically favourable configuration. This particular method did not yield any significant results. Ground states of ASI systems can be reached through thermal activation and relaxation [13]. In TEM, this can be done by heating the specimen utilizing a heating holder. For this to work, the structures should be less than 10nm thin to be thermally

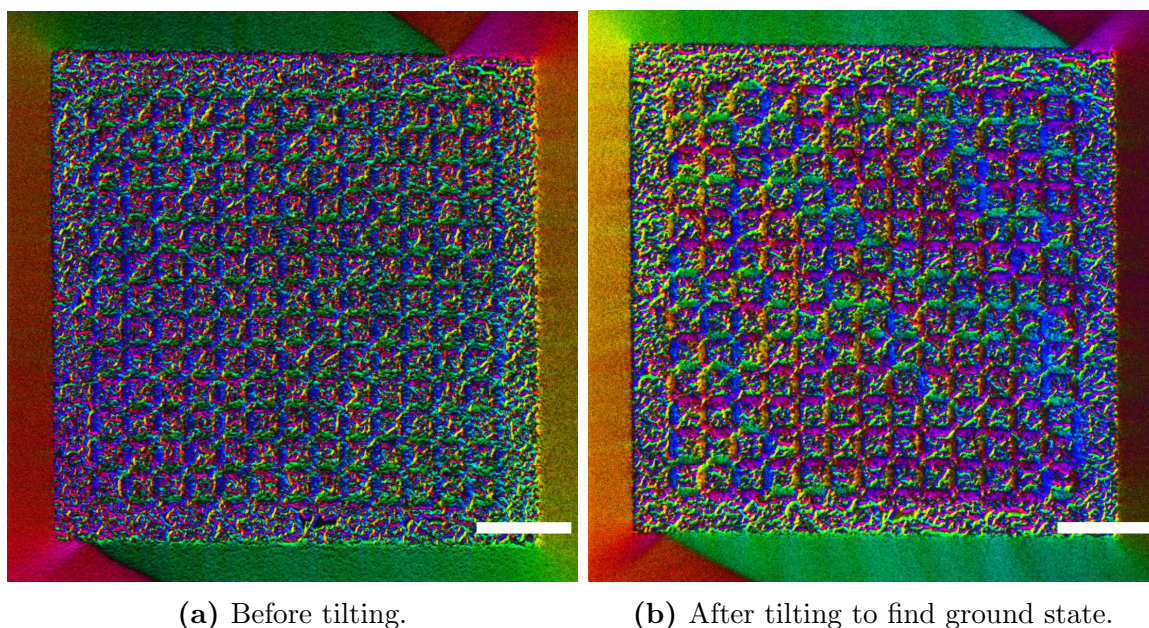


**Figure 5.2: Tilting to groundstate** | Before and after specimen tilt in an attempt to reach ground state. The data set was acquired before the FIB procedure was refined resulting in strong contrast from the milled areas. Scalebar is 2  $\mu\text{m}$ .

active. To limit the scope of the project, and our structures being 20nm thick, no temperature experiments were performed. The mention of temperature experiments is provided only as a suggestion for future considerations.

### 5.1.3 Correction of Coma

In addition to astigmatism, another significant challenge in achieving high-resolution imaging was the presence of comatic aberrations, also called coma. Coma is caused by off-axis alignment, resulting in distorted or elongated, comet-like effects, and is especially noticeable when moving in and out of the focus point. This aberration results in a degradation of image quality characterized by blurring or asymmetry. In LMSTEM mode, where the objective lens is turned off, coma is observed to be severely more pronounced. Coma is corrected by adjusting the beam deflectors, or condenser alignment coils, to tilt the beam onto the coma-free axis. This should be done in LMSTEM mode, with a large condenser aperture inserted. When moving in and out of focus, there should be no shift of the structure at the through-focus point, and the structure should look completely *flat* to the eye. After the best possible beam tilt correction, the smallest condenser lens aperture is then placed around the through-focus centre, and the beam is shifted with the projector lens deflectors onto the edge of the ADF detector for subsequent STEM-DPC imaging. Coma correction requires periodic checks to maintain accuracy, and the same applies to astigmatism. Because coma and astigmatism alignments affect each other, and alignment can drift

and become worse over time, it is important to iteratively adjust and monitor these aberrations to ensure optimal imaging quality at all times.

### 5.1.4 Magnetic Contrast

After refining the LMSTEM alignment procedure and making severe improvements to the milling process, it was realized that it is indeed possible to observe magnetic islands all the way down to sizes  $225 \times 75 \text{nm}$ . This was also the initial goal, as it compares to the sizes typically used in the ASI community [1, 4]. To further improve the imaging method, some experimenting to enhance magnetic contrast was done. Magnetic contrast refers to the sensitivity of electron beam movement, i.e. the detector's ability to capture small deflections of the electron beam. Although the magnetic contrast was quite good from the start, it was even further improved by adjusting the projector lens to its maximum setting. This effectively increased the camera length, allowing for more precise measurements of even smaller variations in beam shift. Additionally, it was noted that arrays of islands are generally easier to observe compared to individual islands milled by themselves. This can be attributed to interactions between the magnetic islands, amplifying their magnetization and resulting in more prominent beam deflection. Another way to enhance magnetic contrast is by increasing the current through the OL, thereby enhancing the external magnetic field applied to the specimen. Previous studies have reported that a slight increase in OL current leads to enhanced magnetic contrast [31]. Tuning of the OL, as well as other lenses, was therefore explored via free lens control (FLC).

#### Enhancing Magnetic Contrast: Varying Objective Lens Current

While we refer to this technique as "OL off", it is important to note that a small residual field of approximately  $35 \text{mT}$  perpendicular to the sample still remains (see the experiment in Figure D.1). To eliminate this residual field completely, an opposing current can be applied to the objective lens, although this is not yet possible at our microscope. Even though this residual field makes it difficult to for example observe low-energy states, it has proven advantageous for the purposes of this work. The ASI structures showed desired sensitivity to the field strengths obtained when tilting the specimen in the available tilt ranges ( $\pm 30^\circ$ ). What is meant by this, is that with the residual field of  $35 \text{mT}$  from the OL, we could access many stable states of the ASI structures, with full magnetization around maximum tilt. It is also possible to enhance this magnetic field by changing the current through the OL. This was experimented with in Figure 5.3, changing the OL values in FLC to 128, 256 and 512, corresponding to approximately  $45 \text{mT}$ ,  $55 \text{mT}$  and  $70 \text{mT}$  (see Figure D.2). For  $55 \text{mT}$ , it was observed "bleeding" magnetic contrast from the islands, much like the effect seen when applying a strong Gaussian filter to this data. A darker, but more vibrant contrast was also observed, especially in the milled areas, probably due to the aberrations not being properly corrected for when changing OL strength. For  $70 \text{mT}$  in Figure 5.3c, the magnetic information is completely gone. An explanation could be that the magnetism within the islands is no longer aligned in-plane. A more likely



explanation is the same as for what observed in Figure 5.3b, that the alignment is off. This can be argued for because the effect is not only enhanced for the magnetic contrast within the islands but also for the "magnetic" contrast from the surrounding milled areas. This will be discussed later on. It remains unknown if this approach could in fact work with some re-alignment. Nevertheless, it was concluded that the residual field of approximately 35mT was sufficient and a good value for the purpose of this study.

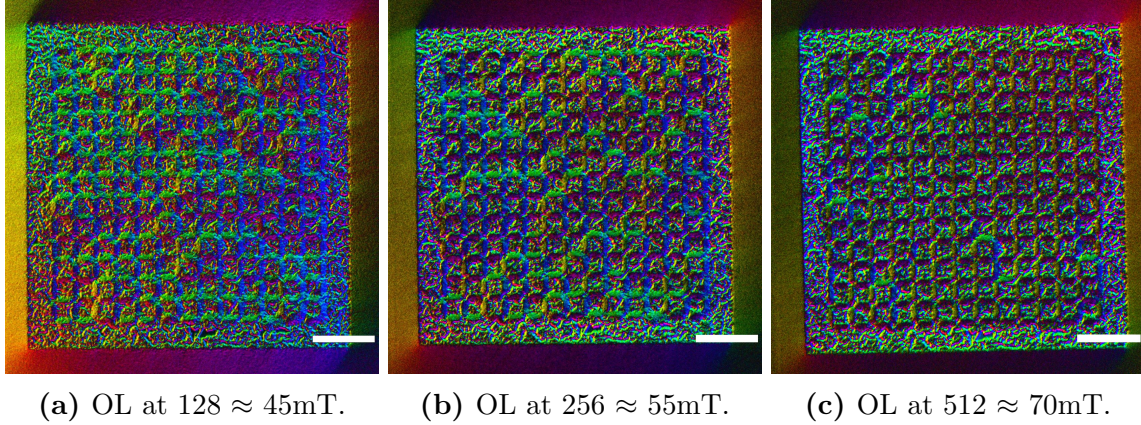


**Figure 5.3: Magnetic contrast and OL strength** | Results when varying the OL current, and thus the effective, external magnetic field, from a value of around 45mT to 75mT. See Appendix D for magnetic field experiments. Scale bars are 2  $\mu$ m.

### Maximizing Magnetic Contrast: Probe Position and Detector Geometry

A third way to enhance magnetic contrast is by considering probe placement on the ADF detector. Due to the ADF detector geometry, the probe placement on the detector in regard to the relevant structure is extremely important to consider. An example of varying magnetic contrast based on sample geometry is shown in Figure 3.7. In Figure 3.7a and Figure 3.7c, the square lattice is illustrated with the probe placed halfway onto the detector in the west (W) and southwest (SW) positions, respectively. Because of the sample's orientation relative to the detector, these two probe placements will result in different intensities. When the probe is placed in W (Figure 3.7a), and if the ASI islands are assumed to have four separate magnetization directions, three shades of grey can be accessed. Islands with magnetic field  $\mathbf{B}$  aligned in the S-direction will show light contrast, whereas those with  $\mathbf{B}$  aligned in N-direction will show dark contrast. The two islands aligned parallel to W and E will both show similar contrast, somewhere between light and dark. If the same logic is applied to the scenario in Figure 3.7c, only two intensity variations will show, and therefore it is not possible to differentiate the four directions that easily. The same logic applies to the pinwheel structure in Figure 3.7b and Figure 3.7d. Therefore, to maximize magnetic contrast, the probe placement for sqASI should be one of the cardinal directions N, S, E or W, whereas for pwASI the mid-way cardinal directions should be used

(NW, SW, NE, SE). This of course depends on scan alignment and specimen rotation (see Table 3.1) and is most relevant to take into consideration when obtaining tilted STEM-DPC data, where only one probe position defines the final outcome. However, the choice of probe position will also affect the DPC<sub>x</sub> and DPC<sub>y</sub> components in regular ADF-STEM-DPC data, although the complete DPC signal will remain unchanged.

### **False Magnetic Contrast: Structural Contrast from Milled Areas**

The ability to observe smaller magnetic islands is primarily limited by the quality of the milling process and the structural contrast arising from the milled areas, as shown in Figure 5.2 and Figure 5.3. Although improvements have been made in the final results soon presented, this problem continues to impose limitations on the fabrication and imaging methods employed in this work. The contrast can be attributed to the rough surface due to the milling process, which still involves some degree of preferential milling and re-deposition. This contrast does not appear to be of magnetic origin, as discussed in section 5.2, and can effectively be masked out.

In chapter 4, EBL was briefly compared with FIB patterning. Due to the presence of height differences and charging when using EBL, FIB was chosen as the preferred STEM sample preparation technique. Using EBL can result in a distorted and elongated beam when scanning across height differences as observed by Bekkevold [31], causing disturbances when mapping magnetic contrast. In ADF-STEM-DPC, simultaneous access to both the image plane and the back focal plane, as available with a direct electron detector (DED), is not possible. Consequently, we are unable to analyze whether the magnetic contrast observed in the milled areas is solely due to distortions of the electron probe or if other factors contribute to it. However, it is highly likely that similar distortions of the electron probe play a significant role when scanning across the rough surfaces of the FIB milled areas. Additionally, other factors like diffraction contrast may also contribute to the observed disturbances in magnetic contrast and will be discussed in the following section.

## **5.2 Diffraction Effects**

In the previous chapter and subsection 4.1.4, we discussed the immense improvement of milling precision and pattern fidelity achieved by tilting the incidence ion beam angle. However, there was another significant improvement that emerged as a side effect of this approach.

One significant challenge encountered in this study was the presence of diffraction contrast originating from the milled areas between the magnetic islands. This contrast is believed to be caused by preferential milling of certain grain orientations due to channelling effects in FIB. Figure 5.4 compares reconstructed BF images of two square lattices milled at the normal incidence angle (Figure 5.4a) and 10° off the normal incidence angle (Figure 5.4b). These structures were milled approximately one month apart in the project. Both BF images were reconstructed by adding the four ADF-STEM-DPC images taken at 0° tilt in LMSTEM. Figure 5.4a exhibits significantly

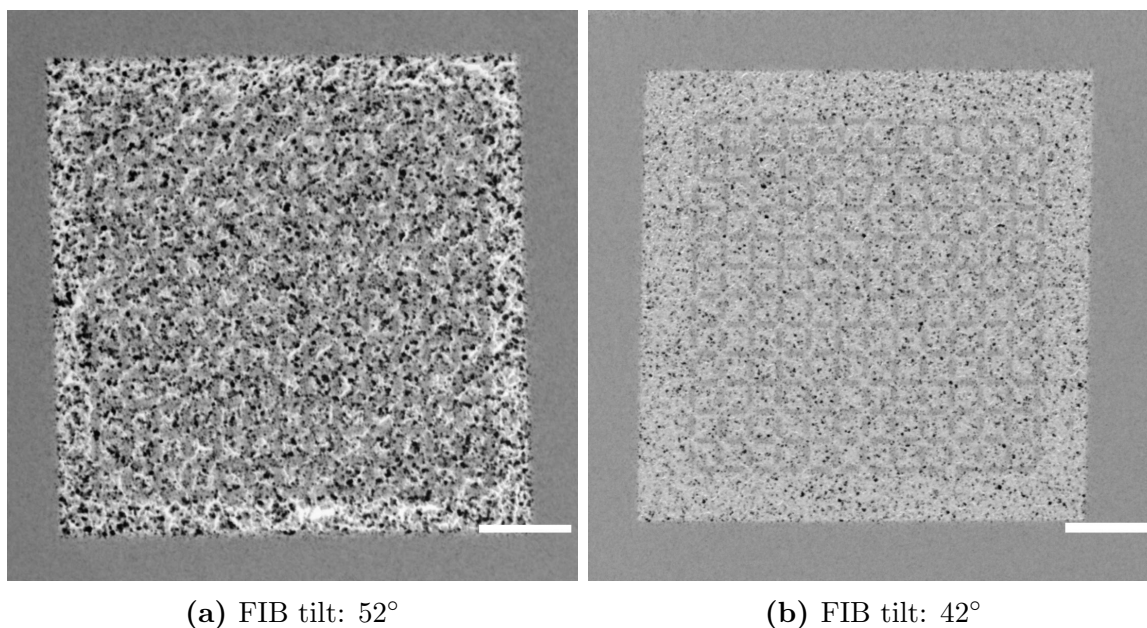


**Figure 5.4: Channeling effects when varying milling angle |** Reconstructed BF image captured at 0° tilt in LMSTEM. Scale bars are 2  $\mu\text{m}$ .

more diffraction contrast compared to Figure 5.4b, which can be observed as a higher amount of darker grains in the milled area. Grains with low-index crystallographic orientation parallel to the ion beam will undergo a lower sputtering yield in the FIB, compared to grains aligned in other orientations, due to reduced interaction with the  $\text{Ga}^+$  ions [36]. Additionally, the sputtered material is likely to be re-deposited onto the non-milled grains, causing these grains to grow in size [34]. If milled along the same axis as imaged in STEM, these grains can show up in the BF image as dark grains because they Bragg scatter to wider angles, causing most of the intensity to fall outside of the doughnut-shaped ADF detector. This is observed as stronger diffraction contrast in Figure 5.4a where both the ion beam incidence angle in FIB and electron beam in the STEM is normal to the specimen, compared to when the relative angle between the two is 10°, as in Figure 5.4b, where the diffraction contrast is significantly minimized. Consequently, strong diffraction contrast in STEM is attributed to channelling effects during FIB milling and can be mitigated if tilting off the milling axis when imaging in STEM.

To further investigate this phenomenon, another experiment was performed with a pinwheel lattice, although the effect is independent of geometry. Continuing on the previous result shown in Figure 5.4b, a structure was milled 10° off the normal ion incidence angle. By tilting the sample in STEM, it was observed that at -10° tilt (Figure 5.5a), diffraction contrast was similar to that observed in Figure 5.4a. This suggests that we are close to being aligned with the milling axis, confirming what was discussed above. The diffraction contrast is strongly minimized when tilting away from the milling axis, shown in Figure 5.5b and Figure 5.5c for 0° and +10°, respectively.

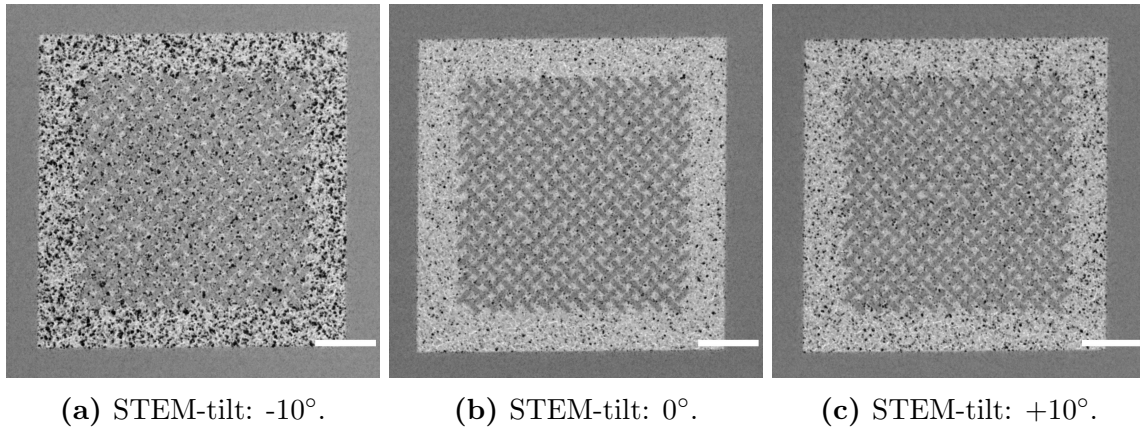


**Figure 5.5: Diffraction contrast is reduced by tilting the specimen off the milling axis** | Reconstructed BF images of a pinwheel lattice milled  $10^\circ$  off the specimen normal. The images demonstrate the effect of channelling and diffraction contrast and its relation to tilt angle in STEM. Scale bars are  $2\ \mu\text{m}$ .

To work around this issue, we can either stay on the positive tilt side or attempt to rotate the structure to eliminate some diffraction contrast.

At last, it should be examined whether this effect is just structural contrast or if it actually affects magnetic contrast. By examining the decomposed DPC signals (DPCy is shown here) for the three data sets, it is observed little to no difference between the three results. This is shown in Figure 5.6. This illustrates that diffraction contrast evens out for regular ADF-STEM-DPC data, where a data set composed of four images is combined into DPCx and DPCy by subtracting the data acquired from two opposing sides of the ADF detector. To obtain the reconstructed BF images, the

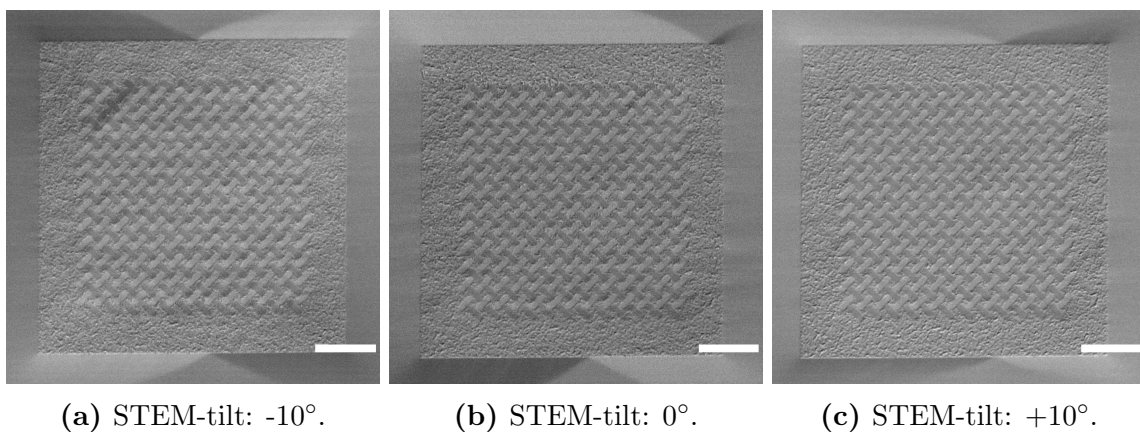


**Figure 5.6: DPCy is independent of diffraction contrast** | DPCy component of the same data sets shown in Figure 5.5, showing no significant changes of magnetic contrast in the milled areas. Scale bars are  $2\ \mu\text{m}$ .

four signals are added together as described in subsection 3.2.2. For the continuous STEM-DPC method, however, this issue is not as easily avoidable since only one probe position on the detector is used to acquire data. Therefore, it seems like a win-win situation to continue to mill off the normal incidence angle. Not only to obtain good pattern fidelity in FIB but also to reduce diffraction contrast in STEM.

### 5.3 Analysis of ADF STEM-DPC Data

It has already been shown that the ADF-STEM-DPC method yields good magnetic contrast. Bekkevold even showed that using the ADF detector yields near identical magnetic contrast as that obtained with a MerlinEM DED [31]. In the data shown in the previous chapters, the milling process and STEM-DPC alignment method were not fully optimized. In this section, we will present the final results in this study after optimizing both fabrication and the two characterization methods, ADF-STEM-DPC and continuous tilt STEM-DPC. The structures that were studied can be observed in Table 3.1. In order to organize the many results obtained in this work, data from the pw, sq, and kagome lattices are collected in separate tables. Data from pw in size M, S, S spaced, XS (two data sets), and XS spaced can be found in Table 5.1. Whilst the results for sq and kagome can be found in Table B.1 and Table C.1, respectively. However, the kagome lattice will not be discussed in this work, as the results do not provide any new information about the employed methods techniques. These tables contain the bitmap used, reconstructed BF image, colourized vector maps with and without the mask as well, as the two components of the vector map, DPCx and DPCy. If details about certain data sets are discussed, this will be enhanced in separate figures. The tables are mostly meant to guide the reader through the discussion and can be used as reference tables.

#### 5.3.1 The Square Lattice

If we analyze the S-sized square lattice shown in Figure 5.7, we see that the ADF-STEM-DPC method successfully captures the in-plane magnetization within each island of the square lattice. The colours represent the magnitude and direction of magnetic induction vectors as shown in the colour wheel. This is particularly visible in the inset to the right, where the corresponding schematic clearly shows the direction of magnetic induction in each island, annotated with arrows. Sometimes it can be easier to analyse the DPCx and DPCy signals because of less apparent "magnetic" contrast from the milled areas. DPCy clearly shows two brighter chains of connected islands. This might be an emergent property of ASI called magnetic monopoles, but this goes beyond the scope of the present work [1, 4]. For DPCx, this contrast is less prominent, but some patchy-looking contrast can be observed randomly across the milled areas. This was not observed in any of the other data sets, except for in the kagome DPCx signals in Table C.1. The reason for the patchy contrast in the DPCx images remains undetermined in this study.



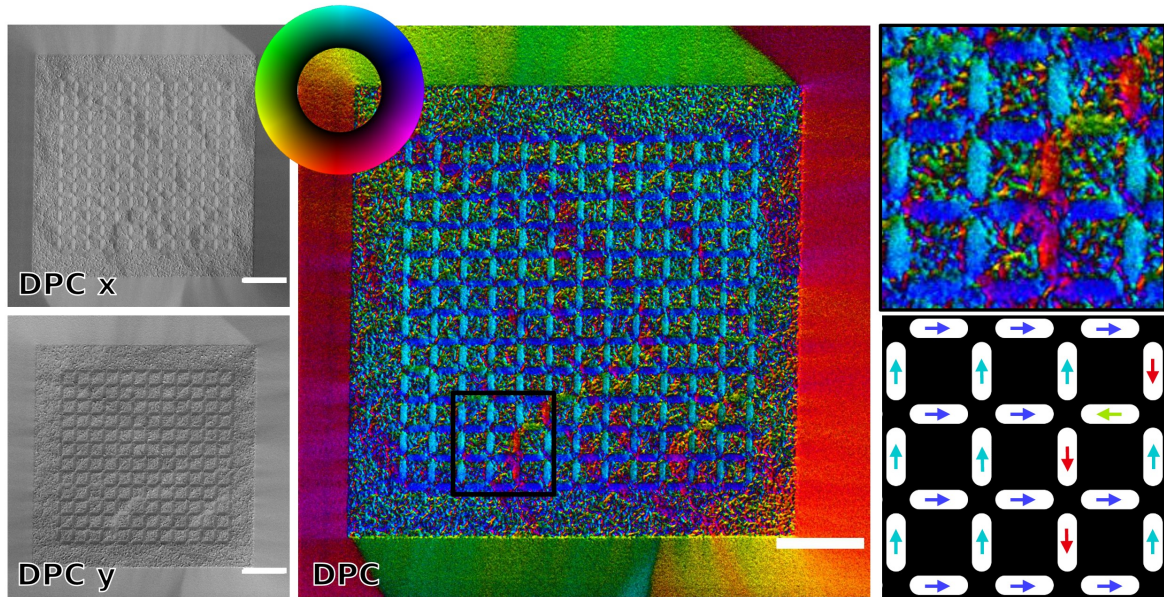


**Figure 5.7: ADF-STEM-DPC data of an S-sized sqASI** | Analysis of a sqASI shows that almost all vertices are aligned in type 2 configuration. A few other vertex configurations can also be observed, such as type 1. Scale bars are 2  $\mu\text{m}$ .

It is observed that almost all islands are aligned with their magnetization along two primary directions, namely up and to the right. We recognize this from Figure 2.6 as type 2 vertices. The specific configuration in the observed case is shown in Figure 5.8b with (turquoise) up-magnetization for vertical islands and (blue) right-magnetization for horizontal magnets, resulting in a net magnetization in the upper right direction. Following the arguments presented in subsection 2.1.7, it was expected that type 1, as shown in Figure 5.8b, would be the most favourable vertex state. However, this

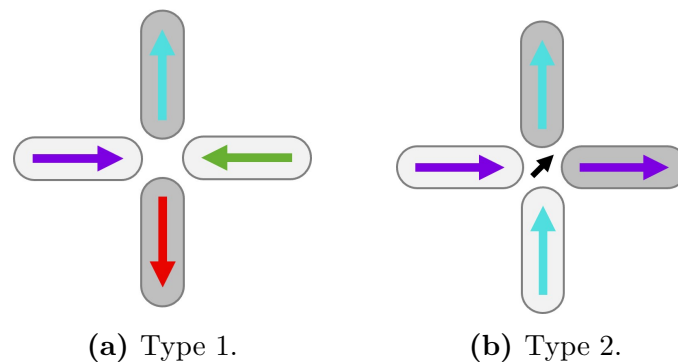


**Figure 5.8: Observed vertex states in sqASI** | The most energetically favourable type 1 vertex state versus the most observed type 2 vertex state in Figure 5.7. Refer to Figure 2.6a to see all four vertex types for sqASI.

state was only observed in some parts of the structure (see inset in Figure 5.7). This can for example be due to irregularities and defects introduced during FIB milling or thin film deposition. Most likely is it due to a slight tilt of the sample resulting in a non-uniform external field across the specimen.

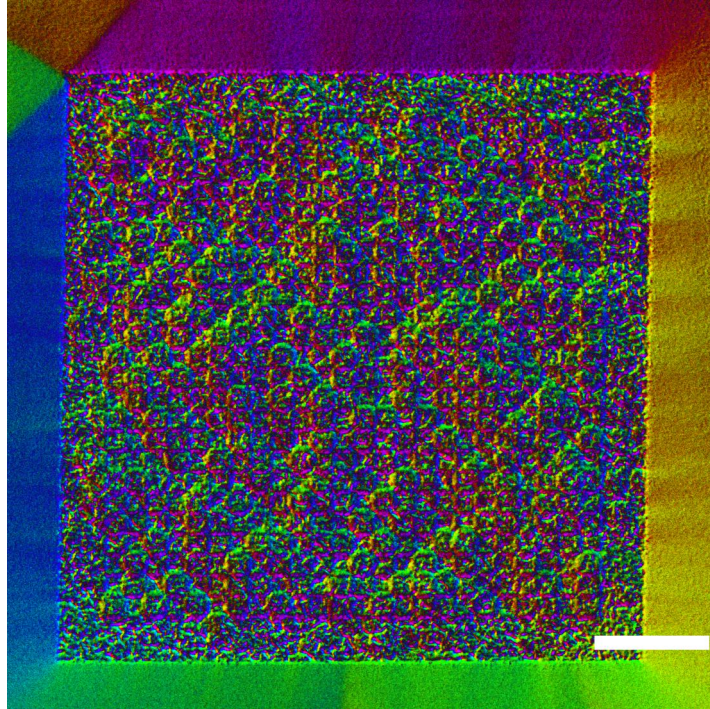
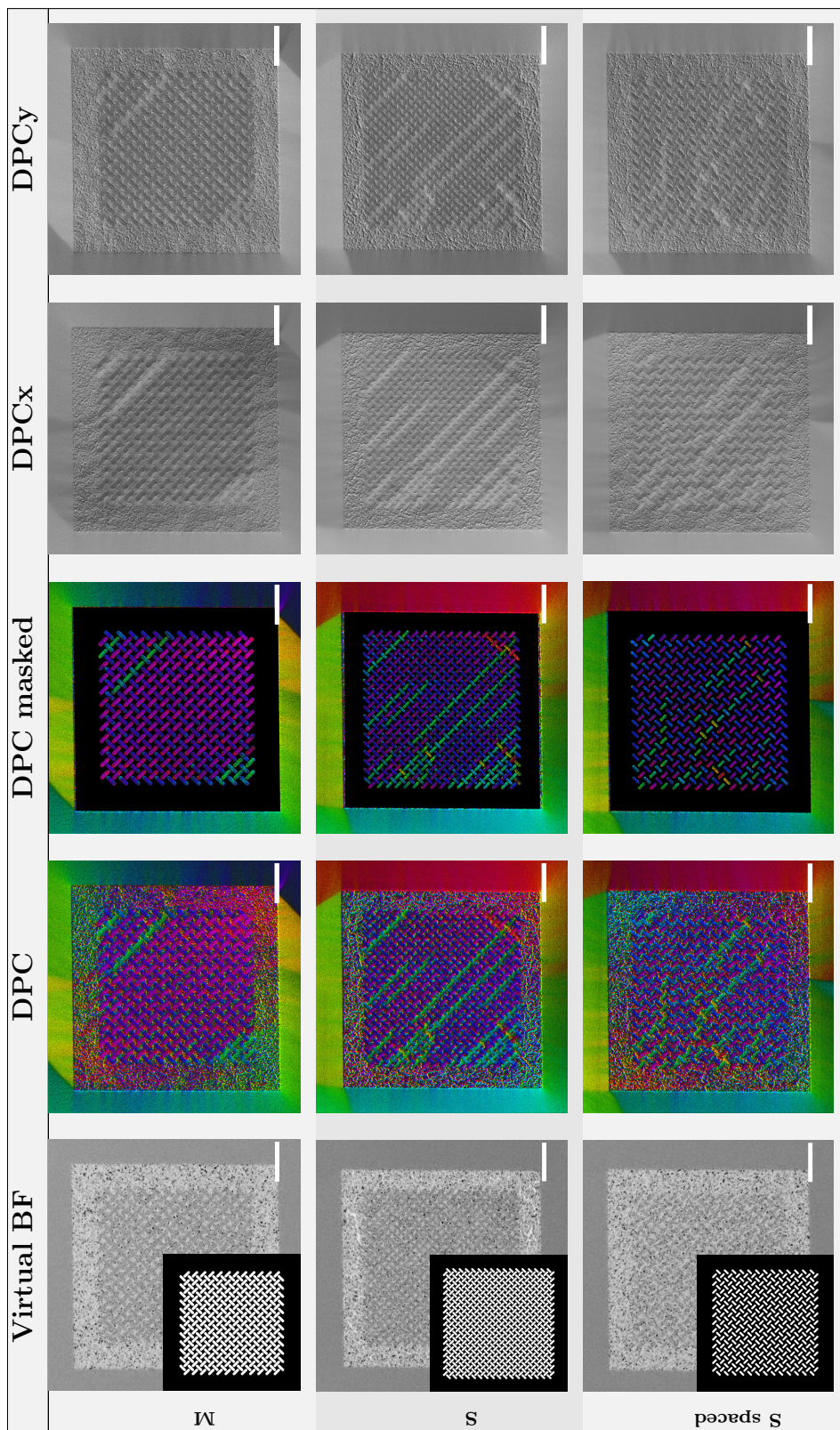


**Figure 5.9: ADF-STEM-DPC image of XS sqASI | DPC signal** of an XS sqASI showing tendencies of a low-energy state as shown in Figure 2.6a. Scale bar is 2  $\mu\text{m}$ .

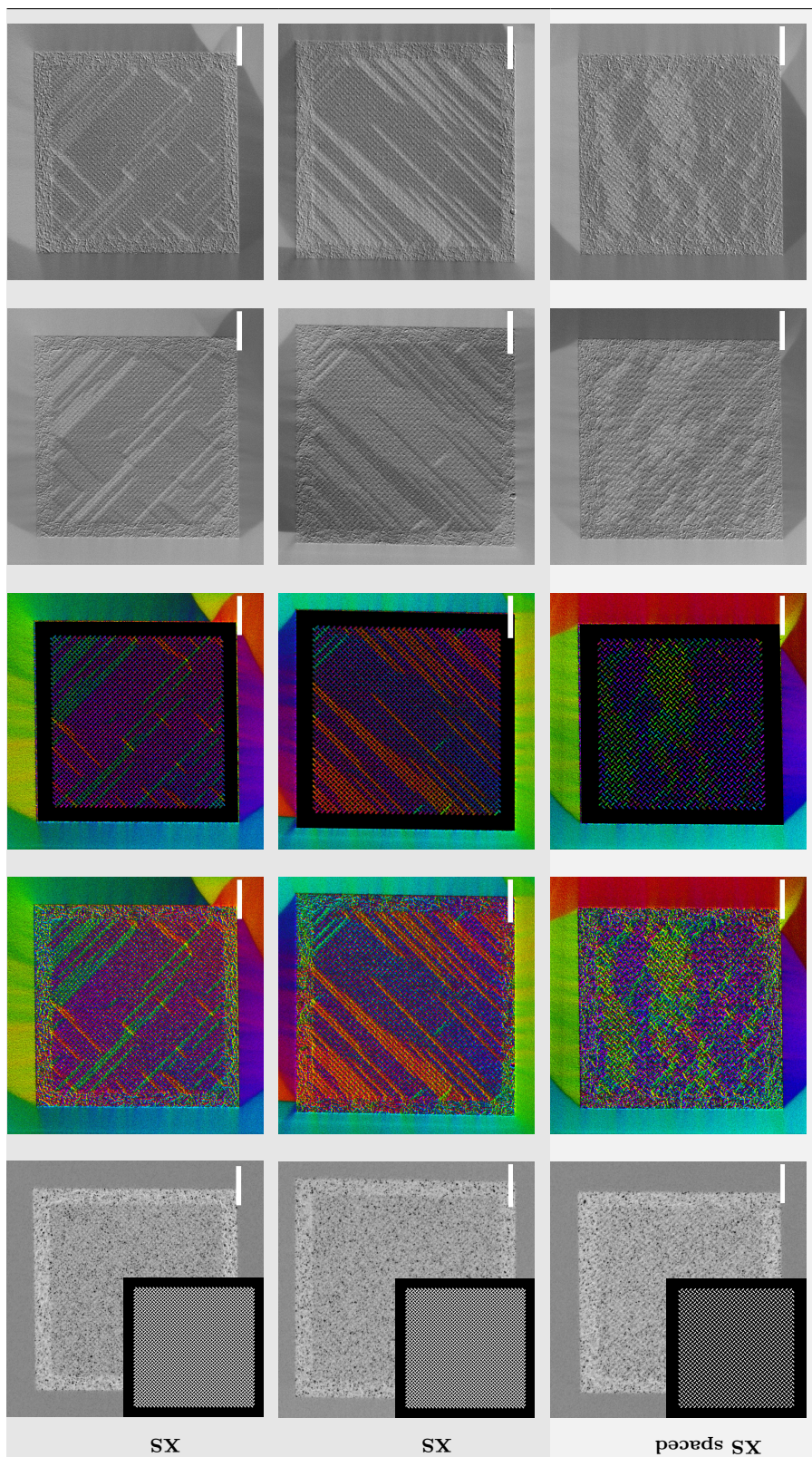
To make sure the magnetic field is normal to the specimen, the specimen can be tilted to obtain a uniform field across the specimen, as discussed earlier and partially demonstrated in Figure 5.2b. This was done for the XS sqASI shown in Figure 5.9. The structure only shows tendencies of the low-energy type 1 states, although the contrast from the milled areas makes this quite difficult to observe. Observing the lowest energy state of type 1 vertices as shown in Figure 5.8a, was found to be challenging when not manipulating the temperature. This is expected, particularly when the specimen is located inside a TEM column surrounded by a residual magnetic field of approximately 35mT. Moreover, a slight mis-tilt of the specimen or structural defects could cause another state to be more favourable than what is discussed in subsection 2.1.7.



**Table 5.1: ADF-STEM-DPC results of pwASIs |** Bitmap mask, reconstructed BF image, vector map with and without a mask as well as DPCx and DPCy for the studied pw structures. Note that M spaced was not imaged with this technique. Scale bars are 2  $\mu\text{m}$ .







### 5.3.2 The Pinwheel Lattice

In general, when analyzing the results shown in Table 5.1, it is observed that the ADF-STEM-DPC method is clearly able to extract information about magnetization direction and visualize this in vector maps. Because the contrast is not observed in the reconstructed BF images, this is a solid indicator of true magnetic contrast. The colours clearly show that the magnetization is aligned along the easy axis of each island, with pink and blue for the pwASIs indicating that the structures mostly show type 2-like vertices, as illustrated in Figure 5.10a. This is in line with the theory presented in subsection 2.1.7, which states that pwASI is ferromagnetic, and type 2 being the lowest energy state. Other vertex states are also observed, such as icing type 3 as illustrated in Figure 5.10b.

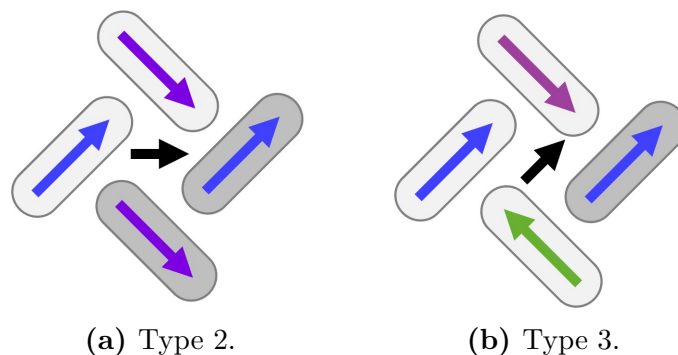


**Figure 5.10: Observed vertex states in pwASI** | Two of the most commonly observed vertex states in Figure 5.11. Refer to Figure 2.6b to see all four vertex types for pwASI.

Strikingly similar observations to that observed in Figure 5.11 have been reported in the literature, where avalanches of islands flipping their magnetization direction nucleate from the edges of the arrays [41]. This effect is particularly evident for  $XS > S > M$  structures, as shown in Figure 5.11, and can be attributed to the size of the islands. As discussed in section 2.1, for the islands to be well coupled through their stray fields, they have to be single-domain and put close to each other. This arrangement maximizes the stray field interaction (as depicted in Figure 2.2a), allowing neighbouring islands to easily flip their magnetization when the surrounding field is changed. This results in the collective behaviour that is characteristic of ASI systems.

However, in the case of the lattices with larger pitch, namely S spaced and XS spaced, we observe little to no such behaviour (see Table 5.1). S-spaced structures only exhibit a tendency towards the streaky pattern, while XS-spaced structures seem to align the islands into larger domains rather than nucleating row by row. This behaviour can be attributed to the spacing ( $r_{ij}$ ) between neighbouring islands.

Upon closer examination of the M- and S-sized structures in Figure 5.11a, we notice some uneven colouration at the short edges of the islands, which may indicate that the islands are not truly single domains. It is possible that the spins at the edges of the islands are bent due to the strong stray field from neighbouring islands. This is a well-



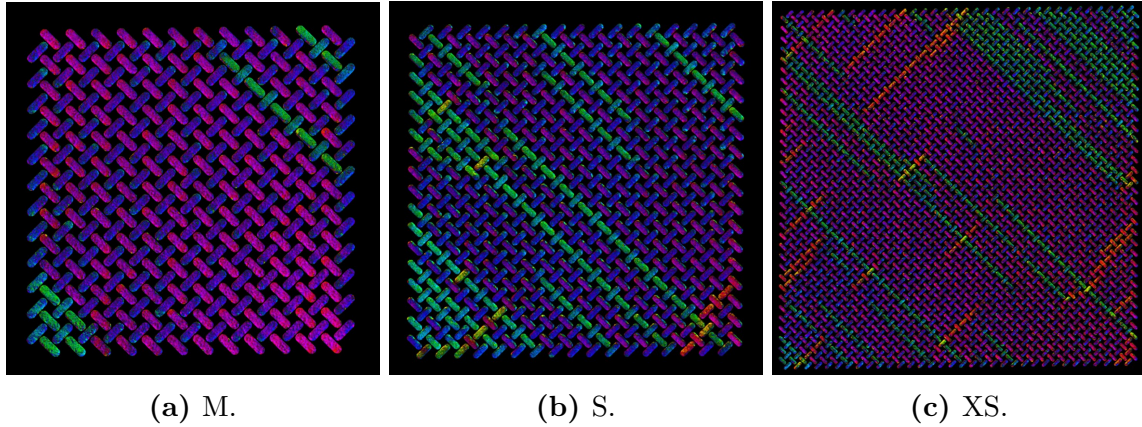


**Figure 5.11: Size of ASI islands changes the emergent behaviour of the system** | ADF-STEM-DPC images of three sizes of pwASI: M, S and XS. Scale bars are  $2\ \mu\text{m}$ .

known phenomenon in ASI literature [42–44]. Alternatively, this uneven colouration could be a result of the electron beam’s sensitivity to stray fields from surrounding islands. Furthermore, we observe up to eight different colours for the islands in the XS lattice in Figure 5.11c, whereas only four colours (green for upper-left, blue for upper-right, orange for lower-left, purple for lower-right) were expected due to the geometry and restricted binary alignment of magnetization within each island. This is more visible when investigating the non-masked DPC signal of the two XS pwASIs in Figure 5.12.

If carefully analysing the colours, we observe that the nuances of each island shift slightly, but in an organized manner, depending on the magnetization in the surrounding islands. If we start by analyzing the sublattice with islands aligned with  $+45^\circ$  rotation (positive rotation counterclockwise), we see that most of the time, when surrounded by blue (up/right on the colour wheel) islands, they are purple (down/right). However, these purple (down/right) islands shift to red (down) in proximity to orange (down/left) islands. If the magnetization in these islands is flipped, they become green (up/left). This green colour is also observed to shift  $\pm 45^\circ$  on the colour wheel, into two other nuances of green, to lime green (up/left) and sea green (up/right), depending on the magnetization of the neighbouring islands.

The same concept applies to the sublattice with islands rotated  $-45^\circ$ . As shown in Figure 5.12, these islands are most of the time blue (up/right), but shift towards turquoise (up) when surrounded by green islands (up/left). When the magnetization is flipped, they are orange (down/left). However, this orange colour seems yellow (left) when surrounded by green (up/left) magnets. All of this either suggests that the magnetization within each single-domain nanomagnet is not indeed binary, or (more likely) that the STEM-DPC method is sensitive for neighbouring stray fields when scanning magnetic induction from structures at this small size scale. This is probable because the strong stray fields should reach far enough to flip neighbouring islands, therefore they could easily also affect beam deflection. A large probe would enhance

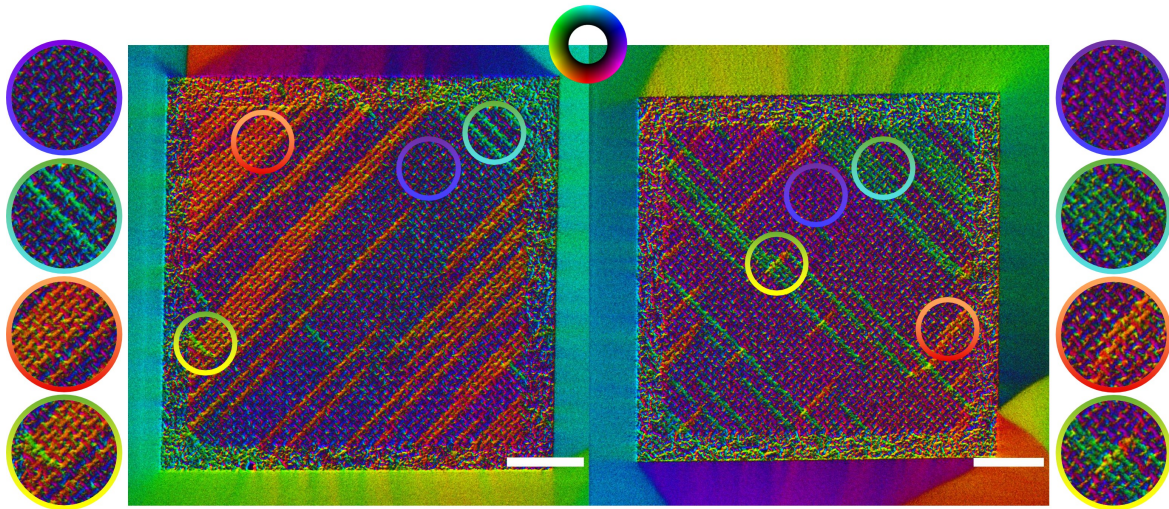


**Figure 5.12: Stray fields from neighbouring islands** | Up to eight nuances of colours were observed in the XS pwASI data. This was believed to be an effect of the beam being deflected by the stray field originating from the surrounding islands. Both scale bars are 2  $\mu\text{m}$ .

this effect, which is the case in non-corrected LMSTEM mode, hence the terrible structural contrast. A third reason could of course be that this is due to the disturbing contrast from the milled areas in between each island. Because this is so systematically observed in multiple data sets, this reason is neglected. Although it does underscore the need for better fabrication methods. A fourth, and quite probable reason, could be a misalignment of the magnetic induction zero-point, or uneven intensity distribution due to e.g. de-scan. This should have been accounted for in the data processing when levelling the intensity using the milled frame around the ASI, as described in subsection 3.2.2. When only using the corners of the image to do the intensity levelling, we observed that the colours varied from one side to the other, indicating that we still had some de-scan in our data. However, in the new and processed data shown here, using the milled frame to level intensity, we were able to successfully remove the de-scan from the data.

In conclusion, it is believed that this effect is due to the beam being deflected by stray fields originating from the surrounding islands. If that is true, this could be resolved by obtaining a smaller and more localized probe scanning across the specimen at the image plane, for example by installing aberration correction for the LMSTEM mode. Aberration correction can significantly reduce probe size and thus improve the spatial resolution, enabling better control and characterization of the individual islands in the ASI structures. With a smaller scanning probe, the effect of neighbouring stray fields will also be minimized, possibly allowing for more localized magnetic imaging.



### 5.3.3 Combining ADF-STEM-DPC and Sample Tilt

Even though the ADF-STEM-DPC method provides a lot of valuable information about our magnetic system, it is difficult to draw conclusions about the dynamic behaviour with this method alone. One way to explore the system's dynamics is to tilt to a certain angle, tilt back to  $0^\circ$ , and then image the new state which is possible because of the hysteresis nature of magnetic structures. This approach was done to image the square lattice with XL-sized ( $1800\text{nm}\times 600\text{nm}$ ) islands and the results are shown in Figure 5.13. The magnetization directions are clearly shown, with most of the islands showing multi-domain behaviour, or at least bending of the spins at the edges. This is a known effect in literature [42, 44], and one of many effects that can be studied using this method. It is also observed that the domains are switching in-plane, and probably clockwise, as observed from the vertical sublattice switching from red to blue to green. It is assumed that the same applies to the horizontal sublattice, but that this switching appears faster than the vertical sublattice. The results shown in Figure 5.13 can be more thoroughly studied, but this is merely shown as an example

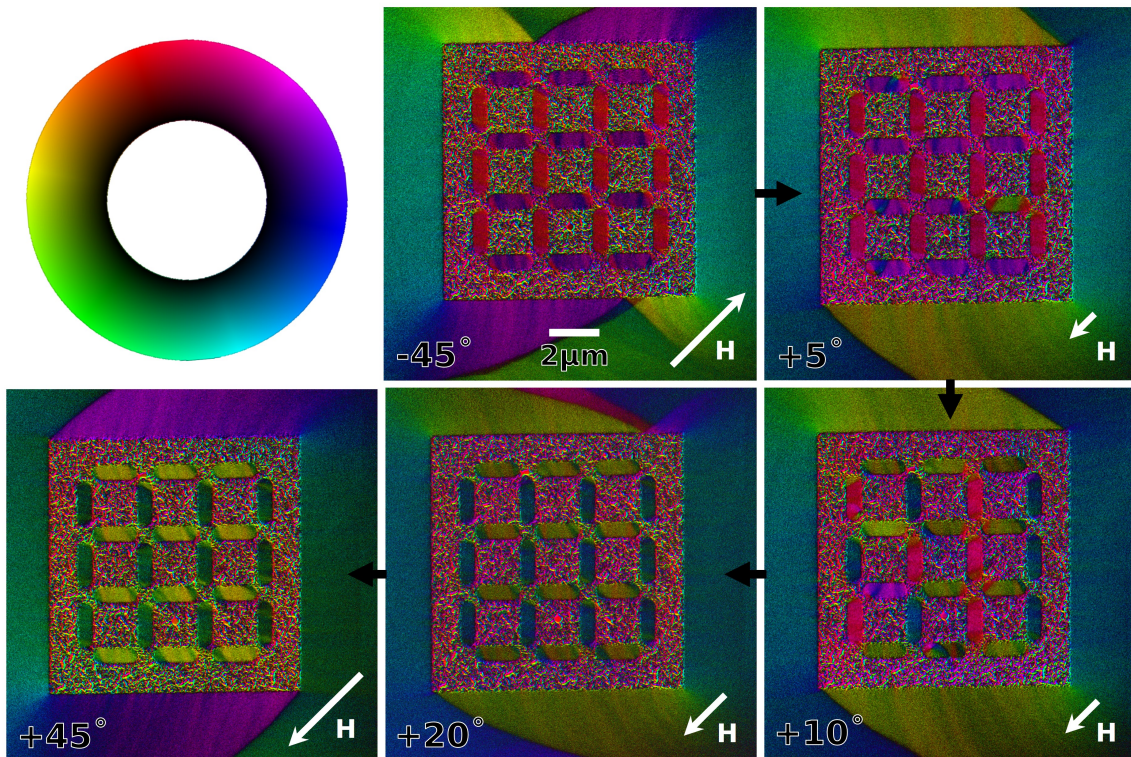


**Figure 5.13: ADF-STEM-DPC showing domains in XL-sized islands** | Magnetic reversal in a square lattice with XL-sized islands. The structure is first tilted to the desired tilt angle, and then tilted back to  $0^\circ$  where four images are acquired to obtain a complete data set with the ADF-STEM-DPC method, as described in subsection 3.2.1.



of how we can utilize ADF-STEM-DPC and sample tilt to conduct a detailed analysis of a magnetic system.

Acquiring meaningful data sets, without a priori knowledge of the domain structure, proves challenging. For the data shown in Figure 5.13, we captured four images to complete a data set for every  $5^\circ$  degrees in both positive and negative tilt direction. This was time-consuming and resulted in many useless data sets which did not provide any new information. Hereby, a rapid and exploratory method was developed, called continuous tilt STEM-DPC (see subsection 3.2.3). By first applying this in-situ exploratory method, it becomes possible to explore the dynamics of our system, and subsequently select the best tilt angles, or magnetic field strengths, to always image unique and interesting states of our structure. Note that this only works well for reversible systems, which luckily applies to most magnetic systems due to hysteresis. By combining these two methods, time and resources can be saved and it becomes feasible to perform controlled and efficient experiments to learn more about a wide range of magnetic systems.

## 5.4 Analysis of Continuous Tilt STEM-DPC Data

In addition to the ADF-STEM-DPC method discussed in the following section, we also used the continuous tilt STEM-DPC technique to in-situ characterize the dynamic behaviour of the magnetic systems. This technique is described in detail in subsection 3.2.3. Instead of capturing four images, the continuous tilt STEM-DPC involves continuously tilting the specimen while acquiring images. The results obtained were found to be significantly improved when milling off the incidence angle, thereby minimizing diffraction contrast at  $>0^\circ$  tilt. This technique allows for a more dynamic observation of the structures, and the structure's response to changes in the magnetic field, by changing the tilt angle.

A way to observe ASI behaviour is by analysing whether the system behaves in a collective manner or not, meaning the individual magnetic islands are coupled together by their respective stray fields. As elaborated in section 2.1, each magnetic island should be single-domain to maximize stray field, and like so enhance the stray field coupling. The level of coupling can be determined by analyzing how the system responds to external stimuli such as a magnetic field.

Let us begin by examining a subset of a tilt series obtained using the continuous tilt STEM-DPC method on a square lattice with L-sized ( $900\text{nm}\times 300\text{nm}$ ) islands. This was done as explained in subsection 3.2.3, by capturing a stack of  $768\times 768$  pixelated images with the lowest possible dwell time of  $8\mu\text{s}$ , resulting in approximately 3 seconds acquisition time per image. Before the stack was acquired, the structure was tilted in opposite tilt direction to ensure magnetic saturation, and then back to  $0^\circ$ . The specimen was then tilted  $0.5^\circ$  after each capture up to  $20^\circ$ , resulting in 40 images in this exact tilt series. In FLC, the projector lens was set to its maximum, and here the OL was adjusted to a value of 256 ( $\approx 55\text{mT}$ ). Note that in the other tilt series presented, the OL was not excited. This is because the data in Figure 5.14 was acquired when the alignment procedure was still under refinement and when experimenting with the OL values was done.

Figure 5.14 displays five selected images of the tilt series captured at different tilt

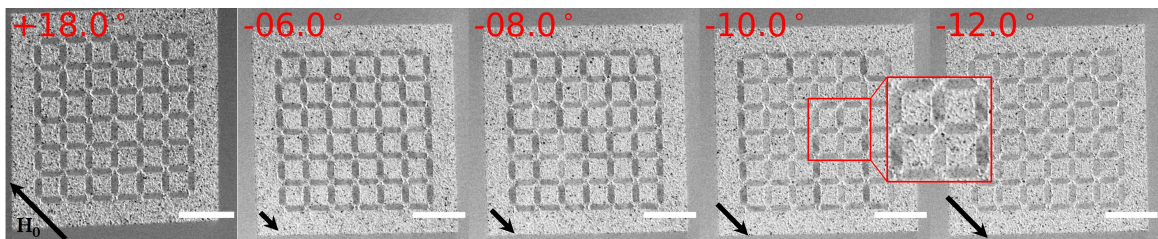


**Figure 5.14: Tilt series of a square array with L-sized islands** | Continous STEM-DPC results of an array with L-sized ( $900\text{nm}\times 300\text{nm}$ ) magnets showing a gradual transition from being magnetized along the  $\mathbf{H}_0$ -field (darker contrast) to  $-\mathbf{H}_0$  (lighter contrast). The islands are too large to be single domains, and switching can be seen for separate domains in the inset of  $-10^\circ$  tilt.

angles. By tilting the specimen, the external magnetic field  $\mathbf{H}_0$  is changed across the sample. At  $+18^\circ$  tilt, it was visually apparent that the structure could not be further magnetized, leading us to assume that we had reached the point of magnetic saturation  $M_s$ , as depicted in Figure 2.5.

When tilting in the opposite direction, i.e. applying a field  $-\mathbf{H}_0$ , it takes some time before changes become noticeable. This corresponds to the part of the hysteresis curve from  $M_s$  down to the point of remanence  $M_r$ , which occurs at  $-6^\circ$  tilt as seen in Figure 5.14. After tilting across the  $0^\circ$  point, a gradual change in contrast within each island becomes apparent. This can be observed in the images captured at  $-6^\circ$ ,  $-8^\circ$ , and  $-10^\circ$  tilt. The change in contrast suggests that we have reached the point of coercivity  $-H_c$ . Upon closer inspection, particularly in the inset of  $-10^\circ$  tilt, we can even observe individual domains within each island flipping one by one, rather than the entire island flipping simultaneously. This is because the L-sized islands are too large for them to energetically align as single domains when put in arrays, i.e.  $E_{MS} < E_{Ex}$ . When further increasing the field by tilting the sample to  $-12^\circ$ , the point saturation magnetization is reached again, but in the opposite direction,  $-M_s$ .

For single-domain magnets, we would expect a larger  $E_{MS}$  than what was observed for the L-sized islands in Figure 5.14, due to more energy stored in the demagnetization, or stray field  $\mathbf{H}_d$  as seen in Figure 2.2a. This is because the strong, but short-range exchange interactions *win* over the magnetostatic energy at small size scales. The exchange energy prefers parallel alignment of magnetic dipole moments, which is the reason that domain walls cost energy, and sufficiently small magnets are single-domain. When we compare the L-sized lattice in Figure 5.14 to tilt series of square M, S and XS (see Zenodo, code 8015634), we do indeed observe that there is stronger coupling between the smaller, S- and XS-sized, single-domain islands than it is between the L- and M-sized islands. This result is consistent when analysing all the structures, pinwheel, square and kagome. Smaller islands, especially when put close together or in a lattice with tighter spacing (pinwheel vs square), are coupled more strongly together than larger islands. This is in line with the theory. The data sets for all the tilt series are uploaded to Zenodo (8015634).

This size dependency when it comes to the coupling between islands is also visible

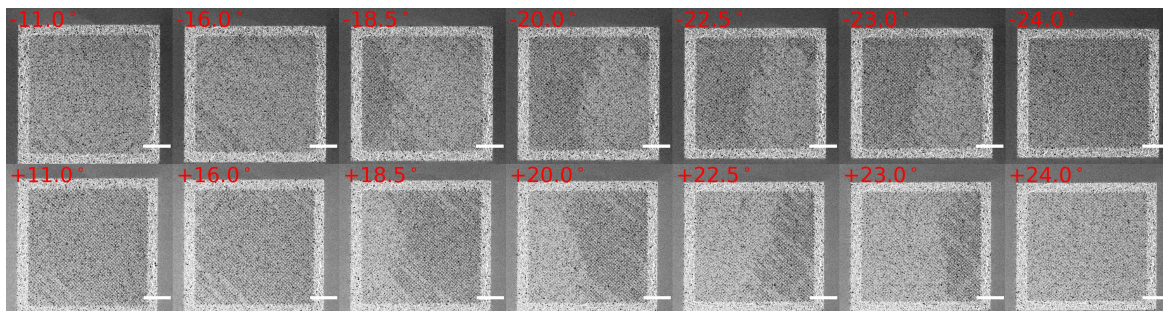


**Figure 5.15: Dynamic tilted STEM-DPC series of an XS-sized pinwheel** | Collective behaviour is seen for XS pwASIs. Scale bars are  $2\mu\text{m}$ .

for the pinwheel lattices. Where XS shows significantly faster and more connected switching behavior than S and M. This is shown in the selected images from a tilt series of one of the two pwASIs (the upper XS in Table 5.1). The contrast shifts from light to dark or vice versa, depending on the tilt direction and probe placement on the ADF detector. We observe a similar behaviour, although more streaky, in the other XS structure (see Figure B.1). This could be attributed to small defects in the system, causing nucleation of edge islands, and causing certain rows of islands to flip more easily than others. Such dynamic behaviour is commonly observed in ASI structures and is not an uncommon result [3, 16, 45].

With this tilting method, information about when each island switches its magnetization can be extracted and mapped like shown in Figure 5.16. This way it is possible to compare patterns in the switching dynamics, and link certain behaviours to certain parameters. For instance, Figure 5.16 compares two pwASIs with M-sized islands, but with two different pitch values. By mapping the flipping behaviour in colours, we can identify which magnets flip first (blue) and which flip last (red). We observe that the pinwheel with closer spacing (30 nm pitch) exhibits stronger coupling compared to the spaced version (105nm pitch). This is expected because the strength of the stray field decays with distance from the magnetic structure the stray field originates from [21].

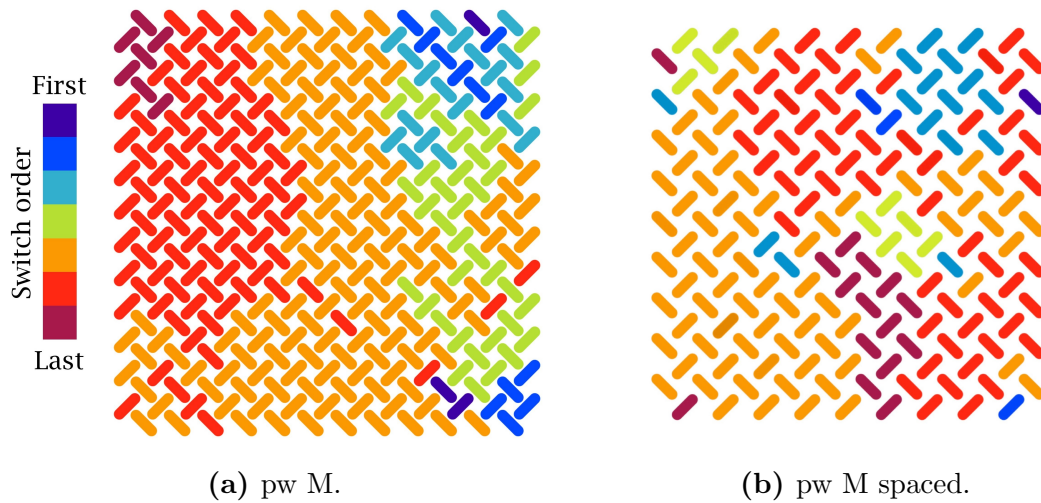


**Figure 5.16: Switching data of pw M versus pw M spaced |**  
 The pwASI with smaller spacing between neighbouring islands shows significantly more coupling than the one with more space between the islands. Figure inspired by [16]

Another interesting comparison is to study the dynamics in the pinwheel versus that in the square lattice. Taking the S-sized pwASI and sqASI as examples, it is observed in Figure 5.17 some differences in how the structures behave as a response to changes in  $\mathbf{H}_0$ . These differences can be attributed to the geometrical differences between the two structures. The pwASI undergoes rapid and almost simultaneous flipping of magnets. Although, due to the limited time resolution of our method (taking one image per tilt), we cannot access what switching dynamics actually occur in this one step (shown in



red). This may be accessed if reducing the tilt step to  $0.1^\circ$ , or by using a fast DED to acquire video data, as mentioned earlier. Anyhow, the S-sized pwASI demonstrates a higher degree of responsiveness and collective behaviour compared to the S-sized sqASI. This is most likely due to the lattice geometry. Instead of the preferred head-to-tail vertex configuration in the square lattice, the pinwheel magnets have their heads and tails positioned at the middle of the next magnet. This geometric difference allows for stronger binding between the islands through the stray fields, resulting in enhanced coupling. Ergo, pinwheel lattice shows more coupling between the islands. It is also important to mention that these two ASI systems are expected to behave inherently different and to remember that sqASI is an antiferromagnetic system and pwASI a ferromagnetic one. A similar pattern of switching in sqASI was also seen by Paterson et al. [16].

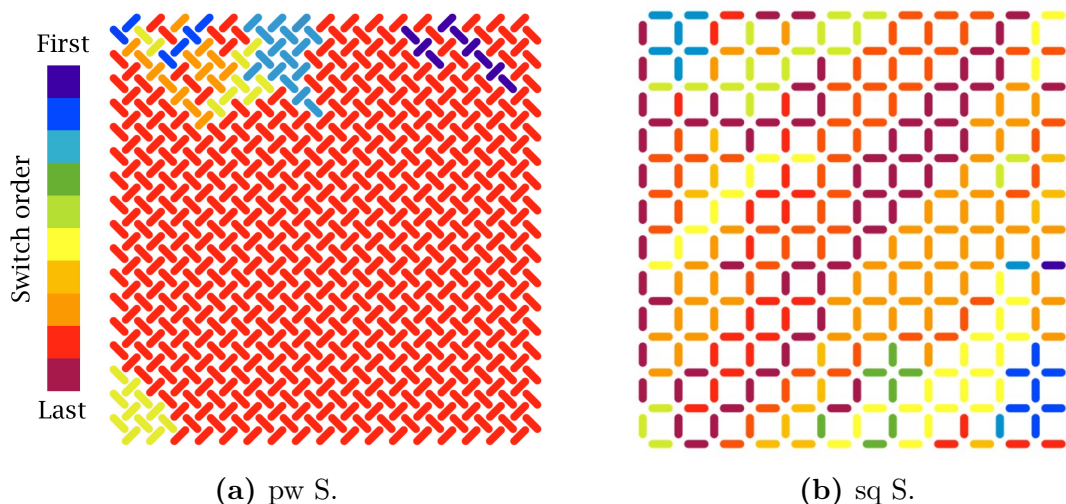


**Figure 5.17: Switching data of pw S versus sq S** | The S-sized pinwheel lattice switches in a completely different manner than the S-sized square lattice.

## 5.5 Summary of the Findings: Characterization

In conclusion, the findings of this study highlight the significant impact lens aberrations such as coma and astigmatism have on data quality in LMSTEM mode. This is because when switching the upper part of the OL pole piece off, the weaker condenser mini lens becomes the probe-forming lens, resulting in more pronounced aberrations. Precisely correcting these aberrations was found to be crucial to obtaining good image quality. Correcting for astigmatism using a milled circle proved to be an efficient method, as alternative techniques such as using the Ronchigram, live image of the specimen, or live fast Fourier transform (FFT) are quite tricky to use in LMSTEM. Correcting for coma was shown to be more challenging and required an iterative approach. Furthermore, it was experienced that the concept *the simpler the better* also applies to alignment in LMSTEM mode. Adjusting e.g. OL and the intermediate lenses with FLC was

not shown to significantly improve the results, and most often caused more de-scan, "bleeding" of magnetic contrast (see Figure 5.3) and aberrations (which is expected when changing the beam path in the column). One adjustment that did in fact yield better results was to set the projector lens value at maximum. This was done to maximize magnetic contrast, by enlarging the camera length.

Another important consideration was the presence of diffraction contrast originating from grain formed during sample fabrication in FIB. By optimizing the milling procedure and aligning the microscope appropriately, the diffraction contrast was significantly reduced or avoided. Continuous tilt STEM-DPC data acquisition proved to be sensitive to grain orientation, and milling off the normal incidence angle, or tilting the specimen off the FIB-milled axis helped mitigate this issue (see Figure 5.4 and Figure 5.5). This did however not seem to affect ADF-STEM-DPC data when acquiring data at the same tilt angles (see Figure 5.6). This can be explained due to magnetic contrast not being dependent on the Bragg diffraction angle. What was observed, however, was some "magnetic" contrast from these milled areas. This is because magnetic contrast is dependent on thickness variations of the specimen through Equation 2.6, and therefore surface roughness, i.e. changes in thickness, will also cause deflections of the beam which will be mapped as false magnetic contrast. A solution to this could be to precess the beam during STEM-DPC to smooth out the contrast within the magnetic islands, and also from the milled areas around the islands. This technique is explained by [46], using a pixelated detector. It could, however, be interesting to test out, and then compare to the results obtained with this method, to see if e.g. the colour changes in Figure 5.12 would be any different.

Lastly, entering the nano realm is known to result in many interesting physics phenomena, including the magnetic properties of nano-sized structures [47]. The final results showed that smaller islands show more ASI behaviour, which is expected based on the theory presented. Domain formation is a competition between magnetostatic energy, which prefers to create domain walls, and exchange energy, which prefers to align its spin parallel to one another, therefore making it costly to rotate the spins to create domain walls. At these small dimensions short-range interactions, like exchange interactions, *win* over magnetostatic energy, resulting in single-domain magnets. Additionally, the magnetization direction can be modified by adjusting the shape. Elongated single-domain magnets like the Permalloy islands in our ASI structures, are forced into binary configurations because they prefer to align their magnetization along the easy axis. The thinness relative to the size of the islands can also force the magnetization to be in-plane, which is favourable in this case as STEM-DPC is only able to image in-plane magnetization. Even though the collective ASI behaviour is most prominent for XS-sized pwASI, the larger-sized pwASIs like S-sized and M-sized do also show tendencies of ASI behaviour, also observed by [31]. This can be explained by Figure 2.2b, where some magnetostatic energy is stored in the stray field, even though the structure is too large to be single-domain. The switching behaviour of all structures was successfully observed with the continuous tilt STEM-DPC where it was shown that distance between islands results in a weaker connection between the islands (see Figure 5.16, and that the switching behaviour varied with lattice con-

figuration (see Figure 5.17). In conclusion, the continuous tilt method proves to be an excellent approach for studying the collective behaviour of ASI systems. It allows for in-situ experiments, which is a huge advantage when it comes to exploring new magnetic systems and can be combined with ADF-STEM-DPC to explore magnetic reversal within magnetic structures such as the example in Figure 5.13.

## Chapter 6

# Conclusion and Further Work

In this work, we have successfully fabricated a wide range of ASI systems with islands as small as  $225\text{nm} \times 75\text{nm}$  using a FIB. The ASIs were characterized using a conventional ADF detector in non-aberration corrected LMSTEM mode, employing two distinct STEM-DPC techniques. The ADF detector showed advantages over using segmented or pixelated detectors in terms of availability, acquisition time, and low data sizes even for highly pixelated data ( $<200\text{MB}$  for a data set composed of four  $3072 \times 3072$  pixelated images). The combination of fabrication and characterization methods demonstrated exceptional results, indicating the suitability of this methodology for fast prototyping and characterization of ASIs. Moreover, the methodology can be combined with structural and chemical analysis in the TEM, further enhancing its capabilities. STEM-DPC with an ADF detector has proven to be a robust magnetic imaging technique, although it is still in the early stages of development with room for improvement. The challenges related to sample fabrication, including preferential milling by the FIB leading to diffraction contrast and surface roughness, have been identified. These challenges introduce unwanted contrast in the milled areas surrounding the magnetic arrays, making it more difficult to analyze smaller ASI islands. The continuous STEM-DPC methodology enables in-situ studies of magnetic field and temperature responses, facilitating the prototyping and tailoring of ASI systems to achieve desired properties for computing devices. The insights gained from this study also open up exciting possibilities for exploring even larger ASI systems. For instance, it is highly feasible to image pwASIs consisting of over 10,000 XS-sized islands within a  $40\mu\text{m} \times 40\mu\text{m}$  area while maintaining high magnetic resolution in LMSTEM. This is four times larger than the structures studied in this work and can be advantageous to experimentally study complicated ASI structures for novel, low-power spintronic devices. Overall, the methods developed in this study hold great promise for future research endeavours in the study of magnetic structures. The employed techniques, from sample fabrication to data processing, are readily available, efficient and have so far shown excellent results. With the continuous advancement in nanofabrication and characterization techniques, we anticipate that this approach can become a valuable tool and contribute to the understanding and application of ASI systems and other magnetic structures in the future.



---

## References

- [1] S. H. Skjærvø et al. ‘Advances in artificial spin ice’. *Nature Reviews Physics* 2 (2020), 13–28.
- [2] R. F. Wang et al. ‘Artificial ‘spin ice’ in a geometrically frustrated lattice of nanoscale ferromagnetic islands’. *Nature* 439 (2006), 303–306.
- [3] S. Gliga et al. ‘Emergent dynamic chirality in a thermally driven artificial spin ratchet’. *Nature materials* 16 (2017), 1106–1111.
- [4] C. Nisoli. ‘Artificial spin ice: from scientific toy to material by design’. *SPIE Newsroom* (2015).
- [5] I. Gilbert et al. ‘Direct visualization of memory effects in artificial spin ice’. *Physical Review B* 92 (2015).
- [6] J. H. Jensen, E. Folven and G. Tufte. ‘Computation in artificial spin ice’. *Artificial Life Conference Proceedings*. MIT Press One Rogers Street, Cambridge. 2018, 15–22.
- [7] J. H. Jensen and G. Tufte. ‘Reservoir computing in artificial spin ice’. *Artificial Life Conference Proceedings* 32. MIT Press One Rogers Street, Cambridge. 2020, 376–383.
- [8] D. J. Gauthier et al. ‘Next generation reservoir computing’. *Nature communications* 12 (2021).
- [9] H. Y. Kwon et al. ‘Searching for the ground state of complex spin-ice systems using deep learning techniques’. *Scientific Reports* 12 (2022).
- [10] A. Penty and G. Tufte. ‘A representation of artificial spin ice for evolutionary search’. *Artificial Life Conference Proceedings* 33. Vol. 2021. MIT Press One Rogers Street, Cambridge. 2021.
- [11] J. C. Gartside. ‘Controlling magnetic charge landscapes in nanostructures’. PhD thesis. Imperial College London.
- [12] J. H. Jensen et al. ‘flatspin: A large-scale artificial spin ice simulator’. *Physical Review B* 106 (2022).
- [13] V. Kapaklis et al. ‘Thermal fluctuations in artificial spin ice’. *Nature Nanotechnology* 9 (2014), 514–519.
- [14] Y. Li et al. ‘Superferromagnetism and Domain-Wall Topologies in Artificial “Pin-wheel” Spin Ice’. *ACS Nano* (2019).

- 
- [15] A. Talapatra, N. Singh and AO Adeyeye. ‘Magnetic tunability of permalloy artificial spin ice structures’. *Physical Review Applied* 13 (2020).
- [16] G. W. Paterson, G. M. Macauley and Rair Macêdo. ‘Field-Driven Reversal Models in Artificial Spin Ice’. *Advanced Theory and Simulations* 4 (2021).
- [17] X. Zhou et al. ‘Large area artificial spin ice and anti-spin ice Ni80Fe20 structures: static and dynamic behavior’. *Advanced Functional Materials* 26 (2016), 1437–1444.
- [18] G. Yi et al. ‘Influence of end shape, temperature, and time on the switching of small magnetic elements’. *Journal of applied physics* 92 (2002), 6087–6093.
- [19] E. C. Stoner and E.P. Wohlfarth. ‘A mechanism of magnetic hysteresis in heterogeneous alloys’. *Philosophical Transactions of the Royal Society of London. Series A, Mathematical and Physical Sciences* 240 (1948), 599–642.
- [20] J. M. D. Coey. *Magnetism and Magnetic Materials*. Cambridge: Cambridge University Press, 2010.
- [21] M. Getzlaff. *Fundamentals of magnetism*. Springer Science & Business Media, 2007.
- [22] P. Fischer. ‘X-ray imaging of magnetic structures’. *IEEE Transactions on Magnetics* 51 (2014), 1–31.
- [23] J.N. Chapman, R. Ploessl and D.M. Donnet. ‘Differential phase contrast microscopy of magnetic materials’. *Ultramicroscopy* 47 (1992), 331–338.
- [24] A. Lubk and J. Zweck. ‘Differential phase contrast: An integral perspective’. *Physical Review A* 91 (2015).
- [25] A. Farhan et al. ‘Emergent magnetic monopole dynamics in macroscopically degenerate artificial spin ice’. *Science Advances* 5 (2019).
- [26] AC Daykin and AK Petford-Long. ‘Quantitative mapping of the magnetic induction distribution using Foucault images formed in a transmission electron microscope’. *Ultramicroscopy* 58 (1995), 365–380.
- [27] H. Nakajima et al. ‘Foucault imaging and small-angle electron diffraction in controlled external magnetic fields’. *Microscopy* 65 (2016), 473–478.
- [28] S. McVitie, D. McGrouther and Matus Krajnak. ‘High resolution quantitative Lorentz microscopy’. *Journal of Physics: Conference Series*. Vol. 644. IOP Publishing. 2015.
- [29] L.F. Yin et al. ‘Magnetocrystalline anisotropy in permalloy revisited’. *Physical review letters* 97 (2006).
- [30] K.J. Kirk et al. ‘Imaging magnetic domain structure in sub-500 nm thin film elements’. *Journal of Applied Physics* 89 (2001), 7174–7176.
- [31] J. M. Bekkevold. ‘Improving in-situ dynamic magnetic characterisation of artificial spin ice ensembles using STEM’. MA thesis.

- 
- [32] H. D. Arnold and G. W. Elmen. ‘Permalloy, a new magnetic material of very high permeability’. *The Bell System Technical Journal* 2 (1923), 101–111.
- [33] H.S. Yoon et al. ‘Advanced scanning paths for focused ion beam milling’. *Vacuum* 143 (2017), 40–49.
- [34] M. Urbánek et al. ‘Focused ion beam fabrication of spintronic nanostructures: an optimization of the milling process’. *Nanotechnology* 21 (2010).
- [35] J. Orloff. ‘High-resolution focused ion beams’. *Review of Scientific Instruments* 64 (1993), 1105–1130.
- [36] L. A. Giannuzzi et al. *Introduction to focused ion beams: instrumentation, theory, techniques and practice*. Springer Science & Business Media, 2004.
- [37] D. Onderdelinden. ‘The influence of channeling on Cu single-crystal sputtering’. *Applied Physics Letters* 8 (1966), 189–190.
- [38] J. Lindhard. ‘Motion of swift charged particles, as influenced by strings of atoms in crystals’. *Physics Letters* 12 (1964), 126–128.
- [39] I. Utke, S. Moshkalev and P. Russell. *Nanofabrication using focused ion and electron beams: principles and applications*. Oxford University Press, 2012.
- [40] D. A. Gilbert et al. ‘Realization of ground-state artificial skyrmion lattices at room temperature’. *Nature communications* 6 (2015).
- [41] S. Gliga et al. ‘Emergent dynamic chirality in a thermally driven artificial spin ratchet’. *Nature materials* 16 (2017), 1106–1111.
- [42] S. Gliga et al. ‘Broken vertex symmetry and finite zero-point entropy in the artificial square ice ground state’. *Physical Review B* 92 (2015).
- [43] S. Gliga et al. ‘Spectral analysis of topological defects in an artificial spin-ice lattice’. *Physical review letters* 110 (2013).
- [44] C. Phatak et al. ‘Nanoscale structure of the magnetic induction at monopole defects in artificial spin-ice lattices’. *Physical Review B* 83 (2011).
- [45] Y. Li et al. ‘Superferromagnetism and domain-wall topologies in artificial “pin-wheel” spin ice’. *ACS nano* 13 (2018), 2213–2222.
- [46] G. Nordahl and M. Nord. ‘Improving Magnetic STEM-Differential Phase Contrast Imaging using Precession’. *Microscopy and Microanalysis* 29 (2023), 574–579.
- [47] R. Kelsall, I. W. Hamley and M. Geoghegan. *Nanoscale Science and Technology*. Wiley, 2005.

# Appendix

## Appendix A

### Problems Tackled Along the Way

During the hours spent operating the FIB instrument, several issues have emerged, leading to much frustration. One such issue is shown in Figure A.1a, where the ASI pattern has not been accurately processed by the software due to the high level of pixelation in the bitmap ( $4096 \times 4096$ ), thus exceeding the processing capacity of the FIB software.

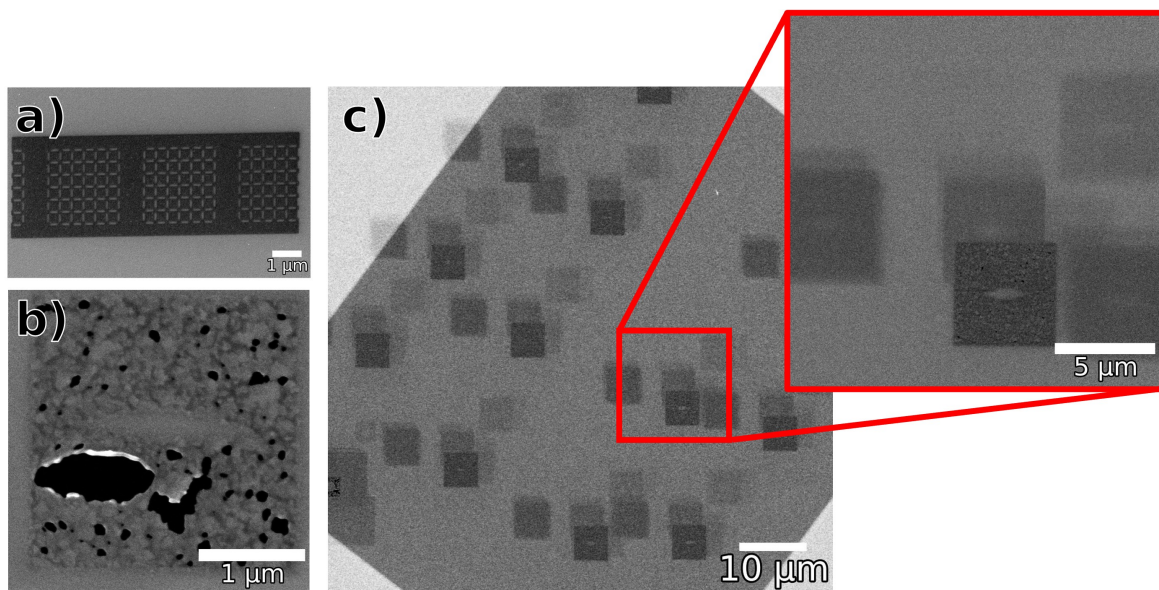


**Figure A.1: Challenges met during FIB milling** | (a) Faulty patterning due to bitmaps exceeding the processing capacity of the FIB software. (b) Surface roughness and hole formation when milling small areas. (c) Ion beam jumping around, milling multiple patterns simultaneously.

Another major challenge met was that multiple patterns were milled at once, as shown in Figure A.1c. It is difficult to pinpoint the exact cause of this, but one explanation could be the same as in (a), that the bitmaps were too pixelated and therefore too large for the FIB software to handle. However, the bitmap used here (a

sharp single magnet studied early on), had a resolution of  $1024 \times 1024$ , which has not been a problem to mill later on. At this time, even  $1666 \times 1666$  was successfully milled without any trouble. This strange effect was however observed in the early stages of this work, at a time where the FIB (and thus the experimentalist herself) experienced many in-explainable issues. Thankfully, when the ion source was changed mid-ways in this project and the software updated, this problem was eliminated.

A problem that was not eliminated when changing the ion source, was hole formation during milling (see Figure A.1b). The issue was particularly prominent when milling smaller areas (e.g.  $5\mu\text{m} \times 5\mu\text{m}$  vs.  $10\mu\text{m} \times 10\mu\text{m}$ ) and/or intrinsic patterns (XS and S). This can be attributed to various factors such as ion beam current, dwell time, beam overlap, and milling strategy that we will now discuss further.

## Appendix B

### Extra STEM-DPC Data

All bitmaps and continuous tilt STEM-DPC data for the pinwheel, square and kagome structures can be found at Zenodo via [zenodo.org/record/8015634](https://zenodo.org/record/8015634).

**Table B.1: ADF-STEM-DPC results of sqASI |** Bitmap mask, reconstructed BF image, vector map with and without mask as well as DPC<sub>x</sub> and DPC<sub>y</sub> for the S and XS sq structures. Scale bars are 2  $\mu\text{m}$ .

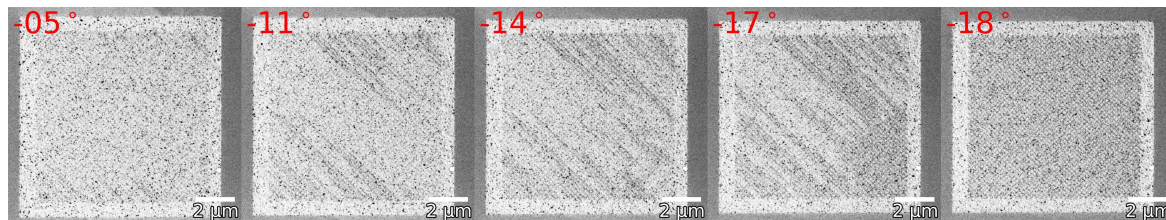
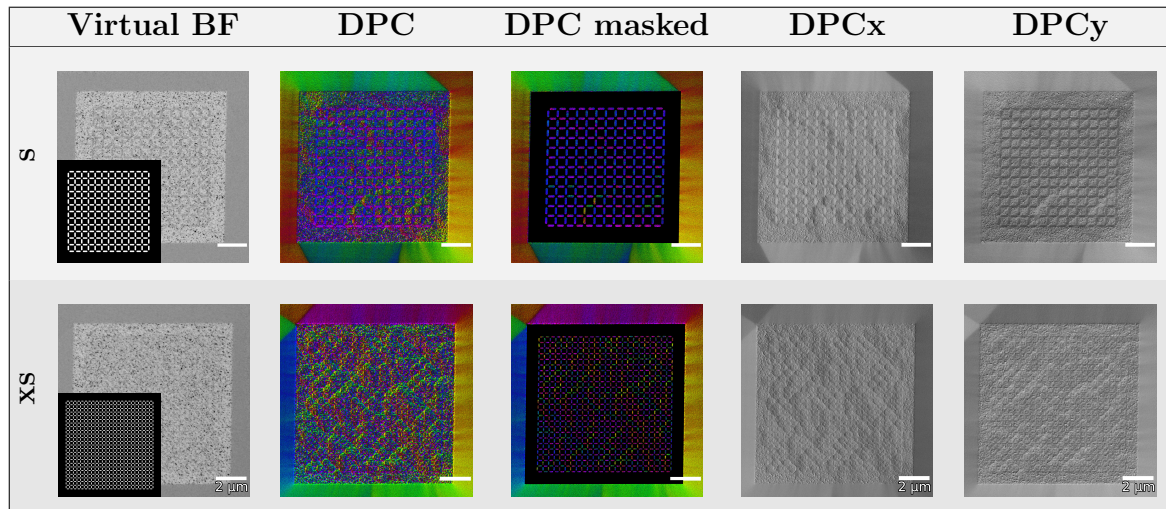


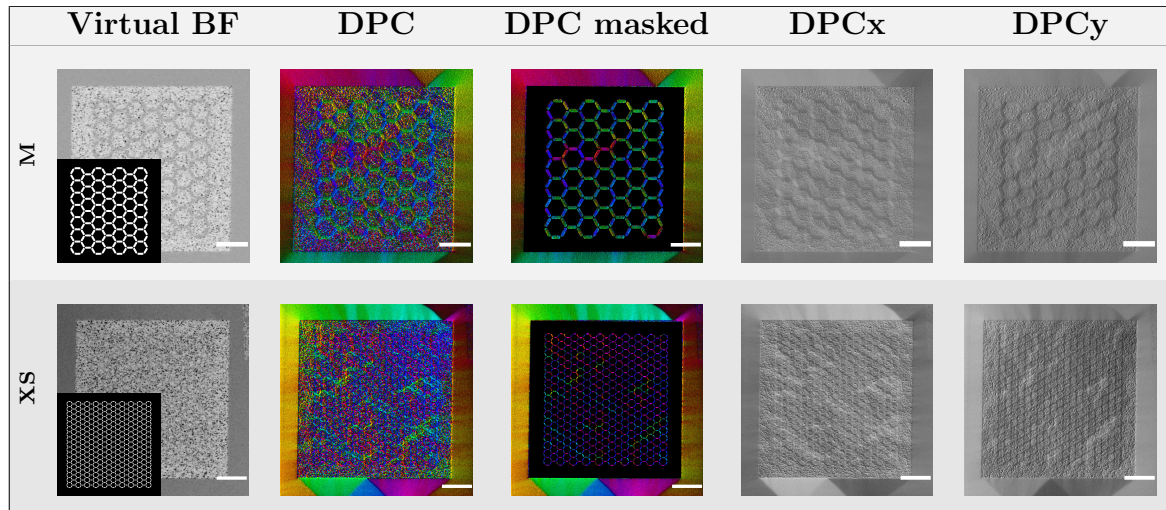
**Figure B.1: Continuous tilt STEM-DPC series of an XS-sized pinwheel.**

## Appendix C

### The Kagome Lattice

The Kagome lattices with islands sized M, S and XS were not discussed in this work as the results do not provide any new information regarding the characterization methods beyond what the pw, or sq did. However, the results for M and XS are shown in Table C.1.

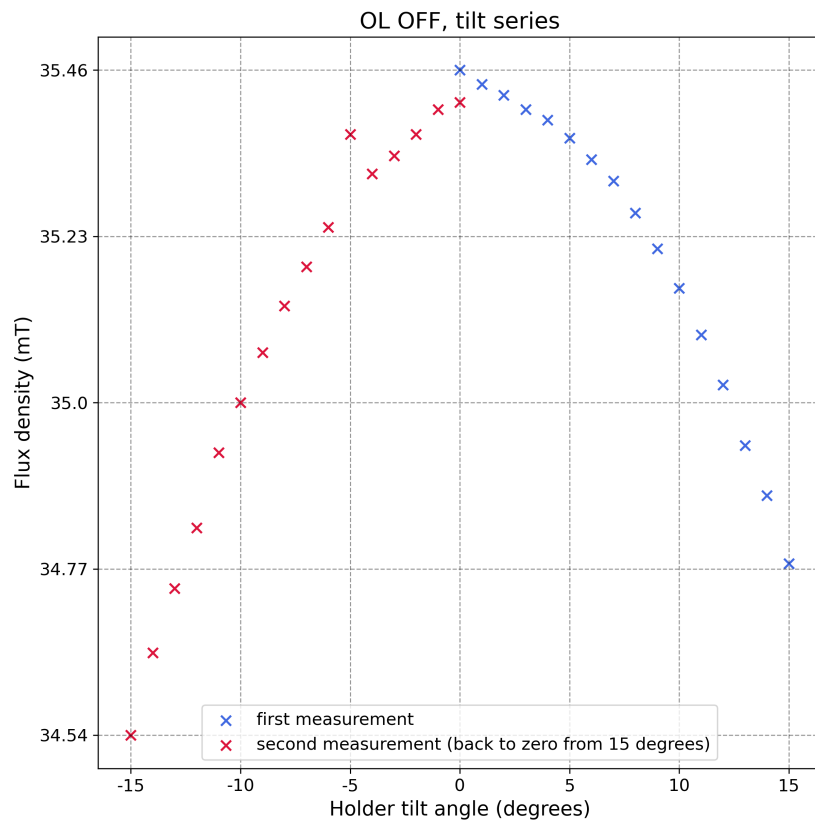
**Table C.1: ADF-STEM-DPC results of kagome ASI |** Bitmap mask, reconstructed BF image, vector map with and without mask as well as DPCx and DPCy for the M and XS kagome structures. Scale bars are 2  $\mu\text{m}$ .



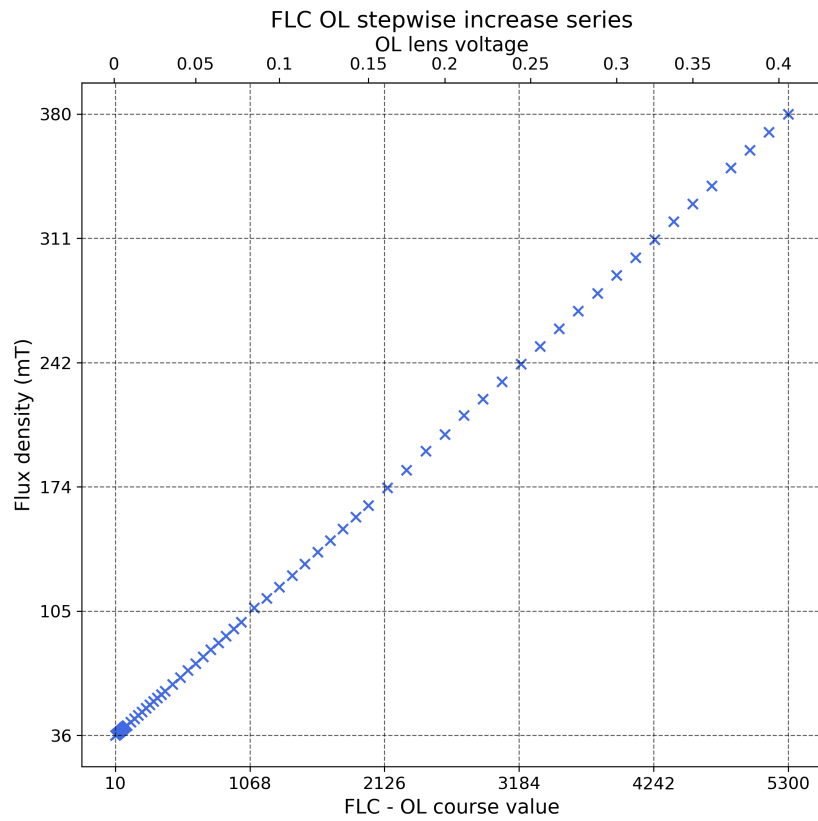


## Appendix D

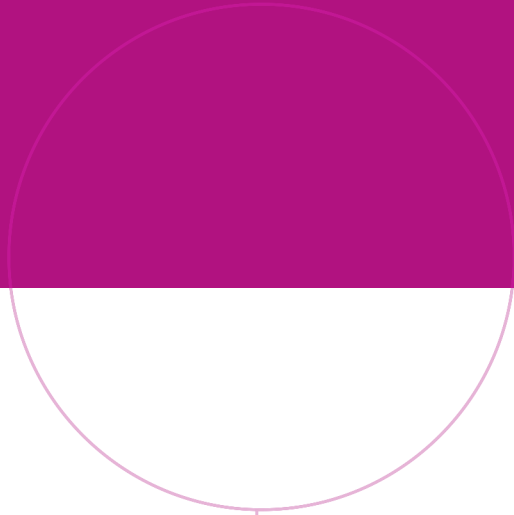
# Magnetic Field Measurements of the OL



**Figure D.1: Measured flux density when OL is off as a function of specimen tilt** | Flux density shows a parabolic dependency on sample tilt, but with the small variations seen, this effect can be neglected. Based on this experiment, the residual field is therefore assumed to be around 35mT.



**Figure D.2:** Measured flux density as a function of OL strength | Flux density increases linearly with the current applied to the OL.



Norwegian University of  
Science and Technology